TECHNISCHE UNIVERSITÄT MÜNCHEN

Lehrstuhl II für Technische Chemie

Bifunctional Pt/MFI Catalysts for Hydrogenation of Phenol in Aqueous Phase

Guoju Yang

Vollständiger Abdruck der von der Fakultät für Chemie der Technischen Universität München zur Erlangung des akademischen Grades eines

Doktors der Naturwissenschaften (Dr. rer. nat.)

genehmigten Dissertation.

Vorsitzender: Prof. Dr.- Ing. Kai-Olaf Hinrichsen

Prüfer der Dissertation:

1. Prof. Dr. Johannes A. Lercher
2. Prof. Dr. Klaus Köhler

Die Dissertation wurde am 10.05.2017 bei der Technischen Universität München eingereicht und durch die Fakultät für Chemie am 01.06.2017 angenommen.

Statutory Declaration

I declare that I have authored this thesis independently and that I have only used the declared (re)sources and I have explicitly marked all the materials which have been cited either literally or by content from the used sources. At the end of each chapter all collaborators are named and their specific contributions are explained. Publication issue of each chapter is marked at the end of each chapter.

May 2017, Munich   _____

To open a new chapter of my future.

"Think highly of yourself because the world takes you at your own estimate."

Kurt Hahn (1886 – 1974)

Acknowledgements

How time flies. Many ups and downs in the past 4 years, but all are sweet memories to cheer at the end. I want to use this opportunity to express my deepest gratitude to everyone who has provided me support, one way or another, throughout the study in the Chair of Technical Chemistry II at Technische Unviersität München.

First and foremost, I would like to thank Prof. Dr. Johannes A. Lercher for, not only in providing the necessary facilities to conduct my research but also providing me the opportunity to conduct and execute such a challenging and interesting topic under his guidance in the Chair of Technical Chemistry II. He has opened my eyes to a future of many different possibilities in the field of catalysis and its broad capabilities. In addition, it has been my great pleasure to experience his humorous conversation and intelligent discussion, from which I learned how to put the motivated and positive attitude to the work and life in the future.

Secondly, I am very grateful to my supervisor, Dr. Yue Liu, for his unrelenting guidance throughout the execution of my thesis. Without his dedicated support in every step throughout the process, this paper would have never seen the light of day. Other than imparting his knowledge and guidance, he is also a good friend, more likely a brother for me. I will never forget the fantastic time experienced with you and your family during my stay here.

Furthermore, I would like to give the gratitude to the members of biomass group, Dr. Eszter Baráth, Dr. Yuanshuai Liu, Dr. Jiayue He, Dr. Wenji Song, Dr. Marco Peroni, Manuel Wagenhofer, Peter Hintermeier, Sebastian Eckstein, Martina Braun, Moritz Schreiber, Xi Chen for all the insightful discussions; as well as other senior scientist of TCII: Dr. Prof. AndreasJentys, Dr. Erika Ember, Dr. Maricruz Sanchez-Sanchez, Dr. Ricardo Bermejo-Deval. Besides the TCII members, I am also grateful for the kind help and fruitful

discussions with Dr. Donald M. Camaioni and Dr. Hui Shi at Pacific Northwest National Laboratory.

I would also like to express my thanks to other former or present colleagues, namely Dr. Yu Lou, Dr. Wenhao Luo, Ruixue Zhao, Takaaki Ikuno, Wanqiu Luo, Yang Zhang and Guanhua Cheng. Without them, laboratory work every day would have been mundane and boring. Thanks for giving me so many happy times in Munich.

My thanksgiving goes to the students who ever worked with me, Johann, Dan, Thomas, Bau and some other members whose names are not mentioned here, Thank you all for your tolerance, accompanies and friendship in my doctoral topic.

The kind help and assistance from technical and administrative staffs of TCII are also highly appreciated. I want to thank Xaver Hecht for N_2 physisorption and hydrogen chemisorption measurements. Thank Martin Neukamm, who helped me perform AAS and SEM measurements and Andreas Marx, who helped me solve all the electronic problems. I am also grateful for the great assistance with all the administrative matters of all nice secretaries, Ulrike Sanwald, Bettina Federmann and Karen Schulz.

Finally, I would like to express my utmost thankfulness to my family, friends back home in China for not only providing me the financial backbone to complete my university studies in TUM but also in supporting me to get where I am today. Studying in a foreign environment, more than 10,000 km away, for more than 3 years has not been easy but I achieved it.

Many thanks to all of you, Guoju

April 2017

Symbols and Abbreviations

AAS	Atomic absorption spectroscopy
AHFS	Ammonium hexafluorosilicate
BAS	Brønsted acid site
BET	Brunauer-Emmett-Teller
CO	Carbon monoxide
C_{phenol}	Phenol concentration
DFT	Density functional theory
DP	Deposition-precipitation
EXAFS	Extended X-ray absorption fine structure
GC	Gas chromatography
h	Hour
HC	Hydrocarbon
HDO	Hydrodeoxygenation
IR	Infrared
I	Moment of inertia
K	Kelvin
K_a	Adsorption equilibrium constant
k_a	Adsorption rate constant
k_{-a}	Desorption rate constant
KIE	Kinetic isotope effect
LAS	Lewis acid site
(m)L	(Milli) liter
min	Minute
MS	Mass spectrometer
nm	Nanometer
NMR	Nuclear magnetic resonance
NP(s)	Nanoparticle(s)
p_{H2}	H_2 partial pressure

RDS	Rater determining step
STEM	Scanning Transmission electron microscopy
TEM	Transmission electron microscopy
TOF	Turnover frequency
wt.%	Weight percent
XRD	X-ray diffraction
XAS	X-ray absorption spectroscopy
XANES	X-ray absorption near edge structure
Z-OH	H-form Brønsted acid site of zeolite
Z-OD	D-form Brønsted acid site of zeolite
ZPE	Zero point energy
θ	Coverage
$\Delta H^{\ddagger}$	Enthalpy of activation
$\Delta S^{\ddagger}$	Entropy of activation

Abstract

Pt clusters encapsulated in MFI micropores with varying Brønsted acid site (BAS) concentrations were prepared and characterized. The kinetics and thermodynamics of H_2 adsorption on these Pt/MFI catalysts in the aqueous phase were determined by a novel kinetic method. The Pt/HMFI catalyst using acidic support (Si/Al = 24) showed lower adsorption heat of H_2 than that using neutral support (Silicalite-1). The hydrogenation activity of these catalysts in the aqueous phase was tested by the reaction of phenol hydrogenation. The hydrogenation rate of phenol showed a positive correlation with the hydronium ion concentrations in MFI micropores. Furthermore, catalysts with higher hydronium ion concentrations showed weaker adsorption of phenol. The hydronium ions in adjacent to Pt clusters in MFI micropores changed the H-addition pathways. In the presence of hydronium ion, protonation of the aromatic ring coupled with electron transfer led to a higher rate than the conventional addition of hydrogen atom. This changed the reaction order of H_2 from 0.5 to 1 and decreased the corresponding activation energy from 94 to 63 $kJ \cdot mol^{-1}$. The promising results in this dissertation could shed light on understanding the H_2 activation process on transition metal catalysts in the aqueous phase. Meanwhile, it could provide a potential way to design promising bifunctional catalysts for the biomass conversion.

Kurzzusammenfassung

Es wurden verschiedene, in MFI-Mikroporen geträgerte Pt Cluster mit unterschiedlichen Konzentrationen an Brønsted-Säurezentren synthetisiert und charakterisiert. Die Kinetik und Thermodynamik der H_2-Adsorption an diesen Pt/MFI-Katalysatoren in Wasser wurde mittels einer neuartigen Methode ermittelt. Die aus sauren Trägermaterial (Si/Al = 24) bestehenden Pt/MFI- Katalysatoren zeigten eine niedrigere Adsorptionswärme von H_2 als die aus neutralem Trägermaterial (Silicalite-1) bestehenden Katalysatoren. Die Aktivität der Hydrierung dieser Katalysatoren wurde in der Phenol-Hydrierungsreaktion in wässriger Phase ermittelt. Mit der Erhöhung der Hydroniumionen geht eine positive Korrelation mit der Hydrierungsrate einher. Katalysatoren mit einer höheren Konzentration von Hydroniumionen zeigten eine schwächere Adsorption von Phenol. Die Hydroniumionen in Nachbarschaft zu den Pt-Clustern in MFI-Mikroporen veränderten den Mechanismus der Wasserstoffaddition. In der Anwesenheit von Hydroniumionen führt die Protonierung des aromatischen Ringes, gepaart mit Elektronentransfer, zu einer Erhöhung der Rate im Vergeich zu der konventionellen Addition des Wasserstoffatomes. Dies änderte die Reaktionsordung des Wasserstoffes von 0,5 auf 1 und senkte die dazugehörige Aktivierungsenergie von 94 auf 63 $kJ \cdot mol^{-1}$. Diese vielversprechenden Ergebnisse in dieser Dissertation könnte Licht in das Verständnis des Prozesses der H_2-Aktivierung in wässriger Phase auf Übergangsmetallkatalysatoren bringen. Währenddessen könnten sie einen potentiellen Weg zur Entwicklung vielversprechender bifunktionaler Katalysatoren zur Umwandlung von Biomasse aufzeigen.

Table of contents

Chapter 3

3. Determination of H_2 adsorption heat on Pt/MFI catalysts in the aqueous phase.. 61

Chapter 4

Chapter 1

Introduction

1.1. General background

With the increase in the price of fossil fuels in recent years and its foreseeable shortage in the future, finding an alternative route for the production of fuels has become urgent and necessary. The U.S. Energy Information Administration (EIA) released the International Energy Outlook 2016 in which an assessment for international energy markets through 2040 was presented, as shown in **Figure 1.1**. It predicted that the world energy consumption by fuel would increase by 56% till 2040, from 524 quadrillions British thermal units (Btu) to 820 quadrillions Btu. Moreover, liquid fuels, coal and natural gas will still be the dominant energy source and will take up at least 80 % of the world's total energy production in the early future. The utilization of renewable energy sources, as the green line shown in **Figure 1.1**, will become a trend to produce the replacement of fossil fuel, and will dramatically increase in the following decades. Therefore, advanced technologies and methods for utilizing renewable energy sources have attracted increasing interests.
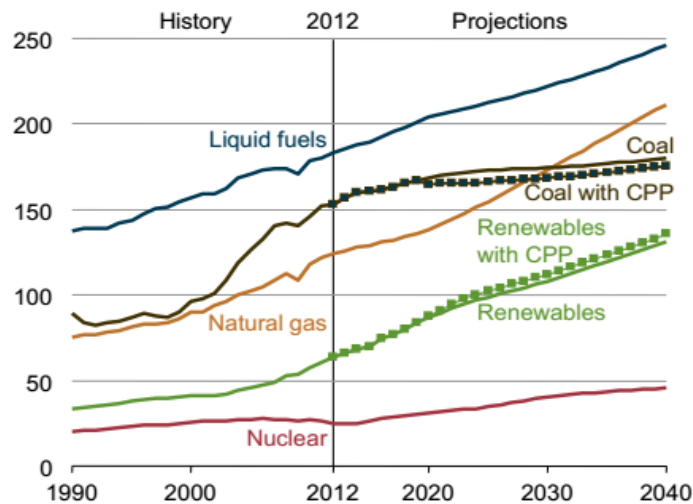
Figure 1.1. Total world energy consumption by different energy sources in the past and in the projections from 1990 to 2040 (quadrillion Btu).[1]

The development of renewable energy resource will not simply enhance the worldwide economic but reduces environmental pollution issues as well. In the US, the renewable

energy took up approximately 10 % of the total consumed energy in 2015. Among all kinds of renewable resources, the biomass source supplied approximately 50 % of all consumed renewable energy (**Figure 1.2a**).
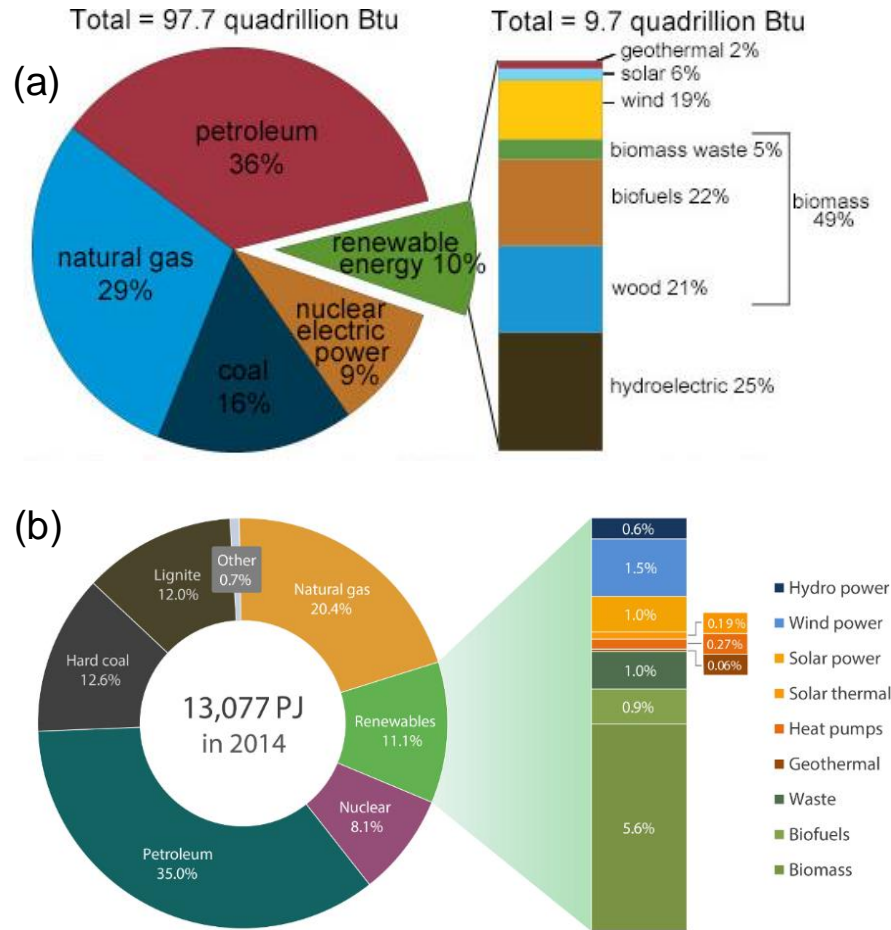
Figure 1.2. The energy consumption mix and renewable energy construction in the United States in 2015 (a) and in Germany in 2014 (b).[2, 3]

The similar situation was observed for that in Germany, which is shown in **Figure 1.2b**. The renewable energy made up 11 % of German primary energy consumption, but more than half of it was from biomass. Therefore, it can be concluded that the biomass has been becoming one of most promising renewable energy sources recently. It is interesting to note that final energy consumption from biomass raised about 16 million tons of oil equivalent in the past decades between 2000 and 2011, while the supposedly rapid expansion of the wind and solar energy just grew by 3.4 and 2.1 million tons, respectively.

In another word, absolute growing utilization of biomass in Germany has become 3-fold higher than that of summed wind and solar, as shown in **Figure 1.3**.
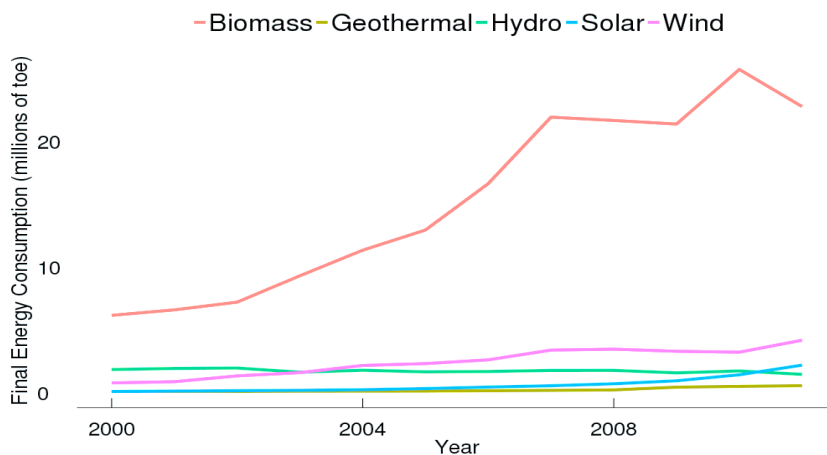
Figure 1.3. Consumption of renewable energy in Germany from 2000 to 2011 (energy unit is million tons of oil equivalent).[4]

All the statistics about renewable energy consumption point out that biomass has been regarded as a potential feedstock for the sustainable production of fuel energy in the future, because of its abundance, availability, and renewability.

For example, biofuels including biogas, bioalcohols, bioethers, biogasoline and biodiesel *etc.*, has become the primary alternatives to fossil fuel and been applied in the industry. However, disadvantages of these biofuels, such as low oxidation stability and corrosive nature, limit their direct application as transportation fuels as well.[5] Given this, abundant efforts have been made by scientists to develop new technologies and process for producing more stable and effective biofuels in the past decades. For instance, the utilization of heterogeneous catalysis has been universally assessed as the most promising process to produce and improve the biofuels sustainability recently. In this thesis, bifunctional catalysts composed of Pt cluster in acid zeolites are employed to investigate hydrogenation reaction of phenol which is a simplest phenolic monomer from bio-derived compounds.

1.2. Lignocellulose-derived feedstocks

1.2.1. The components and structures of lignocellulose

Lignocellulosic biomass represents a series of lignocellulosic materials available largely in the form of agricultural and forestry residues, such as corn stover, sugarcane bagasse, rice straw or switchgrass, miscanthus, poplar, willow, *etc.*.[6] The lignocellulosic biomass has great potential for bio-fuel production, because it is rich in carbon by fixing atmospheric carbon via photosynthesis to generate carbon-based metabolites. Typically, lignocellulosic biomass consists of cellulose (35 – 50 wt. %), hemicellulose (25 – 30 wt. %) and lignin (15 – 30 wt. %),[7] and roles of them in the plant are depicted by Menon and his co-workers,[7] as shown in **Figure 1.4**. Specifically, cellulose and hemicellulose are main structural components of plant cell walls. Cellulose is crystalline, strong, and resistant to hydrolysis hence contributing to mechanical strength, while hemicellulose, as heteropolymers composed of pentoses and hexoses, has a random and amorphous structure with little strength. Lignin is cross-linked phenolic polymers mainly containing coniferyl alcohol, sinapyl alcohol and para-coumaryl alcohol, which fills the spaces in the cell wall between cellulose and hemicellulose and is responsible for the structure rigidity of plants. Among the three major biopolymer compounds, lignin is able to contribute up to 40 % of the total energy content of the plant biomass, thus causing more interest to be chosen as model compounds to study biomass conversion.
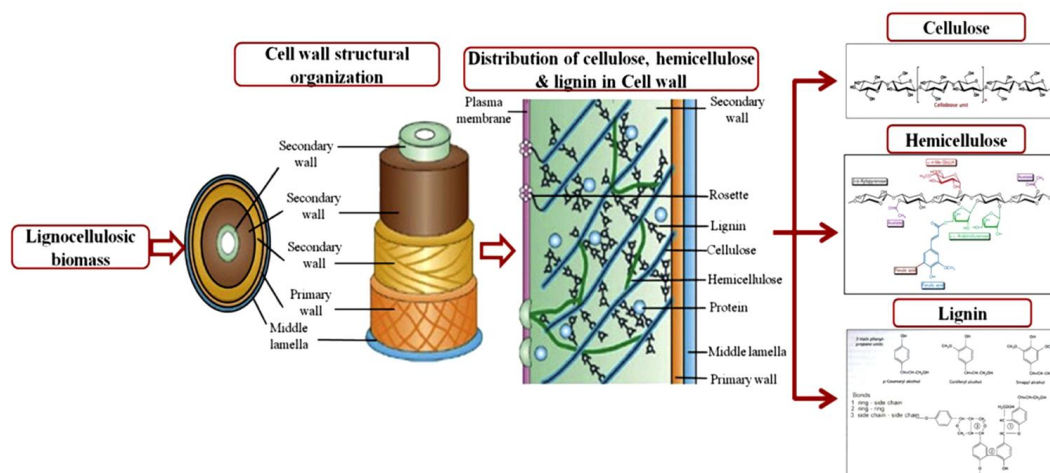
Figure 1.4. Diagrammatic illustration of the framework of cellulose; hemicellulose and lignin in the plant cell organization.[8]

1.2.2. Conventional technologies for lignocellulose conversion

Lignocellulosic biomass contains a relatively lower energy density compared to fossil fuels, because of its high oxygen and water content and low carbon density. Therefore, it is necessary to carry out depolymerisation and size-reduced process for upgrading lignocellulosic materials and produce smaller molecules. To date, there are two major approaches to be considered in order to reduce macromolecule size, as shown in **Figure 1.5**. One approach is biochemical conversion. For instance, the utilization of some enzymes is able to decompose sugar polymers into their constituent monomers, which can be further transformed into a variety of alcohol, methane or other special chemicals.[9]

The second approach involves thermal-chemical processing that mainly includes (i) gasification; (ii) liquefaction; (iii) pyrolysis. Specifically, gasification can convert lignocellulosic materials into syngas which could be further converted to hydrocarbons via Fischer-Tropsch synthesis route. Alcohols could be achieved by treating the syngas using anaerobic bacteria.[10, 11] Furthermore, thermo-chemical process, like pyrolysis or liquefaction, can convert the lignocellulosic biomass into size-reduced bio-oil which includes various liquid organics mixtures with different oxygen-containing functional groups. In fast pyrolysis, the biomass-derived feedstock is rapidly heated in a fluidized bed reactor in the absence of oxygen to very high temperature (573 – 873 K) under atmospheric

pressure at short residence times (1 – 2 s).[12] In terms of liquefaction, both high temperatures (573 – 673 K) and hydrogen pressures up to 20 MPa are needed to produce bio-oil.[13]

There are more than 300 different compounds identified in bio-oil, where the specific composition of the product depends on the feed and process conditions used in the bio-oil conversion. In general, bio-oil mainly comprises of water-soluble acetic acid, sugars, polyols and n-hexane-extracted organic molecules including phenols, ketones, aldehydes, and furans. The acetic acid, sugars, and polyols can be used to produce hydrogen through aqueous phase reforming. Meanwhile, the hydrogen produced via these components is enough to selectively hydrogenate the remaining organic fraction to a hydrocarbon transportation fuel.[14]
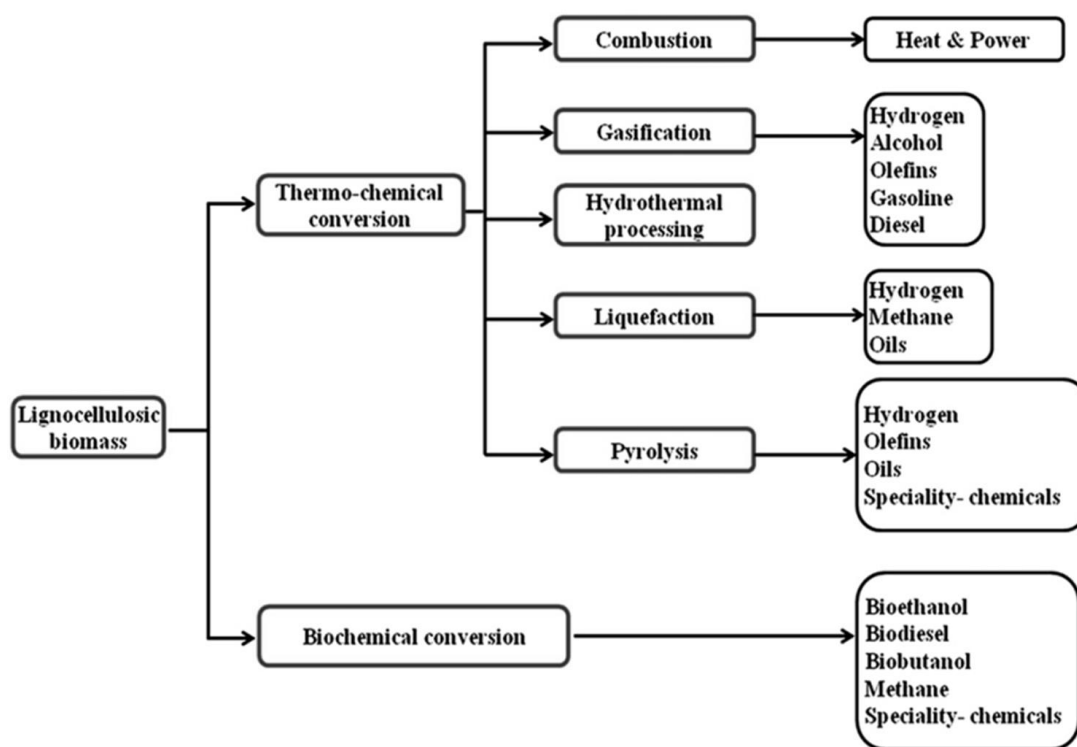
Figure 1.5. Thermo-mechanical and biochemical processing of lignocellulosic biomass into various fuel or fine chemical products.[8]

Despite the advantages of bio-oil mentioned above, its thermal instability, high viscosity, non-volatility and corrosiveness resulted from the high content of oxygen limit its direct

application as the source of energy. For example, bio-oil cannot be burned directly in diesel engines as its low heating value causes ignition difficulties. In addition, its thermally unstable components lead to an excessive coking to the engine. Therefore, in order to overcome these drawbacks of bio-oil, oxygen in the organic compounds has to be removed to upgrade the bio-oil.

1.2.3. Bio-oil upgrading

Given the unfavorable characteristics of bio-oil mentioned above, the upgrading process is considered as a feasible route to transfer the crude bio-oil into biofuel which can be used as a transportation fuel or fine chemicals, as depicted in **Figure.1.6.** Currently, there are two general routes having been taken into account for bio-oil upgrading, i.e. hydrodeoxygenation (HDO) and zeolite cracking. Typically, HDO is a high-pressure operation where hydrogen is used to remove oxygen from the bio-oil, producing high-grade oil products. While zeolite cracking provides another upgrading path, where acid zeolites are used as deoxygenation catalysts.
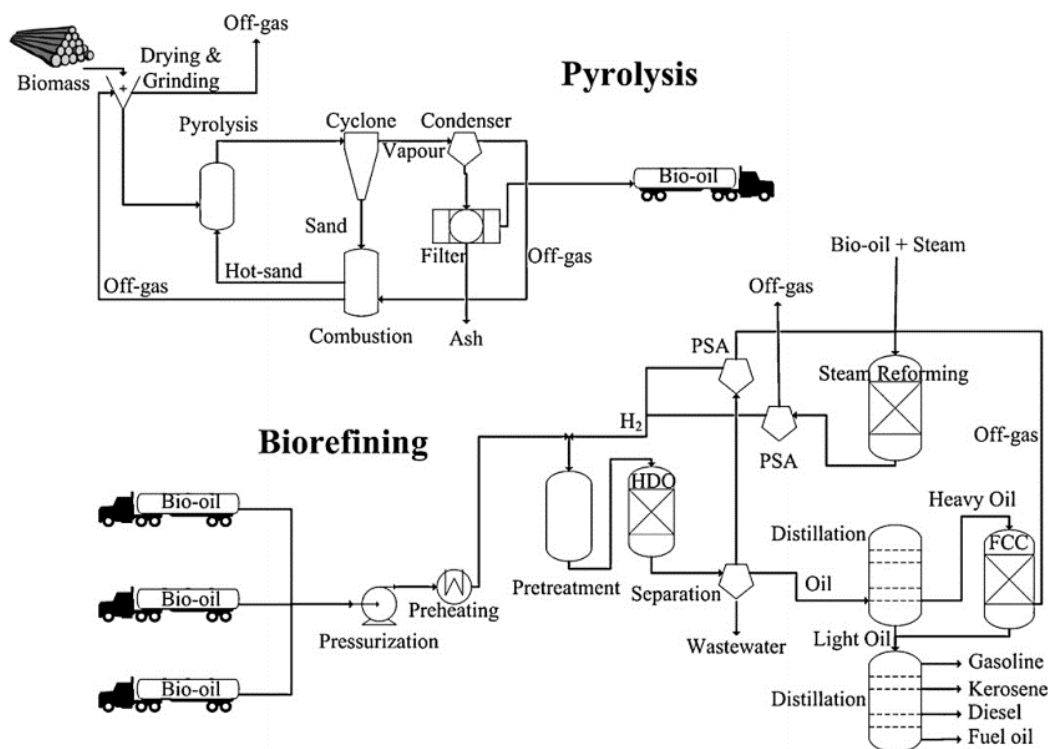
Figure 1.6. Overall flow sheet for the production of bio-fuels on the basis of catalytic upgrading of bio-oil.[14]

However, in the realistic catalysis system, catalytic upgrading of bio-oil is a complex reaction network, because of a high diversity of compounds in bio-oil. As summarized in **Scheme 1.1**, cracking, decarbonylation, decarboxylation, hydrocracking, hydrogenation hydrodeoxygenation and polymerization have been reported to take place for both cracking and HDO.

In catalytic cracking, hydrogen is not a requirement anymore. This catalytic process is able to be carried out at atmospheric pressure. However, extensive carbon deposition on the zeolite leads to a very short catalyst lifetime, which limits its broad application presently. Therefore, substantial research has been carrying out in the field of HDO, which not just constitute a possible route for the production of synthetic fuels but is also able to achieve a good economy potential. Furthermore, this route also constitutes a path to fuels applicable in the current infrastructure.

.
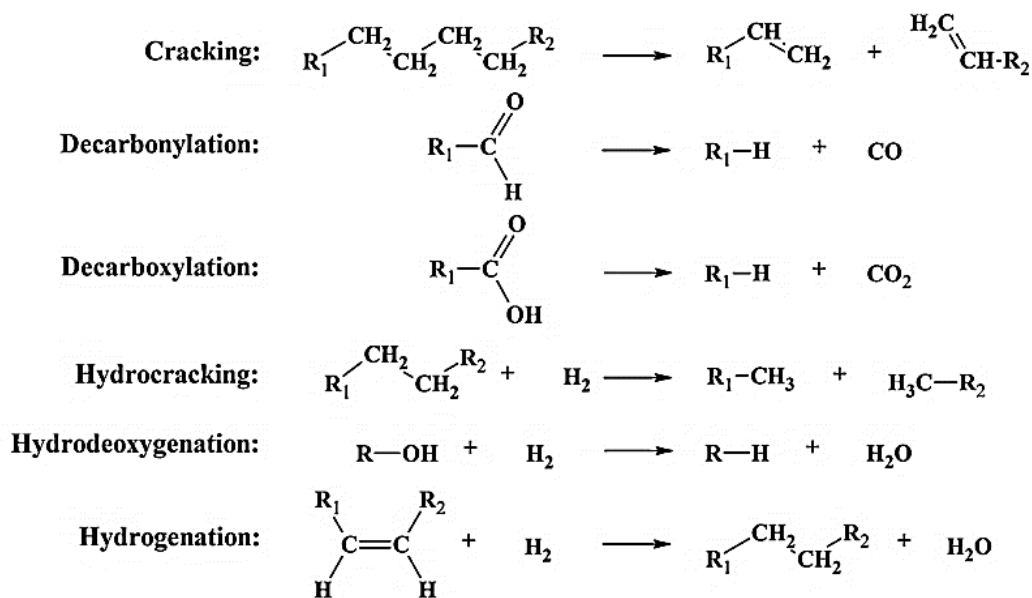
Scheme 1.1. Reaction network associated with catalytic bio-oil upgrading.[14]

1.3. HDO of bio-derived compounds over bifunctional catalysts

1.3.1. General introduction of hydrodeoxygenation reactions

HDO generally involves a high H_2 pressure reaction over the heterogeneous catalyst. The presence of high H_2 pressure not simply ensures a higher solubility of hydrogen in the reaction system for enhancing the availability of hydrogen in the vicinity of the catalyst but can inhibit carbon deposition on the catalyst surface thus improving the efficiency of reactor operation as well. Meanwhile, oxygen content will be removed from the bio oil-derived compounds in the presence of the hydrogen.
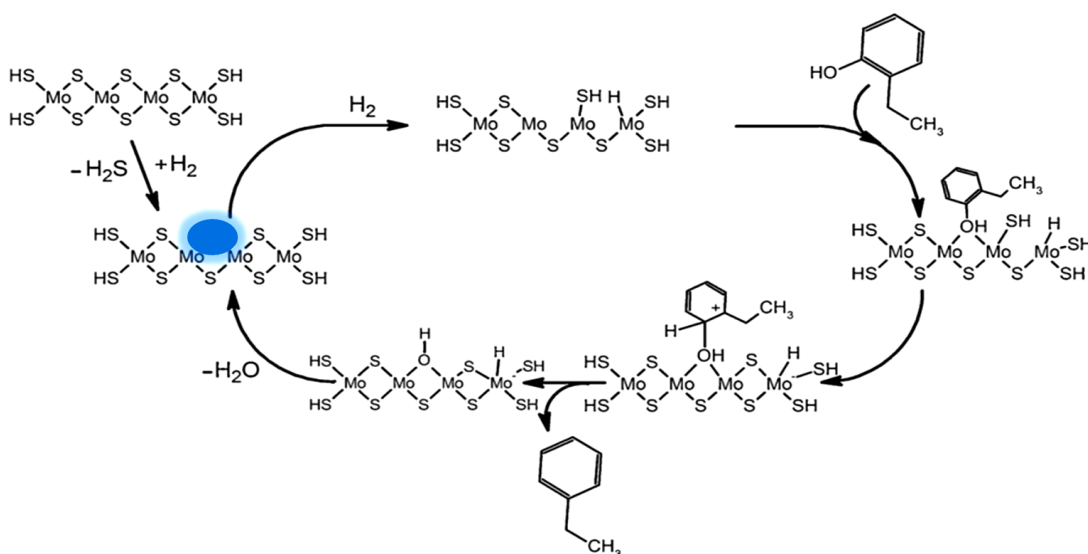
Scheme 1.2. Proposed mechanism for HDO conversion of 2-ethylphenol on a Co–MoS$_2$ catalyst. The blue circle refers to the catalytically active vacancy site.[14, 15]

A variety of different catalysts has been utilized for the HDO process, in which sulfide/oxide type catalysts or supported transition metal catalysts are most widely used. As for sulfide/oxide catalysts, Co/MoS$_2$ and Ni/MoS$_2$ are the most conventional catalysts which have been extensively and frequently applied in the HDO reaction. They are abundantly used as industrial hydrotreating catalysts for removing sulfur, nitrogen, and oxygen from petrochemical feedstocks. In sulfide CoMo and NiMo-based catalysts, Co or Ni serves as promoters, which can donate electrons to the molybdenum atoms. Therefore, the bond between molybdenum and sulfuric weakened, forming a sulfur vacancy site which is an active site in both HDO and HDS reactions.[12] In **Scheme 1.2**, a schematic

representation of HDO reaction of 2-ethylphenol to ethylbenzene over a Co-MoS$_2$ catalyst is drawn, where blue cycle refers to the active sulfur vacancy site on the catalyst.

In terms of supported transition metal catalysts, mechanistic speculations of HDO reaction suggest that the supported transition metal catalyst should exhibit two functions, one is hydrogenation capacity, the other is deoxygenation ability, both of which ensure the cascade reaction of hydrogenation and deoxygenation/dehydration occurring.

Figure 1.7. Phenol hydrodeoxygenation and hydroalkylation over Pd/C combined with zeolite H-BEA and La-BEA catalysts.[16]

As for hydrogenation, most of the transition metals, such as Pd, Pt, Rh, Ni, *etc.*, exhibit excellent catalytic hydrogenation activity, i.e. reducing or saturating organic compounds by adding hydrogen. The dehydration in HDO is the other process whereby oxygen is removed as water, generally followed by adding hydrogen (hydrogenation) for retaining the carbon molecular architecture. In the dehydration reaction, the acid catalyst system is widely applied, including homogeneous and heterogeneous acid. In comparison with liquid homogeneous acid, such as HClO$_4$ and H$_2$SO$_4$ and H$_3$PO$_4$, *etc.*, the heterogeneous acid catalysts mostly like acid oxides, modified carbon/SiO$_2$ and zeolite show more advantages and potential for industrial application because they are recyclable, harmless, profitable and environmentally friendly. For example, Zhao and her co-workers designed acid zeolite-supported Pd bifunctional catalyst which consisted of Pd/C combining with zeolite H-BEA and La-BEA. The catalyst was tested in aqueous phase phenol hydrodeoxygenation and hydroalkylation in the presence of H$_2$, the process of which is depicted in **Figure 1.7**. They
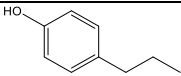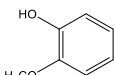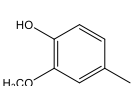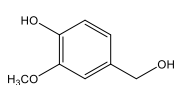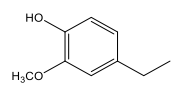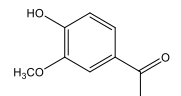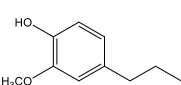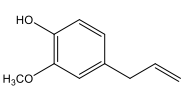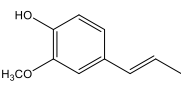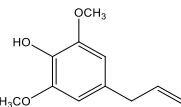
found an optimized H^+/Pd ratio (ratio = 21) to enhance the selectivity of final hydrocarbon products by adjusting the ratio of Pd/C to BEA based zeolites. In this reaction, Pd is in charge of hydrogenation, and dehydration is solely catalyzed by Brønsted acid sites from BEA zeolite, while alkylation can be achieved in the presence of La^{3+} cations.

1.3.2. Applications of bifunctional metal/acid catalysts for HDO reactions

In most cases, multistep conversions are involved to upgrade highly functionalized biomass molecules. Heterogeneous catalysts are more desirable as they are easy to be separated and purified from the reaction mixture after the reaction, in comparison with the homogeneous catalyst. Therefore, it is necessary to design multifunctional catalysts by integrating functions of various active sites. A majority of studies have been reported, which involve the development and optimization of multifunctional catalysts for the biomass conversion into chemicals and biofuels.[17, 18] Preparation of metal clusters on solid acids enables both of hydrogenation and dehydration abilities via combining metal and the functions of Brønsted or Lewis acid sites.

Lercher's group developed a series of metal/acid bifunctional catalysts for HDO conversion of lignin-derived compounds to biofuels in a one-pot process. The oxygen content of the chosen compounds was removed by acid catalyzed dehydration and hydrolysis. Meanwhile, metal clusters catalyzed hydrogenation, hydrogenolysis and decarbonylation of unsaturated compounds. They used bifunctional catalysts consisted of a metal (Pd or Ni) and acid (H_3PO_4, Nafion/SiO_2 or HZSM-5) to convert phenolic oil into gasoline-range hydrocarbons (C_6–C_9) in the aqueous phase under mild conditions.[16, 19-25] For instance, a series lignin-derived compounds including alkyl-, ketone-, and hydroxy-substituted or alkyl-substituted phenols and guaiacols, were effectively converted into cycloalkanes (73 – 92 %) and aromatics (5.0 – 15 %) over acid ZSM-5 zeolite supported Ni catalysts at 250 and 5 MPa of H_2 **(Table 1.1)**.[24] With the bifunctional Ni/HZSM-5 catalyst, supported Ni particles catalyze hydrogenation and dehydro-aromatization reactions, while Brønsted acid sites of the zeolite catalyze dehydration and hydrolysis steps.[20, 22, 23]

Table 1.1. HDO conversion of phenolic monomers over bifunctional Ni/HZSM-5 catalyst.[24]

Phenolic reactant	Conversion (%)	Selectivity (%)		
		cycloalkanes	aromatics	methanol
	100	92	8.0	-
	100	74	13	13
	100	73	15	12
	99	80	9.6	10
	99	79	10	11
	100	77	12	11
	98	84	6.0	10
	100	80	11	9.0
	100	79	12	9.0
	93	78	5.0	17

Reaction conditions: reactant (0.010 mol), 20 wt. % Ni/HZSM-5 (0.5 g), H_2O (80 mL), 523 K, 5 MPa H_2 (at ambient temperature), 2 h, stirred at 680 rpm.

1.3.3. Zeolite as a support of bifunctional catalysts

Zeolite is a kind of porous aluminosilicate materials which consist of aluminum and silicon surrounded by four oxygen, forming tetrahedral three-dimensional periodic framework. It is a suitable component to be used as an acid of the bifunctional catalyst, because of its acidity. The acidity of the zeolite is contributed by the aluminum coordination as well as the chemical nature of its neighbors. The concentration of acid sites will depend on the silicon to aluminum ratio which is then rated accordingly by it. There are two types of acid sites, i.e. Brønsted acid site (BAS) and Lewis acid site (LAS), existing in the zeolite. BAS

generally dominated most of the acid sites, as they are located at the bridging OH between the silicon and aluminum, as depicted in **Scheme 1.3a**. The negative charges caused by the aluminum substitution requires counter charged ions such as H^+ cations to balance the charges. Therefore, zeolites are able to behave as a Brønsted acid in donating protons to guest molecules and perform the acidic function. In particular, when the zeolite is used in the aqueous phase, Brønsted acidic protons transform into the hydronium ions, as shown in **Scheme 1.3b**.[26]

Apart from the acidity of zeolite, another advantage of zeolite as a support of bifunctional catalyst is its shape and size selectivity, which have attracted interest for both fundamental study and practical application.
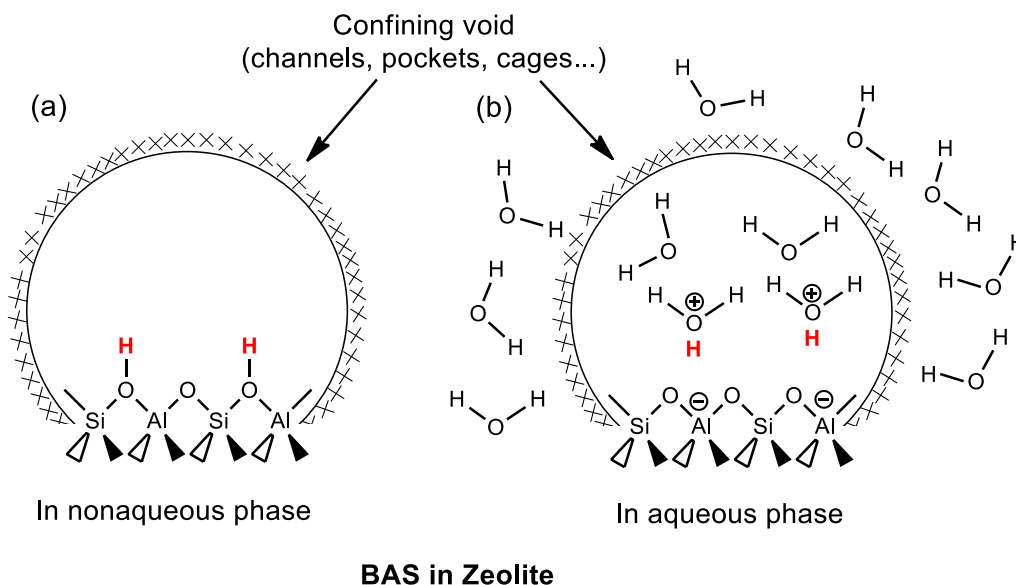
Scheme 1.3. Schematic representation of BAS structure in aluminosilicate zeolite, (a) in the absence of water; (b) in the presence of water.

Many applications require the use of porous materials catalyst. To achieve selectivity based on shapes and sizes of either reactants or products, the catalyst should possess uniform pores with molecular dimension. Zeolite has a unique framework, with highly ordered structure and uniform porosity made of the three-dimensional crystalline network that selectively retains molecules or transition state of certain sizes and excludes the large one. However, zeolite has only micropores which impose diffusional limitations on reactions

involving the participation of bigger molecules. If altering the porosity or particle size of zeolite, it will extend its application to offer unique structural and chemical features for meet abundant industrial demands. Therefore, several different strategies have been developed to solve this problem, as shown in **Figure 1.8**. One approach is to increase the pore size of the zeolite, such as developing mesoporous or macroporous zeolites with an unprecedented pore size,[27-29] or modifying the microporous zeolite by some technologies to offer different porous distribution but still possess acidity.[30, 31] Instead of increasing the pore size, the other approach is to decrease the crystal size of zeolite. Several synthesis strategies have been applied to prepare tiny zeolite crystals (< 50 nm).[32-34]
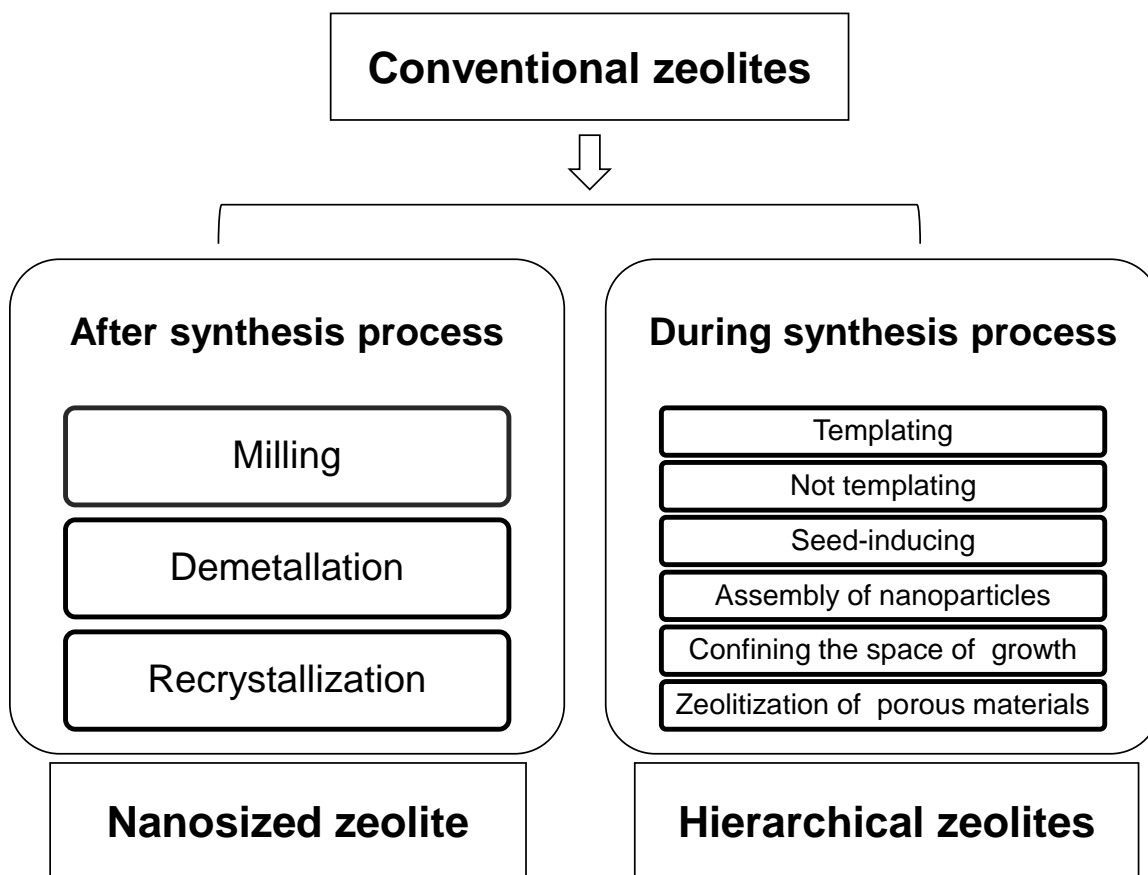
Figure 1.8. Overview of synthetic methods for nanosized zeolites and hierarchical zeolites.[33]

Besides shape selectivity and acidity, zeolites are also stable solids which can resist many environmental conditions compared to other materials. Such cases could be high temperature and high pressure. Because of its highly ordered structure made of the three-

dimensional crystalline network, the structure of most zeolites will not be affected when subjected to high temperature and high pressure. In terms of health concern, the zeolite is not harmful when in contact with skin or through inhalation as it is naturally occurring minerals, will also not cause harm to the environment.

Given the advantages of zeolite, it has become one of the most promising materials for bifunctional catalysts.

1.3.4. Preparation of metal/zeolite bifunctional catalyst

Zeolite supported metal catalyst is a typical and promising bifunctional catalyst as it combines two actives sites together, i.e. metal site and acid site. The support zeolite catalyzes dehydration and hydrolysis with its acid function combining with shape and size selectivity as well. While metal sites contribute to hydrogenation for unsaturated compounds. These two types of sites either catalyze in different steps of the whole reaction or occur in the same step. For example, it could be the interaction taking place at the different parts of the adsorbed reactant molecules in the presence of a metal/zeolite bifunctional catalyst.[35] Both of metal and acid zeolite ensure processing hydrogenation and dehydration of HDO reactions.

The components of metal/zeolite involve metal particles and zeolite support, sometimes with promoters. Metals, especially transitional metals are widely used as an ingredient of the bifunctional catalyst. Transition metals are significantly valued for HDO because of their partially occupied d-orbitals, the symmetry of which is suitable for formation of chemical bonds with neutral molecules. The stable oxidation states and different coordination numbers of transition metal result from the changes in the number of d-electrons.

The function of the support, as discussed above, is not only to stabilize or modify metal particles but also to offer active sites participating in the reaction. Sometimes the promoters are used to enhance the catalytic performance or the structural effects of the bifunctional catalyst system.[36]

The synthetic strategies for loading metal on zeolite support have been extensively studied in the past decades. There are 4 major methods widely used for the preparation of high active metal/zeolite catalysts, which will be introduced in the following.

Incipient wetness impregnation method

In the first case, the method is done in a way that the dry support usually in powdered form is added slowly to the amount of solution equal to its pore volume containing required amount of metal precursor of the active phase under stirring. This is to ensure that the dry support is fully wetted. Once the support is in contact with the solution, it will be drawn into the pores by capillary suction. No excess of the solution remains outside the pore space for proper wetting. At this instance, the dry support turned into a gel-like substance. The continuous heating result in the solution being absorbed and the metal precursor is attached to the dry support.

Impregnation usually followed by drying which is to remove any excess precursor solvent. The impregnated sample is placed in the calcination tube and heated in the oven with the flow of gas. The heating rate may affect the drying process. Therefore, it should be properly programmed and studied before the drying proceed. The gas may be synthetic gas, hydrogen or oxygen depending on desired requirements. Temperature is maintained slightly higher than the boiling point of the solvent. The removal of excess solvent from the pores results in the increase of precursor concentration causing interaction between the precursor and support.

Compared with some other tedious and high-cost method, wet impregnation method provides a more simple option to produce a high active metal/zeolite catalyst with good dispersions. Hence, it is widely used in the lab and in the industry.[37]

Ion exchange method

On the other hand, the mechanism of ion exchange involves in the substitution of ionic species by another ionic species in the electrostatic interaction between the surface support and metal precursor. The surface support containing the first ion is soaked with excess volume compared to its pore volume of solution containing another ion. This ion immediately penetrates the pore space of the support and exchange position with the ion

found in the surface support. Later the exchanged ion moves into the solution. This process is repeated until equilibrium is reached.[36, 38]

Deposition-precipitation (DP) method

The deposition-precipitation (DP) method was developed by Geusand his co-workers.[39], which has become a promising approach to prepare a metal catalyst with high dispersion and high loading. As for the preparation procedure, oxide/zeolite supports are firstly added in a solution containing metal precursor, which undergoes basification of the suspension by urea ($CO(NH_2)_2$). The hydrolysis of urea gradually and slowly generates hydroxide ions at rising temperature, hence preventing local super-saturation and the sole precipitation of metal hydroxide.

Grafting as-synthesized nanoparticles (NPs)

This synthetic strategy was developed by Metin *et al*. for preparing Monodisperse nickel nanoparticles.[40] Specifically, the synthetic procedure of Ni NPs involves firstly the preparation of soluble Ni NPs by reducing [Ni(acetylacetonate)$_2$] with borane tributylamine in the presence of oleylamine and oleic acid. Afterward, the as-synthesized NPs was grafted onto the zeolite under stirring at an ambient temperature in hexane.
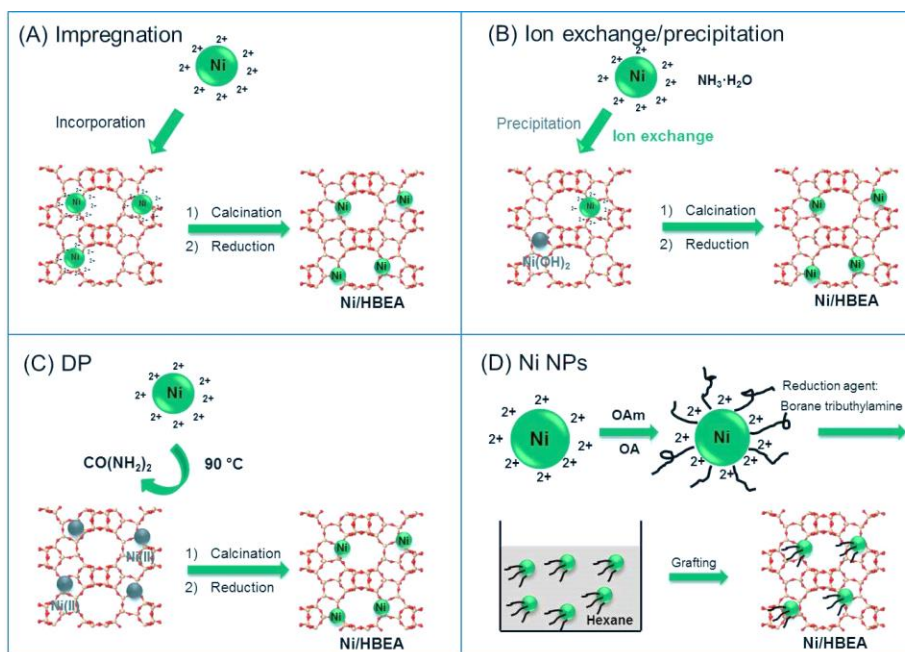
Scheme 1.4. Four processes for loading Ni nanoparticles onto/into Beta zeolite reported by Song *et al.* (a) impregnation; (b) ion exchange; (c) DP; (d) NP Grafting.[37]

Song *et.al.* prepared Ni nanoparticle on Beta zeolite via the four methods mentioned above They gave a schematic representation of the four methods in **Scheme 1.4**.

1.3.5. Application of metal/zeolite in the phenol HDO reaction.

Phenol as the simplest phenolic monomer of bio-derived compounds was always chosen as the model compound for HDO reactions in vast fundamental studies.[25, 41-45] Its HDO reaction was generally tested over a series of bifunctional catalysts. The reaction sequence for phenol HDO in the aqueous phase was studied by Zhao and his co-workers in the past years.[21, 22] In the beginning, they carried out the phenol hydrodeoxygenation reaction over Pd/C in the presence of H_3PO_4 acid, in which they found that reaction progress was accompanied by a growing cyclohexanol selectivity but a declining in cyclohexanone selectivity. This phenomenon indicated that phenol should firstly be hydrogenated to cyclohexanone which acts as an intermediate in the isomerization of the partial hydrogenation product cyclohexanol, as shown in **Figure 1.9a**. While phenol was not converted to benzene via a direct hydrogenolysis. Besides Pd/C, other supported noble metal catalysts such as Pt/C, Ru/C, and Rh/C can also efficiently catalyze the aqueous-phase hydrodeoxygenation of phenol to cyclohexane at 473 K in the presence of phosphoric acid, with a high yield (ca. 90%) and a high average turnover frequency (TOF >1200 h^{-1}).[22]
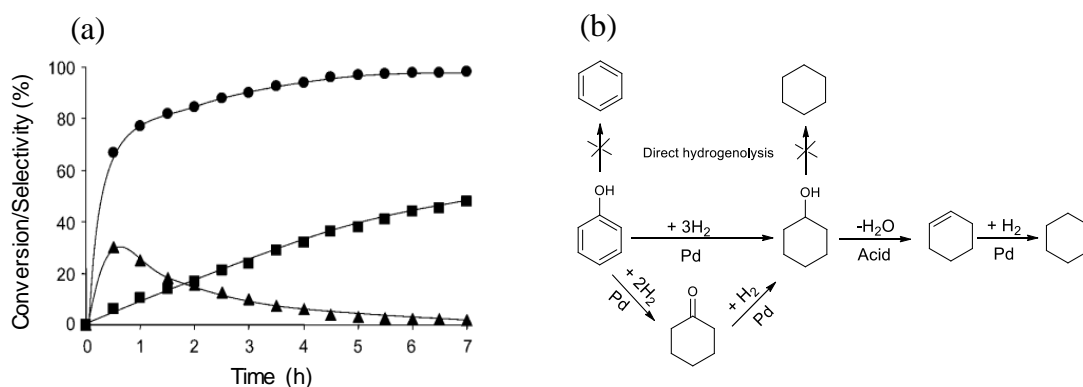
Figure 1.9. (a) Phenol conversion (■), cyclohexanol selectivity (●), and cyclohexanone selectivity (▲) as a function of reaction time in aqueous phase phenol hydrogenation. (b) Proposed reaction pathway of phenol hydrodeoxygenation over Pd/C in the presence of an H_3PO_4 acid.[22]

19

Zhao *et. al* studied the support effect on HDO activity by preparing Ni particles on HZSM-5 or on HZSM-5 coupling with 19.3 wt. % fraction of γ-Al_2O_3 binder and testing in phenol HDO reaction.[21] The detailed kinetics of fundamental steps that were involved in the HDO of phenol over the Ni/HZSM-5 and Ni/Al_2O_3–HZSM-5 catalysts was compared. Ni/Al_2O_3–HZSM-5 exhibited a higher HDO activity due to higher Ni dispersion. The Al_2O_3 binder stabilized the ketone intermediate by introducing Lewis acidity. Moreover, the cyclohexanol dehydration reaction rate on the Ni/HZSM-5 catalyst was slightly higher due to the higher Brønsted acid sites concentration. As a result, the dehydration was greatly enhanced by close proximity between acid and metal sites where the cyclohexene is irreversibly hydrogenated. The pathways of phenol hydrodeoxygenation over ZSM-5 supported Ni catalysts were also proposed which consisted of four individual steps, similar to **Figure 1.9b**. The initial step begins with phenol hydrogenation to cyclohexanone, followed by the second step, which is by cyclohexanone hydrogenation to cyclohexanol. Both steps were hydrogenated on metal sites. The next step is the cyclohexanol dehydration to cyclohexene on HZMS-5, in which the hydroxyl group (OH) is removed as water. The final step involves cyclohexene rapidly hydrogenated to cyclohexane, which is in agreement with the pathways the reported for phenol hydrogenation over Pd/C with H_3PO_4.[22] The proposed phenol hydrogenation pathways are drawn in **Scheme 1.5**.
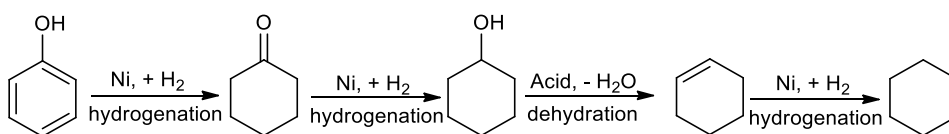
Scheme 1.5. Reaction sequence of phenol hydrodeoxygenation to cyclohexane over supported Ni catalysts in the aqueous phase.[21]

1.3.6. Advantages of highly dispersed metal/zeolite catalysts

The highly dispersed metal/zeolite catalysts play a vital role in improving catalytic activity, selectivity and stability in industrial application. Compared with conventional metal catalysts, the better catalytic performance of highly dispersed metal/zeolite catalyst results from their highly ordered porous characteristic and more active metal sites for electron transfer. The objective of utilizing zeolite is to disperse the main metal particle on a suitable

support to make the catalytic nanoparticle stable for ideal performance and to ensure low cost of metal used which in turns decreases the overall catalysts expenses.

Furthermore, the high surface area and highly ordered crystal structure of zeolite can affect the dispersion of the metallic particles thus increasing its stability against sintering. For instance, Song *et al.* prepared Ni/HBEA samples with different particle sizes and dispersions (**Figure 1.10**) to study the impact of Ni particle size and distribution on the hydrodeoxygenation of microalgae oil. They reported that the small-sized metal particles led to higher catalytic activity, and the more uniform particle distribution ensured better stability of the catalyst in studied reaction. Consequentially, a bifunctional catalyst with well-dispersed metal on the zeolite would make it a suitable and efficient material in the practical application.
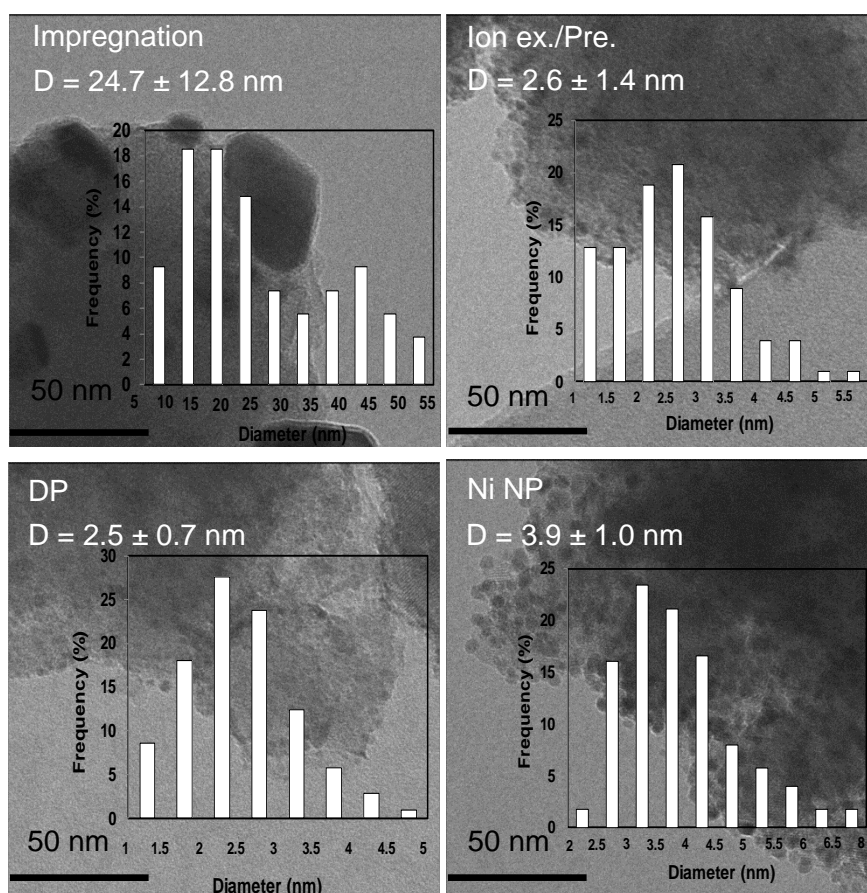
Figure 1.10. TEM images of Ni/HBEA samples prepared by different methods.[37]

1.3.7. Bifunctional Pt/MFI catalyst in phenol hydrogenation reaction

Pt/MFI refers to a bifunctional catalyst with Pt cluster supported on MFI-type zeolite. MFI-type zeolite is a medium pore zeolite with channels defined by ten-membered rings, belonging to the pentasil family of zeolites. Most well-known MFI-type zeolite is ZSM-5 (Zeolite Socony Mobil-5) which was first synthesized in 1969 and patented by Mobil Oil Company in 1972.[46] The framework of ZSM-5 zeolite contains a novel configuration of AlO_4- and SiO_4 tetrahedra linked together by eight five-membered rings. Whereas purely siliceous form of MFI-type zeolite composed with only SiO_4 tetrahedra is named as Silicalite. The MFI elementary units form pentasil chains by joining through the corner sharing of oxygen atoms to oxygen bridge, and then the chains connect to form sheets in the same way.[47] Eventually, MFI structure is formed when the sheets are linked to a center of inversion. The structure of MFI framework is shown in **Figure 1.11**.
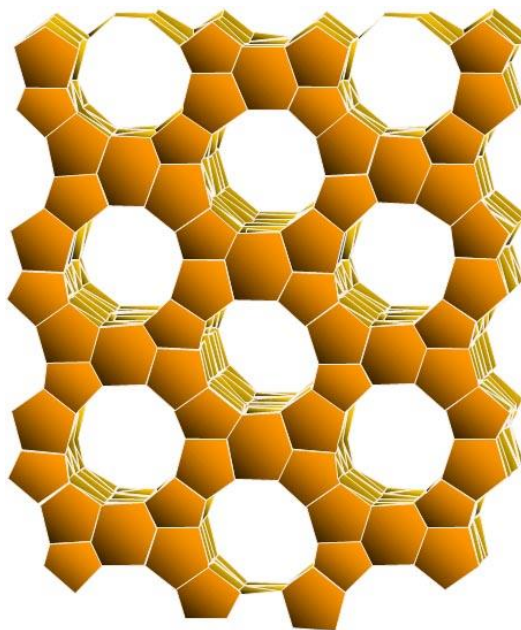
Figure 1.11. MFI framework structure.

Zeolites with MFI framework structure have been widely used as active catalysts and/or supports for a variety of reactions such as cracking, aromatization, dehydration, alkylation, isomerization of hydrocarbons *etc.*, due to their acidity, shape selectivity, ion-exchanging properties and special pore structure (i.e. the 3-dimensional micropore topology and large specific surface area in ZSM-5). Furthermore, given currently increasing industrial oily

wastewater and frequent oil spill accidents, MFI-type zeolites can be used for oil–water separation in the field of environmental protection and chemical industrial process, by varying Si/Al ratio of their composition to be moderately hydrophilic or highly hydrophobic. For instance, Yu and his co-workers firstly prepared nanosized Silicalite-1, based on which they sequentially developed a facile and straightforward way to fabricate zeolite-coated mesh films (ZCMFs) with superhydrophilicity and underwater superhydrophobicity (**Fig.1.12c**). A variety of oils can be separated efficiently from a mixture of oil and water based on the gravity-driven separation process, as shown in **Fig.1.12 (a – b)**.[48]
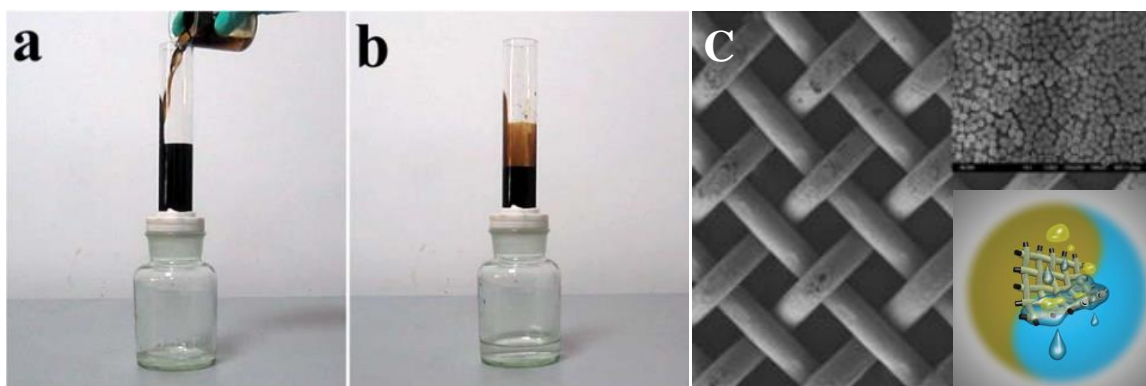
Figure 1.12. Oil–water separation studies of ZCMF-12 which was fixed between two Teflon flanges. (a) The crude oil–water mixture was poured into the glass tube. (b) After separation, water selectively permeated but crude oil was intercepted by the film. (c) SEM images of ZCMF-12 prepared by seeding and secondary growth process of nanosized Silicalite-1.[48]

Besides altering hydrophilicity and hydrophobicity, varying Si/Al ratio of MFI zeolite will also change its acidity, which is generated by framework tetrahedral Si atom substitution by Al. As a primary acid integrant of zeolite, BAS density will be varied accordingly by changing Si/Al ratio, because of its location at the bridging OH between the silicon and aluminum. Therefore it provides one possibility to modify the BAS of MFI zeolite, consequentially facilitating acid-catalyzed reactions. In other cases, the thermal and hydrothermal stability can also be improved by increasing the Si/Al ratio.

Based on the discussion above, it can be concluded that the Brønsted acid properties have a significant influence on the catalytic performance of MFI zeolite in heterogeneous catalysis, and some further modification treatments for the parent zeolite, such as

dealumination, silanization, steaming, alkali-treatment, *etc.*, can optimize its acid properties thereby improving its catalytic performance.[33, 49-54]

Pt-based catalysts，as its high catalytic activity for a broad range of substrates have led to their abundant utilization in vast critical industrial processes, such as hydrogenation and dehydrogenation reactions in the pharmaceutical industry, reforming reactions in the petroleum refining industry, organic oxidation reactions and inorganic oxidation reactions.[55-58] Besides being an excellent catalyst for chemical manufacturers mentioned above, the Pt-based catalyst is also used as automotive emission control catalyst which contributes a positive impact on the environment.[59-65] Pt-based catalysts also play a vital role in treating volatile organic compounds emitted from many industrial processes. Furthermore, platinum, as one of the most common composite electrodes, has been deeply developed and largely applied in electrochemistry, like in fuel cells.[66, 67]

Among the catalytic features of Pt, hydrogenated capacity is an essential character of Pt in catalytic reactions, which generally involves in dissociative adsorption of H_2 and H-addition steps on the Pt surface. Since hydrogenation reaction over Pt will be detailedly discussed in this thesis, it is necessary to understand the steps involving the reaction of platinum with surrounding hydrogen. Taking hydrogenation of alkenes as an example, the whole process mostly proceeds in three steps which involve H_2 dissociative adsorption, hydrogen addition and products desorption (**Figure 1.13**). Specifically, H_2 molecules from the surrounding are firstly adsorbed on the platinum surface, generally dissociated into active hydrogen atoms. Subsequently, the active hydrogen atom was added to the adsorbed alkene generating the alkane on the platinum surface. In the end, the formed alkane molecules desorb from the Pt surface and diffuse into the reaction system.
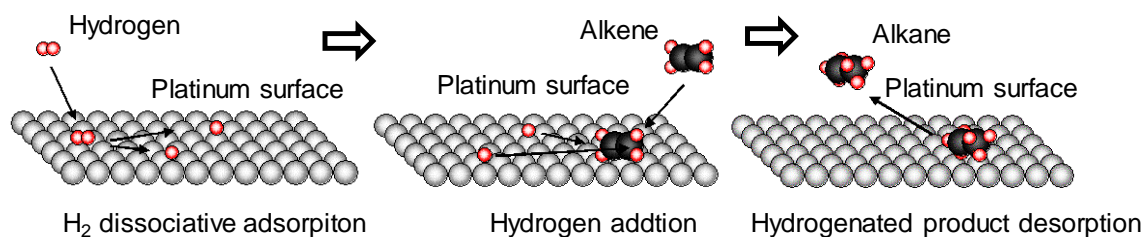
Figure 1.13. Hydrogenation of alkene on platinum surface.[68]

Due to its high catalytic performance, resistance to high-temperature corrosion and oxidation, Pt has become an essential component for the preparation of bifunctional catalysts. Moreover, various studies have shown that it is feasible to load nanosized Pt clusters (1 nm) on the support via common synthesis strategies (IE and incipient impregnation). For example, Philippaerts *et al.* prepared 1 – 2 nm sized Pt clusters encapsulated in the lattice of the HMFI zeolite (**Figure 1.14a**) via competitive ion exchange method followed by curtail activation procedures.[38] Kim *et al.* also obtained ∼ 1nm Pt clusters occluded in HMFI samples by similar ion exchange method (**Figure 1.14b**).[69]
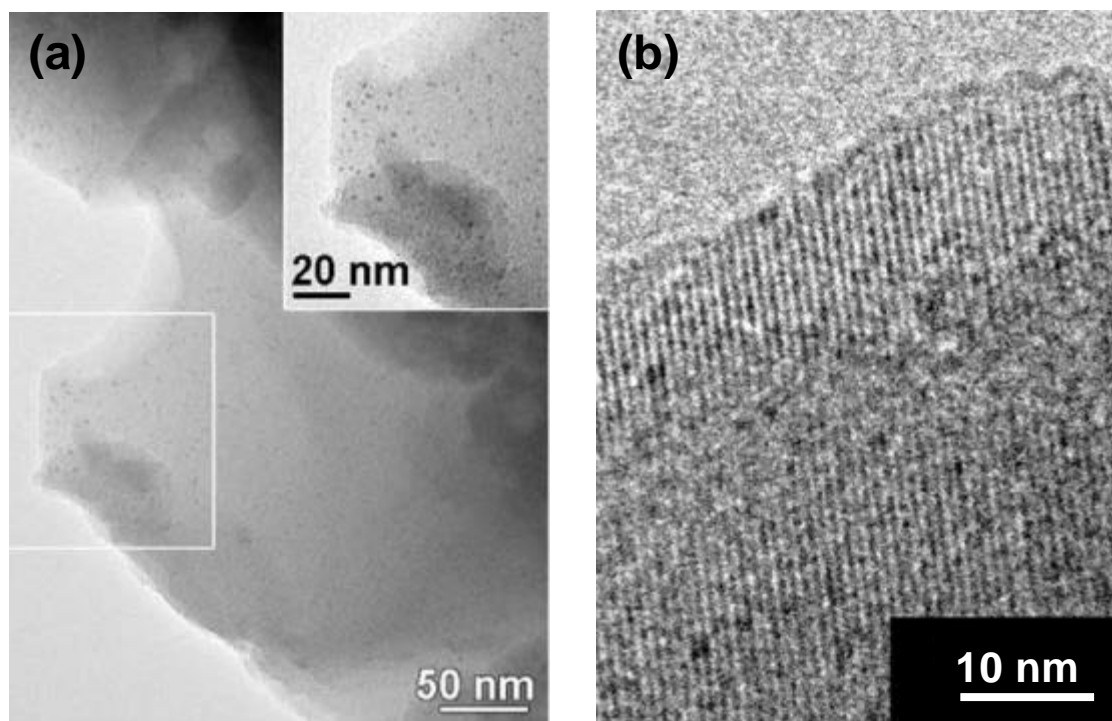
Figure 1.14. TEM images of 1nm Pt cluster occluded in MFI-type zeolite via ion exchange method by (a) Philippaerts *et al.*[38] and (b) Kim *et al.*.[69]

The well-dispersed Pt encapsulated in MFI samples can provide vast active sites for reaction system thus improving the reaction rate. Moreover, it could also cooperate with BAS located in the MFI to expose impacts on related reaction. In the past decades, many studies reported the acidity of support could improve the metal-catalyzed reaction.[70-75] However, the nature of this acid promotion effect still remains unclear, because most of

the catalysts reported containing large metal particles which are too large to enter the micropores of zeolite and not easy to cooperate with the BAS over there. Therefore, it is necessary to prepare the Pt encapsulated in the zeolite samples to figure out the interaction of Pt with BAS in the Pt/MFI catalysts well as their synergistic effect in heterogeneous reaction. The synthesis of high-dispersed Pt/MFI sample with different BAS concentrations will be the subject of interests in the second chapter of this thesis.

To investigate the synergistic effect between Pt and BAS, phenol as a simplest phenolic monomer from bio-derived compounds was chosen to be tested in aqueous phase hydrogenation reactions. The hydrogenation of phenol over Pt/HMFI catalyst involves similar steps as that over Ni/HBEA, actually including one dehydration step by acid. Firstly, phenol is adsorbed on Pt clusters and the double bond in the aromatic ring is hydrogenated by the active H atom which is from the dissociative adsorption of H_2, then forming cyclohexone. Due to Keto-Enol tautomerization, the ketone is then hydrogenated to cyclohexanol.[76] Afterward, the alcohol group (OH) will be removed as water and converted to cyclohexene in the presence of hydronium ion which is the form of BAS in aqueous phase[26]. The final step involves cyclohexene rapidly hydrogenated to cyclohexane. **Scheme 1.6** shows the schematic representation of proposed phenol hydrogenation pathways over Pt/HMFI catalysts.
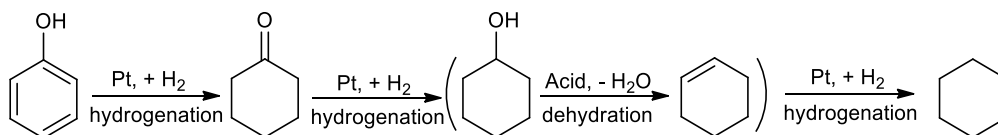
Scheme 1.6. Sequential pathways of phenol hydrogenation reactions over Pt/HMFI samples.

Basically, detailed kinetic studies could provide enough elemental knowledge involving reaction rates, reaction orders and intrinsic energy barriers for interpreting the influence of BAS on Pt-catalyzed phenol hydrogenation reactions. Transition state theory (TST) was applied, which assumes a possible transition state (activated complex) existing between reactants and products during a chemical reaction and a quasi-equilibrium between the reactant and the transition state. In addition, Eyring equation was used to calculate the

activation enthalpy and activation entropy according to the experimentally determined rate constant.

$$k_{rnx} = \frac{k_B T}{h} e^{\Delta S^{\ddagger}/R} e^{-\Delta H^{\ddagger}/RT} \qquad (1.1)$$

By taking the natural logarithm of both sides of Equation 1, the equation can be rearranged to fit the equation of a straight line (Eq.1.2).

$$\ln\left(\frac{k_{rnx}}{T}\right) = \left(\ln\frac{k_B}{h} + \frac{\Delta S^{\ddagger}}{R}\right) - \frac{\Delta H^{\ddagger}}{R}\left(\frac{1}{T}\right) \quad (1.2)$$

where k_{rnx} represents the rate coefficient; R is the universal gas constant with a value of 8.314 J·mol^{-1} K^{-1}; and T is the absolute temperature in a given reaction in Kelvin; $\Delta H^{\ddagger}$ and $\Delta S^{\ddagger}$ refer to enthalpy and entropy of activation; k_B is Boltzmann constant; h is Planck's constant is the minimum amount of energy.

The enthalpy and entropy of activation can be calculated by plotting $\ln\left(\frac{k_{rnx}}{T}\right)$ against $\frac{1}{T}$ using Equation 1.2.

1.4. Scope of this thesis

The major purpose of this dissertation is the preparation of sub-nanosized Pt encapsulated in MFI-type zeolite with different BAS concentrations and their applications for hydrogenation of phenol. Meanwhile, the individual and cooperative roles of metal and acid sites are explored by studying reaction kinetics.

In the second chapter of this thesis, a series of Pt/MFI with different BAS concentration were prepared via impregnation and ion exchange methods. The catalysts were extensively characterized by the STEM, XAS, H$_2$ chemisorption, IR, *etc.*. The encapsulation of sub-nanosized Pt in MFI samples was highlighted by STEM images. The interaction of Pt and BAS was observed by both IR-CO and XANES measurements.

In the following chapter, a novel kinetic method was developed to determine adsorption heat of H$_2$ on Pt/MFI in the aqueous phase. The detailed kinetics and thermodynamics of H/D exchange reaction between gas H$_2$ and liquid D$_2$O over Pt/HMFI-24 and Pt/Silicalite-1 catalysts were investigated in details, including elementary steps, reaction rates, rate

constants, H_2 adsorption equilibrium constant, H_2 adsorption energy barrier, H_2 desorption energy barrier and H_2 adsorption heat. The influence of water and BAS from support on H_2 adsorption over Pt surface in the aqueous phase were also discussed in details.

Apart from H_2 adsorption process, hydrogenation of phenol over Pt/MFI samples with varying BAS concentrations was tested in the aqueous phase. The impact of hydronium ion, i.e. the form of BAS in water, on the Pt-catalyzed hydrogenation was explored by detailed kinetic studies. The different pathways of phenol hydrogenation were proposed in the presence or absence of BAS. In addition, the role of hydronium ions in the phenol hydrogenation over Pt/HMF catalysts was addressed as well.

The final chapter concluded the general findings from this thesis where we had prepared well-dispersed Pt supported on MFI zeolites with different BAS concentrations and tested in aqueous phase phenol hydrogenation reactions. Catalysts with higher hydronium ion concentrations in MFI micropores showed weaker adsorption phenol, but higher hydrogenation activity. In the presence of hydronium ion, protonation of the aromatic ring coupled with electron transfer led to a higher rate than the conventional addition of hydrogen atom.

1.5. Associated content

Figure 1.4 and **1.5** reprinted with permission from (V. Menon, M. Rao, *Prog. Energy Combust. Sci.,* 38 (**2012**) 522-550.). License number: 4126440146447.

Figure 1.6 and **Scheme 1.1−1.2** reprinted with permission from (P. M. Mortensen, J. D. Grunwaldt, *Applied Catalysis A: General*., 407 (**2011**) 1-19.). License number: 4126440410941.

Figure 1.7 reprinted with permission from (C. Zhao, W.J. Song, J.A. Lercher, *ACS Catal,* 2 (**2012**) 2714-2723.). Copyright (2012) American Chemical Society.

Table 1.1 reprinted with permission from (C. Zhao, J.A. Lercher, *Angew. Chem. Int. Ed.,* 51 (**2012**) 5935-5940.). License number: 4126460438705.

Figure 1.8 reprinted with permission from (E. Koohsaryan, M. Anbia, *Chinese Journal of Catalysis,* 37 (**2016**) 447-467.). License number: 4126460722144.

Figure 1.10 reprinted with permission from (C. Zhao, Y. Kou, A.A. Lemonidou, X.B. Li, J.A. Lercher, *Angew. Chem. Int. Ed.,* 48 (**2009**) 3987-3990.). License number: 4126461251047.

Figure 1.11 and Scheme **1.4** reprinted with permission from (W.J. Song, C. Zhao, J.A. Lercher, *Chem-Eur J,* 19 (**2013**) 9833-9842.). License number: 4102531079477.

Scheme 1.5 reprinted with permission from (C. Zhao, S. Kasakov, J.Y. He, J.A. Lercher, *J. Catal.,* 296 (**2012**) 12-23.). License number: 4126470130492.

Figure 1.13 reprinted with permission from (Q. Wen, J.C. Di, L. Jiang, J.H. Yu, R.R. Xu, *Chem Sci,* 4 (**2013**) 591-595.). License number: 4126470398610.

Figure 1.15 reprinted with permission from (A. Philippaerts, S. Paulussen, S. Turner, *et al.*, *J. Catal.,* 270 (**2010**) 172-184. and J. Kim, W. Kim, Y. Seo, *et al.*, *J. Catal.,* 301 (**2013**) 187-197.). License number: 4126470713637 and 4126470929854.

1.6. References

[1] U.S. EIA, https://www.eia.gov/outlooks/ieo/, *The International Energy Outlook 2016*, (**2016**) p.9.

[2] U.S. EIA, https://www.eia.gov/energyexplained/?page=us_energy_home, *Monthly Energy Review April*, (**2016**) p.7.

[3] C. Morris, https://energytransition.org/2015/07/biomass-growth-is-over/, *Energy Transition*, (**2015**).

[4] R. Wilson, http://www.theenergycollective.com/robertwilson190/370286/biomass-worlds-biggest-provider-renewable-rnergy, *The Energy Collective*, (**2014**).

[5] J.R. Regalbuto, *Science,* 325 (**2009**) 822-824.

[6] P. Phitsuwan, K. Sakka, K. Ratanakhanokchai, *Biomass Bioenergy,* 58 (**2013**) 390-405.

[7] P.R. Norton, P.J. Richards, *Surf. Sci.,* 44 (**1974**) 129-140.

[8] V. Menon, M. Rao, *Prog. Energy Combust. Sci.,* 38 (**2012**) 522-550.

[9] J.S. Van Dyk, B.I. Pletschke, *Biotechnol. Adv.,* 30 (**2012**) 1458-1480.

[10] R. Hickey, US20150225749 A1, US 14/176,013, US, **2014**

[11] J.I. Alves, A.J.M. Stams, C.M. Plugge, *et al.*, *FEMS Microbiol. Ecol.,* 86 (**2013**) 590-597.

[12] W.N.R.W. Isahak, M.W.M. Hisham, M.A. Yarmo, *et al.*, *Renewable and Sustainable Energy Reviews,* 16 (**2012**) 5910-5923.

[13] F. Behrendt, Y. Neubauer, M. Oevermann, *et al.*, *Chemical Engineering & Technology,* 31 (**2008**) 667-677.

[14] P.M. Mortensen, J.D. Grunwaldt, P.A. Jensen, *et al.*, *Applied Catalysis A: General,* 407 (**2011**) 1-19.

[15] Y. Romero, F. Richard, S. Brunet, *Applied Catalysis B: Environmental,* 98 (**2010**) 213-223.

[16] C. Zhao, W.J. Song, J.A. Lercher, *ACS Catal,* 2 (**2012**) 2714-2723.

[17] M. Sankar, N. Dimitratos, P.J. Miedziak, *et al.*, *Chem. Soc. Rev.,* 41 (**2012**) 8099-8139.

[18] P. Barbaro, F. Liguori, N. Linares, *et al.*, *Eur. J. Inorg. Chem.,* (**2012**) 3807-3823.

[19] C. Zhao, D.M. Camaioni, J.A. Lercher, *J. Catal.,* 288 (**2012**) 92-103.

[20] C. Zhao, Y. Kou, A.A. Lemonidou, *et al.*, *Chem. Commun.,* 46 (**2010**) 412-414.

[21] C. Zhao, S. Kasakov, J.Y. He, *et al.*, *J. Catal.,* 296 (**2012**) 12-23.

[22] C. Zhao, Y. Kou, A.A. Lemonidou, *et al.*, *Angew. Chem. Int. Ed.,* 48 (**2009**) 3987-3990.

[23] C. Zhao, J.Y. He, A.A. Lemonidou, *et al.*, *J. Catal.,* 280 (**2011**) 8-16.

[24] C. Zhao, J.A. Lercher, *Angew. Chem. Int. Ed.,* 51 (**2012**) 5935-5940.

[25] C. Zhao, J.A. Lercher, *Chemcatchem,* 4 (**2012**) 64-68.

[26] A. Vjunov, M.A. Derewinski, J.L. Fulton, *et al.*, *J. Am. Chem. Soc.,* 137 (**2015**) 10374-10382.

[27] C.T. Kresge, M.E. Leonowicz, W.J. Roth, *et al.*, *nature,* 359 (**1992**) 710-712.

[28] C.C. Freyhardt, M. Tsapatsis, R.F. Lobo, *et al.*, *Nature,* 381 (**1996**) 295.

[29] S.D. Sims, D. Walsh, S. Mann, *Adv. Mater.,* 10 (**1998**) 151-154.

[30] M.S. Holm, E. Taarning, K. Egeblad, *et al.*, *Catal. Today,* 168 (**2011**) 3-16.

[31] Y. Tao, H. Kanoh, L. Abrams, *et al.*, *Chem. Rev.,* 106 (**2006**) 896-910.

[32] J. Cravillon, R. Nayuk, S. Springer, *et al.*, *Chem. Mater.,* 23 (**2011**) 2130-2141.

[33] E. Koohsaryan, M. Anbia, *Chinese Journal of Catalysis,* 37 (**2016**) 447-467.

[34] B.-Z. Zhan, M.A. White, M. Lumsden, *et al.*, *Chem. Mater.,* 14 (**2002**) 3636-3642.

[35] M. Shibasaki, M. Kanai, S. Matsunaga, *et al.*, *Acc. Chem. Res.,* 42 (**2009**) 1117-1127.

[36] S. Rojas, Preparation of Catalysts, Spanish National Research Council, Spain, (**2013**).

[37] W.J. Song, C. Zhao, J.A. Lercher, *Chem-Eur J,* 19 (**2013**) 9833-9842.

[38] A. Philippaerts, S. Paulussen, S. Turner, *et al.*, *J. Catal.,* 270 (**2010**) 172-184.

[39] J.W.G. L. A. M. Hermans, Preparation of Catalysts II Elsevier, Amsterdam, (**1979**).

[40] Ö. Metin, V. Mazumder, S. Özkar, *et al.*, *J. Am. Chem. Soc.,* 132 (**2010**) 1468-1469.

[41] H. Lee, H. Kim, M.J. Yu, *et al.*, *Scientific Reports,* 6 (**2016**).

[42] N. Mahata, K.V. Raghavan, V. Vishwanathan, *Appl Catal a-Gen,* 182 (**1999**) 183-187.

[43] S. Scire, C. Crisafulli, R. Maggiore, *et al.*, *Appl. Surf. Sci.,* 136 (**1998**) 311-320.

[44] S. Scire, S. Minico, C. Crisafulli, *Appl Catal a-Gen,* 235 (**2002**) 21-31.

[45] N.C. Nelson, J.S. Manzano, A.D. Sadow, *et al.*, *Acs Catal,* 5 (**2015**) 2051-2061.

[46] R.J. Argauer, G.R. Landolt, 14 Nov. (**1972**).

[47] S. Bhatia, Zeolite catalysts: principles and applications, CRC press, (**1989**).

[48] Q. Wen, J.C. Di, L. Jiang, *et al.*, *Chem Sci,* 4 (**2013**) 591-595.

[49] Q. Zhou, Y.-Z. Wang, C. Tang, *et al.*, *Polym. Degrad. Stab.,* 80 (**2003**) 23-30.

[50] N. Rahimi, R. Karimzadeh, *Applied Catalysis A: General,* 398 (**2011**) 1-17.

[51] M. Conte, J.A. Lopez-Sanchez, Q. He, *et al.*, *Catal Sci Technol,* 2 (**2012**) 105-112.

[52] E.O. Altynkovich, O.V. Potapenko, T.P. Sorokina, *et al.*, *Petroleum Chemistry,* 57 (**2017**) 215-221.

[53] M. Ogura, S.-y. Shinomiya, J. Tateno, *et al.*, *Applied Catalysis A: General,* 219 (**2001**) 33-43.

[54] J.C. Védrine, A. Auroux, P. Dejaifve, *et al.*, *J. Catal.,* 73 (**1982**) 147-160.

[55] W. Yu, M.D. Porosoff, J.G. Chen, *Chem. Rev.,* 112 (**2012**) 5780-5817.

[56] C. Masters, Homogeneous transition-metal catalysis: a gentle art, Springer Science & Business Media, (**1981**).

[57] K. Pirkanniemi, M. Sillanpää, *Chemosphere,* 48 (**2002**) 1047-1060.

[58] L. Zhang, J. Sun, S.A. Kozmin, *Adv. Synth. Catal.,* 348 (**2006**) 2271-2296.

[59] R. Burch, J.P. Breen, F.C. Meunier, *Applied Catalysis B: Environmental,* 39 (**2002**) 283-303.

[60] D.K. Captain, M.D. Amiridis, *J. Catal.,* 184 (**1999**) 377-389.

[61] R. Burch, A.A. Shestov, J.A. Sullivan, *J. Catal.,* 188 (**1999**) 69-82.

[62] R. Burch, A.A. Shestov, J.A. Sullivan, *J. Catal.,* 186 (**1999**) 353-361.

[63] A.A. Shestov, R. Burch, J.A. Sullivan, *J. Catal.,* 186 (**1999**) 362-372.

[64] R. Burch, J.A. Sullivan, *J. Catal.,* 182 (**1999**) 489-496.

[65] R. Burch, A.A. Shestov, J.A. Sullivan, *J. Catal.,* 182 (**1999**) 497-506.

[66] S. Zhang, X.-Z. Yuan, J.N.C. Hin, *et al.*, *J. Power Sources,* 194 (**2009**) 588-600.

[67] S. Shrestha, Y. Liu, W.E. Mustain, *Catalysis Reviews,* 53 (**2011**) 256-336.

[68] M. Blaber, "*Chemical Kinetics"*, (**2000**).online avaliable, in
http://www.mikeblaber.org/oldwine/chm1046/notes/Kinetics/Catalyst/Catalyst.htm

[69] J. Kim, W. Kim, Y. Seo, *et al.*, *J. Catal.,* 301 (**2013**) 187-197.

[70] G. Larsen, G.L. Haller, *Catal. Lett.,* 3 (**1989**) 103-110.

[71] Z. Karpinski, S.N. Gandhi, W.M.H. Sachtler, *J. Catal.,* 141 (**1993**) 337-346.

[72] W.J. Song, Y.S. Liu, E. Barath, *et al.*, *Green Chemistry,* 17 (**2015**) 1204-1218.

[73] R. Wang, Y.H. Li, R.H. Shi, *et al.*, *J Mol Catal a-Chem,* 344 (**2011**) 122-127.

[74] A. Masalska, J.R. Grzechowiak, K. Jaroszewska, *Top. Catal.,* 56 (**2013**) 981-994.

[75] F. Hoxha, B. Schimmoeller, Z. Cakl, *et al.*, *J. Catal.,* 271 (**2010**) 115-124.

[76] P.M. de Souza, R.C. Rabelo-Neto, L.E.P. Borges, *et al.*, *ACS Catal,* 5 (**2015**) 1318-1329.

Chapter 2

Synthesis and characterization of Pt clusters encapsulated within MFI zeolites

Five Pt/MFI samples with the varying Si/Al ratios were prepared by ion exchange and a specific wetness impregnation method. IR spectroscopy of CO and Pyridine adsorption, STEM, H_2 chemisorption and XAS analysis (XANES and EXAFS) were applied to characterize the properties of the five Pt/MFI samples. The BAS concentrations of the supports were in the range of 658 – 0 $\mu mol \cdot g^{-1}$ and the LAS concentrations were below 50 $\mu mol \cdot g^{-1}$. STEM images suggested that the Pt loading method followed by careful activation procedure ensured a well-dispersed Pt clusters which were encapsulated in the MFI micropores. The electron deficiency of Pt supported on H-MFI-24 (Si/Al = 24) was determined by both IR-CO and XANES analysis. The interaction between BAS and Pt cluster was determined via H/D exchange between D-form BAS and H_2 over Pt/MFI samples, which was in agreement with IR-CO and XANES results.

2.1. Introduction

Platinum catalysts are important materials for green chemistry and car exhaust treatment. [1, 2] Under most of the reaction conditions, the catalytic reaction centers, Pt nanoparticles, are unfortunately subject to deactivation due to leaching, sintering, poisoning or agglomeration of the Pt clusters. Some methods, such as loading on acid or basic support and adding certain promoters to the catalysts, were reported to be able to stabilize the Pt catalysts and avoid the deactivation in reactions.[3-7]

The control of Pt location on the support affects the catalytic activity of Pt catalyst. Firstly it adjusts the accessibility of the Pt metal to the reactants. Secondly, it also limits Pt agglomeration by improving the Pt clusters distribution. Given the importance of Pt location in the catalyst system, a promising strategy is locating the Pt clusters on/in zeolite supports, because the highly ordered porosity of zeolite can help to improve the distribution of Pt by confining the Pt clusters in the channels or pores of the zeolite and contribute the size and shape selectivity to reactants and products. However, conventional preparation methods can not provide enough certainty to control Pt location in the zeolite. For example, the location of the Pt nanoparticles on the MFI support could be at micropores, mesopores or outer surface. Each case may lead to different size and distribution of Pt particles after thermal synthesis or activation processes.[8]

Encapsulating Pt clusters within micropores of MFI-type zeolite can not only prevent them from sintering and contacting with toxic impurities,[8] but can help Pt active sites to select reactants, transition states and products on the basis of molecular size and shape as well.[9-12] However, it is difficult to encapsulate such Pt clusters within MFI micropores via post-synthesis exchange from aqueous or vapor media, because the size of cationic or anionic precursors surrounded by water molecules and their charge-balancing double layer, or the size of gaseous complexes prevents their diffusion through the apertures of the microporous MFI. Furthermore, the encapsulation requires that precursors can be placed and retained within microporous frameworks during hydrothermal syntheses and subsequent post-treatment.[9]

Given these factors, Iglesia and his co-workers firstly developed a synthesis strategy for the encapsulation of noble metals and their oxides within SOD (Sodalite, 0.28 nm × 0.28 nm), GIS (Gismondine, 0.45 nm × 0.31 nm), and ANA (Analcime, 0.42 nm × 0.16 nm) zeolites via direct hydrothermal synthesis using metal precursors stabilized by ammonia or organic amine ligands, which avoided their decomposition or precipitation as colloidal hydroxides at the conditions of hydrothermal synthesis (< 380 K) and favored interactions between metal precursors and incipient aluminosilicate nuclei during self-assembly of microporous frameworks.[13] Afterward, they reported another approach to encapsulate metal clusters (Pt, Ru, Rh) within MFI by exchanging cationic metal precursors into a parent zeolite (BEA, FAU), reducing them with H_2 to form metal clusters and transforming these zeolites into daughter structures of higher framework density (MFI) under hydrothermal conditions.[10]

Philippaerts *et al.* prepared Pt clusters encapsulated in the lattice of the MFI zeolite crystal via competitive ion exchange method followed by the rigorous activation process. It is shown that the calcination in O_2 (purity ≥ 99.9999 %) with low heating rate (0.3 K·min^{-1}) is crucial as it allows the Pt-precursors to be slowly transformed into Pt^{2+} and placed in the 8MR pores of MFI. The following careful reduction process in H_2 can reduce Pt^{2+} to Pt^0 in the pores.[14] Luo *et al.* reported a modified wetness impregnation method to load nanosized Ru clusters on HMFI, in which the Ru with support solution was evaporated at 353 K under vigorously stirring.[15]

In this chapter, a series of Pt/MFI catalysts which consist of the nanosized Pt cluster encapsulated in the micropores of MFI with different Brønsted acid site (BAS) concentrations, were prepared via ion exchange and wetness impregnation methods. Various technologies such as STEM, XAS, IR, *etc.* were applied to determine particle size and location of Pt cluster, as well as the interaction of BAS and Pt cluster in Pt/MFI catalysts.

2.2. Experimental

2.2.1. Chemicals and materials

The following chemicals were used as received in this work: $Al(NO_3)_3 \cdot 9H_2O$ (98.0 %, Sigma-Aldrich), NaOH (98.0 %, Sigma-Aldrich), NaCl (99.5 %, Sigma-Aldrich), Na_2SO_4 (99.0 %, Sigma-Aldrich), Tetrapropyl ammonium bromide (TPABr, 98.0 %, Sigma-Aldrich), Tetrapropylammonium hydroxide (TPAOH, 1.0 M in H_2O, Sigma-Aldrich), Tetraethylorthosilicate (TEOS, 99.0 %, Sigma-Aldrich), Ammonium nitrate (99.5 %, Sigma-Aldrich), Ammonium hexafluorosilicate (AHFS, 99.9 %, Sigma-Aldrich), Tetraammineplatinumnitrate (99.9 %, Sigma-Aldrich), Nitrogen (99.999 %, Westfalen), Hydrogen (99.999 %, Westfalen) and Oxygen (99.9999 %, Westfalen)

2.2.2. Preparation of MFI zeolites with varying BAS concentrations

NH_4-MFI (Si/Al = 15) and NH_4-MFI (Si/Al = 25) were purchased from Zeolyst International (CBV3024E, CBV5524G). H-MFI (Si/Al = 120), H-MFI (Si/Al = 430) and Silicalite-1 were home prepared via hydrothermal synthesis as reported.[16, 17]

Hydrothermal synthesis of zeolites

For the synthesis of H-MFI (Si/Al = 120) and H-MFI (Si/Al = 430), 30 mL solution of $Al(NO_3)_3$ (0.21g or 0.42 g of $Al(NO_3)_3 \cdot 9H_2O$ for H-MFI with Si/Al of 430 or 120) was added into 30 ml solution of NaOH (3.0 g). Then it was mixed with another 70 ml solution which contained 14.8 g TPABr and 1.51 g NaOH, followed by stirring vigorously at room temperature for an hour. Afterward, 20.0g of silicon dioxide was added gradually under vigorous stirring. Then the resulting mixture was aged at room temperature for 20 hours. Eventually, the precursor solution was transferred into an autoclave with a Teflon liner and kept for 48 hours at 448 K.

Silicalite-1 was prepared with a molar ratio of TPAOH : TEOS : EtOH : H_2O = 9 : 25 : 100 : 480. Specifically, 9 ml of TPAOH was added into a flask along with 1.4ml of H_2O followed by stirring at room temperature for 15minutes. Afterward, under stirring, TEOS

was added to the mixture dropwise. In the end, the clear reaction solution was sealed in a 100 mL polypropylene bottle and conducted at 363 K for 4 days.

After hydrothermal synthesis, the resulting zeolites was purified by repeated washing with distilled water until the pH of washing water was close to 7 and then dried in the oven overnight (373 K). Calcination was carried out in the synthetic air to remove the organic template at 773 K for 5 hours.

Subsequently, the as-synthesized samples were ion-exchanged three times using 150 mL of a 1 M NH_4NO_3 solution at 353 K for 2 h, to produce NH_4-MFI zeolites. Finally, the samples were calcined for 5 h at 823 K under synthetic air to generate H-MFI samples

AHFS treatment

AHFS treatment was applied to remove extra-framework alumina. In details, two commercial NH_4-MFI (Si/Al ratio =15 and 25) were respectively added to a solution of $(NH_4)_2SiF_6$ (AHFS) at 353 K and then stirred vigorously for 5 h. The solution contained a 4-fold excess of AHFS with respect to the Al-content of the sample. After the treatment, the samples were washed six times at 353 K with deionized water and calcined for 5 h at 823 K under flowing synthetic air (100 ml min^{-1} g^{-1}, heating rate 10 K min^{-1}).

The H-MFI sample is denoted as H-MFI-X, with "X" referring to the Si/Al (atom/atom) ratio.

Loading Pt on MFI samples

Pt/HMFI-24 and P/HMFI-40 catalysts were prepared by ion exchange (IE) method.[14] Briefly, 100 mL aqueous solution of $Pt(NH_3)_4(NO_3)_2$ (0.022g) was mixed with 1 g calcined zeolite. The slurry was stirred at room temperature for 24 hours. Afterward the solid was separated from the solution by filtration and was then washed three times with distilled water followed by drying at 353 K overnight. Then the Pt-loaded sample was carefully calcined under 150 mL·min^{-1} O_2 (purity $\geq$ 99.9999%) firstly at 373 K for 1 h with secondly increasing to 623 K at 0.3 K·min^{-1} and holding for 2 hours, then cooled to room temperature. The catalyst was flushed with N_2 for 1 h before reduction under the flow of H_2. Afterward, pure hydrogen (150 mL·min^{-1}) was flowed in for the reduction. The samples were heated

to 623 K with a heating rate of 0.4 K·min^{-1}and kept for 2 h. Finally, the catalyst was cooled down to room temperature and flushed by N_2 again before collection.

For Pt loading on MFI-type samples with low/no Al concentrations (H-MFI-120, H-MFI-430 and Silicalite-1), impregnation method was applied. [15] Typically, 1g of dry H-MFI or Silicalite-1 was slowly added to 25 mL of aqueous solution containing 0.022g $Pt(NH_3)_4(NO_3)_2$ and kept stirring at 303 K for 1 h. Then the temperature was raised to 353 K and kept for 6 h to allow a slow evaporation of the solvent until fine catalyst powder of uniform white color was obtained. The catalyst was calcined and reduced following the same procedures as that for Pt/HMFI-24, and Pt/HMFI-40 described above.

2.2.3. Catalyst characterization

The crystal structures of the zeolite powders were analyzed by X-ray diffraction (XRD) using a Philips X'Pert Pro System, with Cu-Kα1 radiation operating at 45 kV/40 mA. The measurement was carried out with a scanning rate of 0.017º/s and the 2θ range from 5 to 70º.

Scanning electron microscopy (SEM) was performed on a JEOL 500 SEM-microscope.

Elemental analysis for Al, Si and Pt content of the samples was determined by atomic absorption spectroscopy (AAS) on a UNICAM 939 AA–Spectrometer. Prior to measurement, the sample was dissolved in a mixture of hydrofluoric acid (48 %) and nitro-hydrochloric acid at its boiling point.

Specific surface area and porosity characteristics were determined from N_2 adsorption isotherms recorded on an automated PMI Sorptomatic 1990instrument at liquid N_2 temperature (77 K). The samples were outgassed in vacuum ($< 1\times10^{-3}$ mbar) for 2 h at 475 K prior to adsorption. The specific surface areas were calculated by applying the Brunauer-Emmett-Teller (BET) theory, and the pore volumes were determined by the t-plot method.[18]

The infrared spectra of adsorbed pyridine (Py-IR) were used to quantify the acid concentrations on the catalysts. All spectra were collected on a Nicolet 5700 FT-IR

spectrometer at a resolution of 4 cm^{-1}. Catalyst samples were prepared as a self–supporting wafer and loaded in the center of a home-made IR-cell perpendicular to the IR beam. It was pretreated in vacuum ($<10^{-5}$ mbar) at 723 K for 1 h. Afterward, the sample was exposed to 0.1 mbar pyridine for 30 min at 423 K, then physisorbed pyridine was removed by outgassing for 1 hand the IR spectra of chemisorbed pyridine were recorded at 423 K. The concentration of BAS and LAS was quantified by integrating the band area of characteristic vibration bands at 1515 – 1565 cm^{-1} and 1435 – 1470 cm^{-1}, respectively.

The IR spectra of adsorbed CO (IR-CO) were recorded on a Vertex 70 spectrometer, Bruker Optics, at a resolution of 4 cm^{-1}. The catalyst sample was prepared as a self-supporting wafer and activated in vacuum ($p = 10^{-6}$ mbar) for 1 h at 533 K with a heating rate of 5 K·min^{-1}, and subsequently re-reduced in 20 mbar H$_2$ at 573 K for 1h with a heating rate of 5 K·min^{-1}. After re-reduction, the sample was outgassed at 573 K in a vacuum for 30 min. After pretreatment, the system was cooled to 303 K, and a spectrum of the activated sample was recorded. CO was adsorbed with an equilibrium pressure of 1 mbar, followed by outgassing to remove physisorbed CO. The IR spectra were recorded until changes in the spectra were not observed. All spectra during CO adsorption were recorded at 303 K. For a direct comparison of the CO surface coverage, the spectra were normalized by the weight of the respective wafer.

The IR spectra of H/D exchange between D-form BAS (Z-OD) and H$_2$ were obtained on a Vertex 70 spectrometer, Bruker Optics, at a resolution of 4 cm^{-1}. The catalyst sample was prepared as a self-supporting wafer and activated under H$_2$ in vacuum ($p = 10^{-6}$ mbar) for 1 h at 533 K with a heating rate of 5 K·min^{-1}, and subsequently D$_2$O was induced to the IR system at 373 K until the band at 3560 $-$ 3650cm^{-1} (Z-OH) disappeared and a new band (Z-OD) at 2630 $-$ 2690 cm^{-1} appeared completely. After Z-OH had been exchanged to Z-OD, the samples were outgassed at 373 K in a vacuum ($p = 10^{-6}$ mbar) for 1h. Afterward, the D-form catalyst was exposed to H$_2$ at 323 K, and the IR spectra were recorded after a certain time.

The scanning transmission electron microscopy (STEM) was performed on a 200-keV FEI Tecnai instrument. The catalysts were prepared for STEM analysis by lightly crushing each

powder between two glass slides, and gently rubbing a holey carbon grid on the slide. No solutions were used in the preparation to avoid any possible change in catalyst morphology.

The Pt L_{III}-edge XAFS spectra were acquired using 12 min ($k = 18$ Å^{-1}) acquisition times. The data was processed using Athena, part of the iXAFS software package,[19] to remove the background from the $\chi(k)$ oscillations. The Fourier transform of the k-space EXAFS data was fit to a theoretical model (FEFF9) [20] using ARTEMIS.[21] Reference compounds, bulk Pt and PtO_2, [22, 23] were measured and used to analyze the structure of the studied Pt catalysts. Because the EXAFS imaginary $\chi(R)$ plots indicated that there was Pt-structure as far as R = 8, and the TEM images suggested that all studied catalyst samples contained a distribution of Pt particles, the following EXAFS analysis protocol was applied to separate the EXAFS contributions of the "Large" particles that are > 3 nm in diameter and "Small" particles that are < 3 nm in diameter. In order to perform this, I had first fitted (R-range of $1 < R < 8$ and k-weighting of 2) the Pt-foil reference with the Pt model. This fit allowed us to determine the necessary fitting paths as well as the respective values for S_0^2, atom distances and Debye-Waller-Factors (DWFs). Subsequently, all fit parameters were set and the R-range was changed to $4.8 < R < 8$. In this range, only the "Large" particles contributed to the spectral features observed in EXAFS. This fit allowed to determine the fraction of the "Large" particles in each sample. Then a second Pt theoretical model was added to the fit to represent the "Small" particles. While all fitting parameters for the "Large" particles were set including the fraction (amplitude parameter in Artemis) that was determined using the above-mentioned approach, the spectra were fitted using only the first two Pt-Pt paths of the second theoretical model. The amplitude parameter for the "Small" particles was defined as the difference between total and "Large" Pt-particles and represented by Equation 2.1 below:

$$amp_{"Small\ particles"} = 0.965 \cdot (1 - amp_{"Large\ particles"}) \cdot CN_{Pt} \quad \text{(Eq. 2.1)}$$

, where CN_{Pt} is the Pt first shell coordination number of the "Small" particles and 0.965 is the S_0^2 value determined from the Pt-foil reference fit. Therefore the Pt-Pt distances, coordination numbers and DWFs of the "Small" particles were able to be determined.

Near-edge structure (XANES) and extended X-ray absorption fine-structure (EXAFS) measurements were performed at the Pacific Northwest Consortium/X-ray Science Division (PNC/XSD) bending-magnet beamline at Sector 20 of the Advanced Photon Source (APS) at Argonne National Laboratory (ANL). The experiments were performed in transmission mode with a focused beam (0.7×0.6 mm) having a flux of 10^{10} photons through the sample. A harmonic rejection mirror was used to reduce the effects of harmonics. A Pt foil was placed downstream of the sample cell, as a reference to calibrate the photon energy of each spectrum. The catalyst reductions were performed using the microreactor cell and procedures described by Chase *et al.*[24] Glassy-carbon discs, 0.75 mm thick by 3 mm in diameter, were used as the x-ray windows. The catalyst samples were pressed into a pellet, 0.4 mm thick and 3.5 mm in diameter, and held between the windows by a cylindrical tube constructed from porous polyether ether ketone (PEEK) mesh (35 μm^2). Typically, the reactor was purged with H_2 at room temperature using five fill/purge cycles, then pressurized to 50 bar with H_2.

2.3. Results and discussion

2.3.1. Physicochemical properties of catalysts

As shown in **Figure 2.1**, the XRD patterns of as-synthesized MFI samples match well with that simulated from the MFI framework type. The intensities and the width of the reflections peaks vary with the crystal size. The diffraction peaks are sharp and intensified for the H-MFI-120 and H-MFI-430 with coarse particles. While it is relatively broad and weak for the nanoscale crystallites, Silicalite-1. The indication of particle size by XRD is in agreement with SEM analysis, which is introduced in the following.
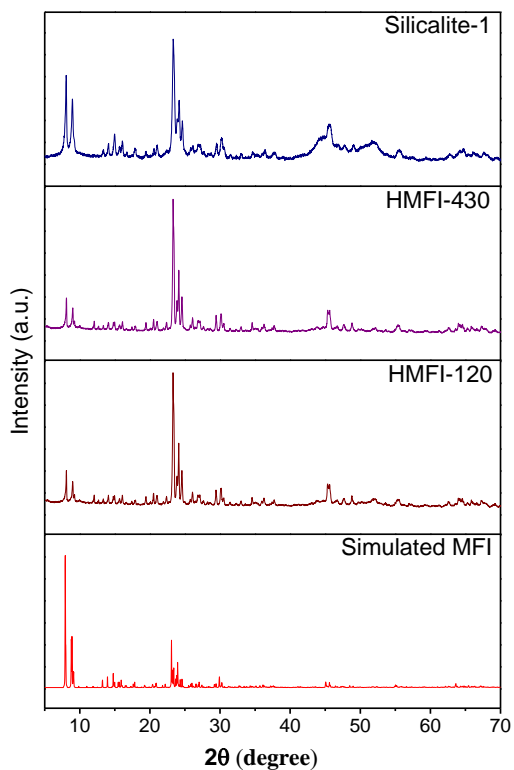
Figure 2.1. XRD patterns of synthesized MFI zeolites with varying Si/Al ratios. The pattern in red is simulated from the MFI-type framework.

SEM images of as-synthesized MFI samples are shown in **Figure 2.2**. Silicalite-1 shows a mean crystallite size of 100 nm, while H-MFI-120 and H-MFI-430 exhibit a similar aggregation morphology with the average crystallite sizes of approximately 2 μm.
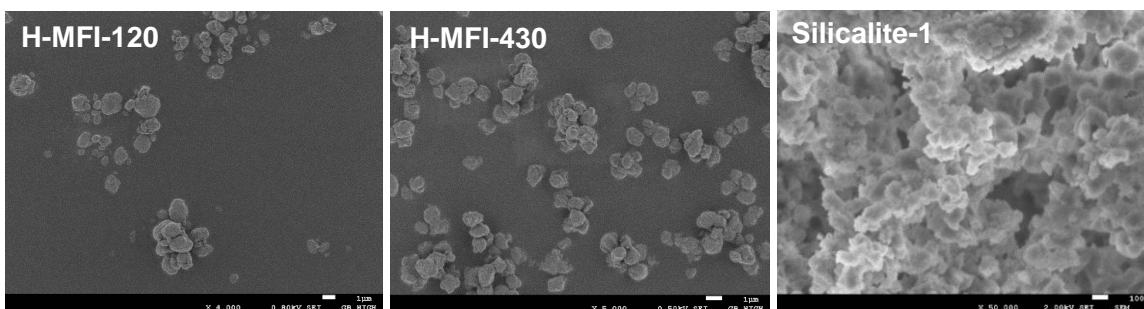
Figure 2.2. SEM images of synthesized MFI-type samples with different Si/Al ratios.

The high amount of extra-framework alumina on two low Si/Al ratio samples, H-MFI-15 and H-MFI-25, was removed by AHFS treatment. The acidic properties of AHFS-treated samples are listed in **Table 2.1**. After the treatment, the characteristic IR vibration bands of extra framework Al-OH at 3656 cm^{-1} and 3780 cm^{-1} disappeared, as shown in **Figure A2.1** and the LAS concentrations obtained by Py-IR analysis decreased from 213 to 56 μmol·g^{-1} for H-MFI-15 and from 137 to 36 μmol· g^{-1} for H-MFI-25. Si/Al ratios of the two samples have increased to be 24 and 40, respectively.

Table 2.1 Acid properties of parent H-MFI and AHFS-treated samples

| Sample	Si/Al[a]	BAS[b]	SBAS[b]	LAS[b]	SLAS[b]
		μmol· g^{-1}			
H-MFI-15	15	843	705	213	168
H-MFI-AHFS-15	24	698	594	56	35
H-MFI-25	25	564	496	137	94
H-MFI-AHFS-25	40	473	461	36	27

[a] Element composition determined with AAS.

[b] Acidic properties measured by IR spectra of adsorbed pyridine (Py-IR).

BET surface areas are comparable for all Pt/HMFI samples, except Pt/Silicalite-1 which shows a bit lower total surface area but much higher mesopore surface area. Notably, the pore volume of Pt-Silicalite-1 (**Table 2.2**) is higher than that of the other four samples, especially the mesopore volume is four times higher than others, which is desirable for Pt distribution in the support, hence resulting in a high dispersion of Pt clusters in Silicalite-1.

Table 2.2. Textural properties of Pt/MFI samples with different acid concentrations.

Catalyst	BET surface area (m^2·g^{-1})			Pore volume (cm^3·g^{-1})		
	Micro	Meso	Total	Micro	Meso	Total
Pt/HMFI-24	391	59	450	0.16	0.11	0.27
Pt/HMFI-40	401	52	453	0.17	0.12	0.29
Pt/HMFI-120	358	86	444	0.14	0.12	0.26
Pt/HMFI-430	354	68	422	0.14	0.06	0.2
Pt/Silicalite-1	176	186	362	0.11	0.47	0.57

The acidic properties of the Pt-loaded catalysts are listed in **Table 2.3.** The concentrations of BAS expectedly decrease from 658 to 0 μmol·g^{-1}with the growing framework Si/Al

ratios of the supports, whereas LAS concentrations are less than 54 μmol·g^{-1} for all five samples.

Table 2.3. Acid properties of Pt/MFI samples measured by IR spectra of adsorbed pyridine.

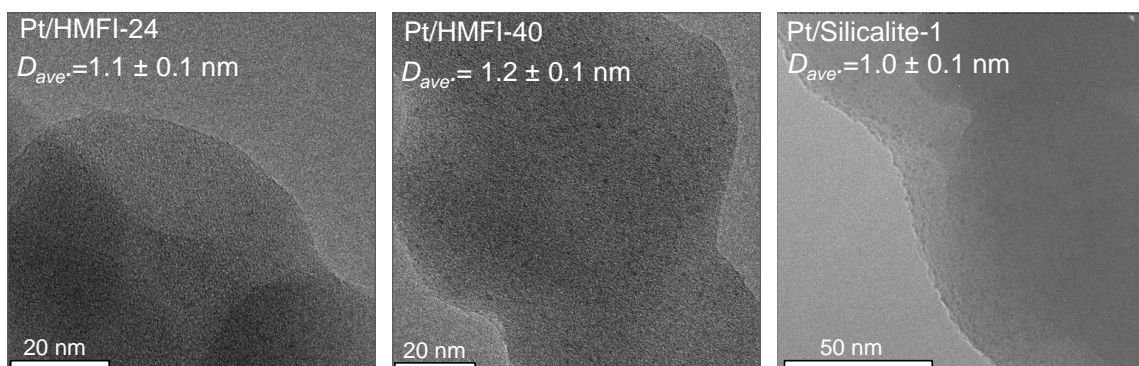| Catalyst	Si/Al [a]	BAS	SBAS	LAS	SLAS	Total
	atom/atom			μmol/g		
Pt/HMFI-24	24	658	572	54	39	712
Pt/HMFI-40	40	414	394	40	29	454
Pt/HMFI-120	116	112	106	34	14	146
Pt/HMFI-430	425	48	45	2.6	2.5	51
Pt/Silicalite-1	∞	0	0	0	0	0

[a] Element composition determined with AAS.

Figure 2.3. TEM images of Pt supported on H-MFI-24, H-MF-40, and Silicalite-1**.**

Pt clusters are visible in all samples with approximately 1.0 to 2.0 nm of particle size. The size and distribution of the Pt particles cross the respective support depending on the loading method used. As reported previously,[14] the slow heating rate under a fast flow of dry O_2 is significant for avoiding the migration of Pt cation from the MFI micropores during the pretreatment process. This procedure ensures the removal of ammonia from the acid sites of H-MFI and converting Pt precursors into Pt^{2+} ions coordinated to the zeolitic framework. TEM images reveal that impregnation for H-MFI-120 and H-MFI-430 lead to a relative broad Pt distribution (**Figure A2.2** in **Appendix**) on the external surface of them, ranging from 1.5 to 2.0 nm, occasionally, some spots are found representing large Pt clusters. However, as STEM images reveal (**Figure A2.3–A2.6** in **Appendix**), there is a majority of Pt particles locating in the voids of zeolites, which could provide an excellent opportunity for the interaction between Pt and acid sites. As for the other two ion-

exchanged samples, Pt/HMFI-24 and Pt/HMFI-40 (**Figure 2.3**), the Pt clusters distribute more uniformly and more small-size particles were observed, which is in agreement with the high Pt dispersion determined by H_2-chemisorption results. Representative TEM and STEM images of Pt/HMFI-24 show rather narrow Pt-distribution with the mean particle size of 1.1 nm **(Table 2.4)**. Even though the maximum diameter of a sphere that can diffuse along MFI framework is 0.45 nm, the careful preparation and activation process for the ion-exchanged sample allow to produce sub-nanosized Pt particles, which are mainly encapsulated inside the zeolite micropores after reduction by H_2.

Table 2.4. Physical and chemical properties of Pt/MFI samples.

Catalyst	Si/Al [a]	Pt [a]	Pt size [b]	Dispersion [c]	Pt size [c]
	atom/atom	wt %	nm	%	nm
Pt/HMFI-24	24	0.99	1.1	99.8	1.1
Pt/HMFI-40	40	0.93	1.2	98.3	1.1
Pt/HMFI-120	116	0.95	2.1	50.2	2.0
Pt/HMFI-430	425	1.01	1.9	63.5	1.6
Pt/Silicalite-1	∞	1.00	1.0	100	1.0

[a]Element composition determined with AAS.

[b]Particle size measured by TEM.

[c]Pt dispersion and particles determined by H_2 chemisorption.

Figure 2.4. EXAFS k^2-weighted $\chi(k)$ plots of the studied catalyst samples measured a) in air at 298 K and b) in H_2 at 473 K are shown. The color-coding is reported in the legend.

Figures 2.4 and **2.5** below show the k^2-weighted $\chi(k)$ and Img[$\tilde{\chi}(R)$] plots of the studied catalyst samples measured a) in air at 298 and b) in H_2 at 473 K, respectively. It was noted that both the oscillations observed in **Figure 2.4** as well as the presence of Pt-structure at

R = 8 shown in **Figure 2.5** indicate that the studied supported Pt catalysts most likely have a distribution of particle sizes, which is also supported by the acquired TEM images shown in **Figure 2.3**.
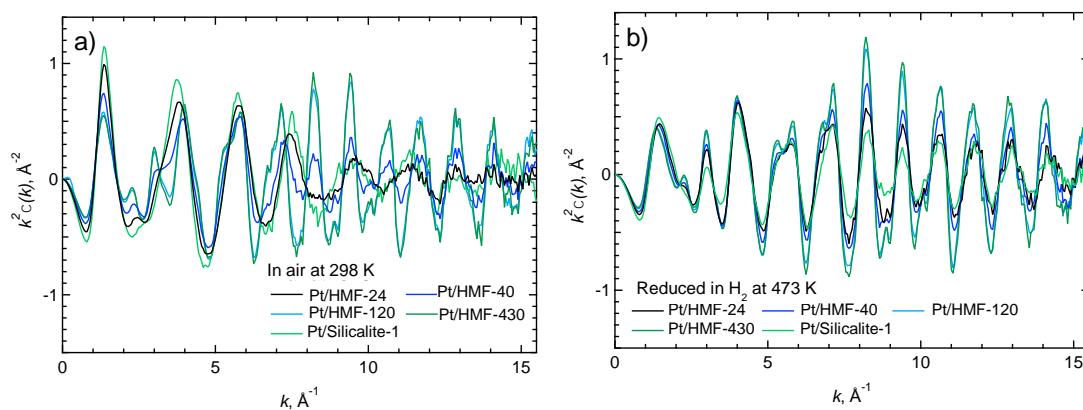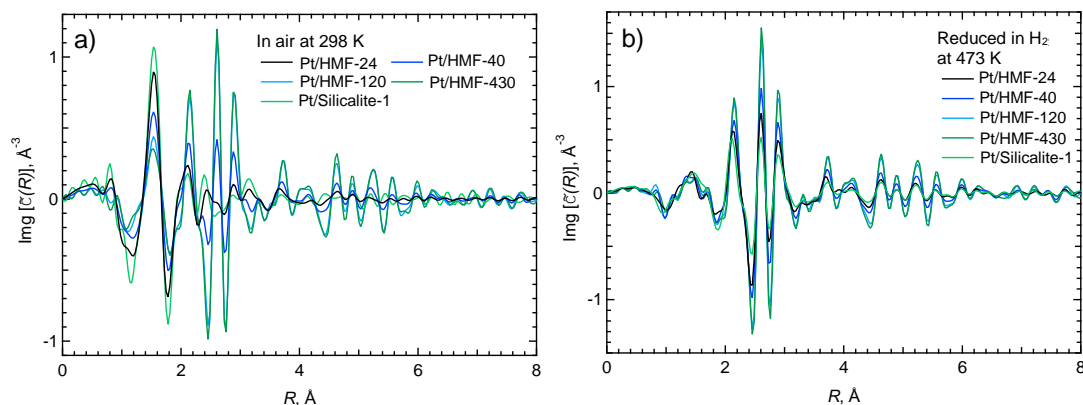

Figure 2.5. EXAFS k^2-weighted Img[$\tilde{\chi}$(R)] of the studied catalyst samples measured a) in air at 298 K and b) in H$_2$ at 473 K are shown. The color-coding is report in the legend.

Table 2.5. The characteristics of the studied supported Pt catalysts as determined by EXAFS analysis. The "Large" particles were defined as > 3 nm, and the "Small" particles were defined as < 3 nm in diameter. The fractions of each type of particles present in the samples were also reported.

Sample [a]	"Large" particles [c]		"Small" particles				
	Pt-atoms (fraction)	Pt-surface atoms (%)[b]	Pt-atoms (fraction)	Pt–Pt (Å)	Pt–Pt DWF[b]	CN Pt–Pt[b]	Pt-surface atoms (%)[b]
Pt-foil	N/A	N/A	N/A	N/A	N/A	N/A	N/A
Pt/HMFI-24	0.130	0.7	0.870	2.749	0.0102 (0.0007)	**8.44** (0.75)	55.7
Pt/HMFI-40	0.267	1.3	0.733	2.747	0.0104 (0.0008)	**8.57** (0.83)	44.0
Pt/HMFI-120	0.487	2.4	0.513	2.759	0.0108 (0.0012)	**9.53** (1.41)	23.6
Pt/HMFI-430	0.537	2.7	0.463	2.761	0.0093 (0.0009)	**9.62** (1.23)	19.9
Pt/Silicalite-1	0.107	0.5	0.893	2.745	0.0120 (0.0012)	**7.26** (0.91)	66.1

[a] The values for the supported Pt catalysts were reported in the reduced state. The measurement was performed at 473 K in 50 bar H$_2$;
[b] The uncertainty was reported in brackets;
[c] Set to values of the Pt-foil reference by definition (first shell Pt CN = 12, the Pt-Pt first shell bond distance was 2.766 Å, and the DWF was 0.00508 (0.0002);
[d] Assuming spherical Pt particles and 5% surface-Pt for the large particles based on the surface/bulk ratio of a sphere as determined from Equation 2.2.

Because EXAFS spectroscopic measurements treated the samples as a whole (bulk), the analysis typically allowed reporting average particle sizes based on parameters such as the Pt coordination number (CN). However, in terms of the Pt/MFI catalysts prepared in this chapter, the specific surface area of the Pt-particles and the number of surface atoms may affect the catalytic activities. Hence, I have attempted to separate the contributions of the "Small" and "Large" Pt nanoparticles by defining the "Small" particles as those having a diameter of less than 3 nm and "Large" particles having a diameter of more than 3 nm. While this definition may be viewed as a qualitative guess at first, the selected size of 3 nm corresponds to a nanoparticle with a coordination number for the first-shell Pt of ~ 9.5, as explained in detail by Frenkel *et al.* in the past.[25] The TEM images (**Figure A2.1**) indicated that there was a large fraction of Pt-particles that range in size from $1 - 3$ nm thus further justifying the selected ranges. Subsequent EXAFS analysis was performed based on the above-mentioned particle gradation by size. The EXAFS fit results including the determined first shell Pt distances, coordination numbers as well as Debye-Waller Factors (DWFs) are reported in **Table 2.5**. While the specific details of the EXAFS analysis were reported in the experimental section, spherical Pt nanoparticles were assumed in which the number of surface metal atoms was determined using Equation 2.2. In Equation 2.2, D refers to the particle diameter in nm and the surface-Pt was assumed to be a monolayer with a Pt shell thickness equal to the Pt-Pt distance determined from EXAFS fitting.

$$\%_{surface-Pt} = \frac{\left(\frac{D}{2}\right)^3 - \left(\frac{D}{2} - 0.276\right)^3}{\left(\frac{D}{2}\right)^3} \cdot 100\ \% \qquad (Eq.2.2)$$

While the fraction of "Large" Pt particles (> 3 nm) range between approximately 0.1 and 0.5 from sample to sample, which contain only less than 2.4 % of total surface Pt. Thus the relative contribution of hydrogen adsorption and subsequent activation by these particles can be negligible in comparison with the "Small" Pt particles (< 3nm). As seen in **Table 2.5**, these "Small" Pt nanoparticles account for the majority of the available surface Pt-species with as much as 66 % of total Pt. The latter particles also typically have an average Pt coordination number between ~ 7.5 and 8.5 with an average uncertainty of ~ 1. The values indicate that the studied catalysts on average contain at least half of the total Pt-species with particle size of $12 - 20$ Å, which is in agreement with the results determined by TEM imaging. Eventually, the average Pt-Pt atom distances of the "Small" particles

compared to the Pt-foil (bulk Pt) decreased slightly with the decreasing of first shell Pt coordination number, which implies the typical nano-particles as reported for Pd particle previously.[24]

2.3.2. Interaction between Pt cluster and BAS of support

The normalized Pt L_{III} edge XANES spectra of the parent and reduced Pt-catalysts as well as Pt-foil and PtO_2 references are shown in **Figure 2.6**. The observed resonance peak in the XANES measured at the Pt L_{III} edge corresponds to the allow $2p_{3/2}$ to the $5d_{5/2}$ bound to bound state transition, which result from the vacancy in the Pt 5d electron level.[26] The plots in **Figure 2.6** include the inserts of the respective white-line peak features for each sample, in which the Pt-XANES spectra exhibit $1 - 2$ eV shifts that appear to be sample-specific.
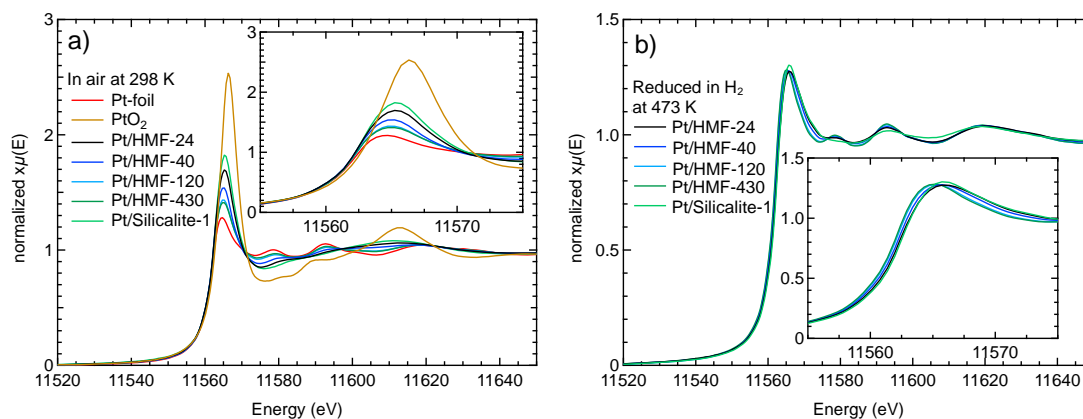

Figure 2.6. Pt L_{III} edge XANES spectra of the studied catalysts at a) 298 K in air and b) 473 K in H_2 are shown. The Pt-foil and PtO_2 reference compounds are also shown.

With the exception of the Pt/Silicalite-1 sample, the fraction of metallic Pt generally increases with decreasing concentration of Al in the zeolite support. This observation indicates that the formation of Pt-clusters is likely kinetically controlled during synthesis because increased Al concentrations in the zeolite allowed a higher degree of Pt incorporation during ion-exchange. The latter lead to the formation of a large concentration of small, highly-dispersed Pt-particles. Pt clusters on Silicalite-1 also show small size, which could results from the much higher percentage of mesopore surface area and volume, compared with other HMFI samples. The higher mesopore surface area and volume

provide more space for confining Pt particles and preventing them from getting aggregations. In the case of the reduced catalysts (**Figure 2.6b**), the shift in the XANES is attributed to the formation of Pt-hydride surface species. [27] Thus, the amount of adsorbed hydrogen is expected to correlate with particle surface-Pt concentrations and should thus be an indicator of the concentration of active sites for hydrogenation reactions.

According to IR spectra of adsorbed CO over Pt/MFI samples, the IR bands of adsorbed CO shifts to higher wavenumbers and the integrated intensity ratio of linear to bridged bonded CO (L/B ratio) increase with the increasing BAS concentrations of supports **(Figure 2.7)**. Both effects suggest a decrease in the electron density of the supported Pt particles, indicating the interaction between Pt clusters and BAS in the micropores of MFI zeolites.
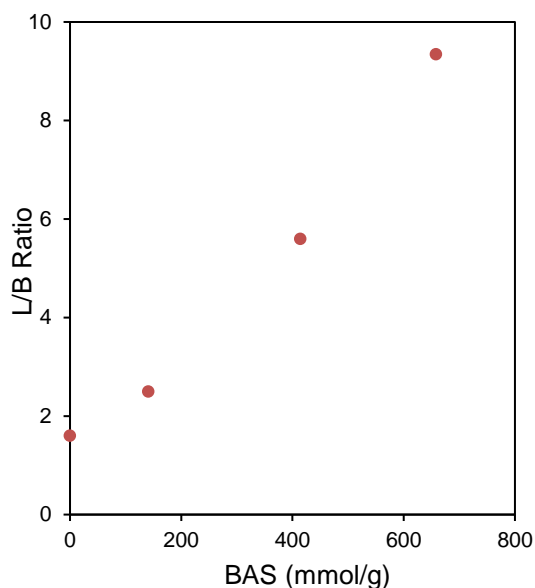
Figure 2.7. Integrated intensity ratio of linear to bridged Pt carbonyls as a function of the support BAS concentration.

The H/D exchange reaction between H_2 and D-form samples was measured by IR spectra. The highest exchanged rate (220 ± 50 $\mu mol \cdot g^{-1} \cdot min^{-1}$) was observed over Pt/DMFI-24 which consisted of sub-nanosized Pt clusters in the micropores of D-MFI-24. The fast exchange of Z-OD to Z-OH (Z-OH refers to hydroxyl group from zeolite BAS) by H_2 indicates the dissociative adsorption H_2 on the Pt surface. Then the active H atom transfer to replace the surrounding D atom from D-form BAS. However, the exchange reaction

hardly occurs on only zeolite without the presence of Pt, as the rate is 0.6 ± 0.3 $\mu mol \cdot g^{-1} \cdot min^{-1}$. Furthermore, the mixture of Pt/Silicalite-1 and D-MFI-24 did not improve the rate of this exchange reaction ($0.8 \pm 0.4 \mu mol \cdot g^{-1} \cdot min^{-1}$). It suggests the short distance is necessary for the interaction between Pt clusters and BAS. Consequentially, the exchange reaction process on Pt/HMFI-24 involves the dissociative adsorption of H_2 on the Pt clusters, followed by exchanging with OD of the zeolite. Afterward, the H/D exchange moves on the whole Pt/MFI catalyst, given the trace amount of water in the system would break OD bond and accelerate the exchange reaction.[28] The detailed kinetic studies show a 0.5^{th} reaction order with respect to H_2, which suggests the dissociative adsorption of H_2 on the Pt clusters. The activation enthalpy of the exchange reaction was estimated to be 16 $kJ \cdot mol^{-1}$ by performing the reactions at $303 - 333$ K. The details of the calculation were supplemented in appendix **Figure A2.7** – **A2.10**.
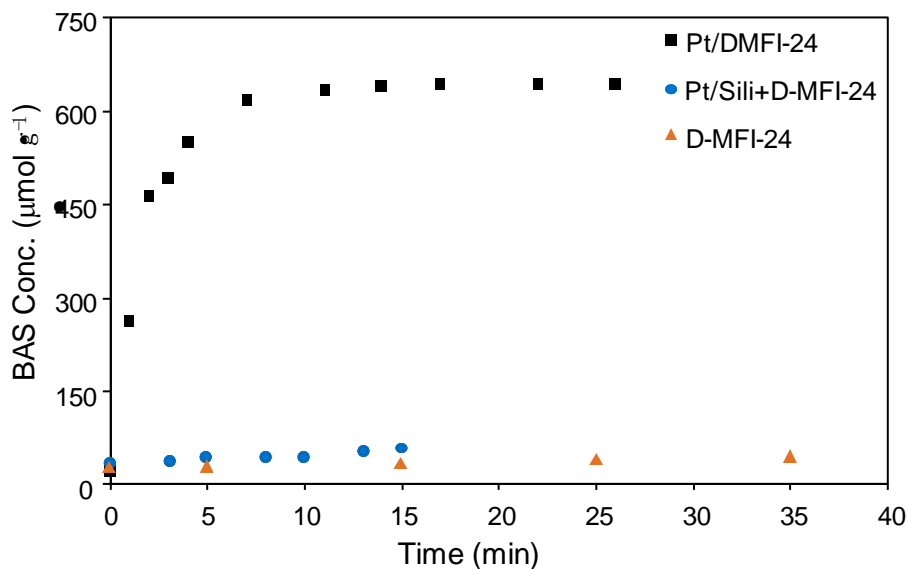
Figure 2.8. H/D exchange reaction between H_2 and D-form samples by the IR measurement under 1 mbar of H_2 at 423 K.

2.4. Conclusions

A series of Pt/MFI catalysts composed of the sub-nanosized Pt cluster encapsulated in MFI zeolite with varying BAS concentration were prepared and characterized in this chapter. All the physical and chemical properties of these samples were comparable, except different BAS concentrations of the MFI support. STEM images showed that Pt clusters ($\leq$

2 nm) were well-distributed and encapsulated in the voids of MFI zeolites for all the catalysts. Both of XANES and the IR spectra of CO adsorption revealed a change of electronic state for Pt clusters. The H/D exchange reaction between H_2 and D-form zeolite suggested the dissociative adsorption of H_2 on Pt surface and the interaction of Pt clusters with proximal BAS.

2.5. Appendix
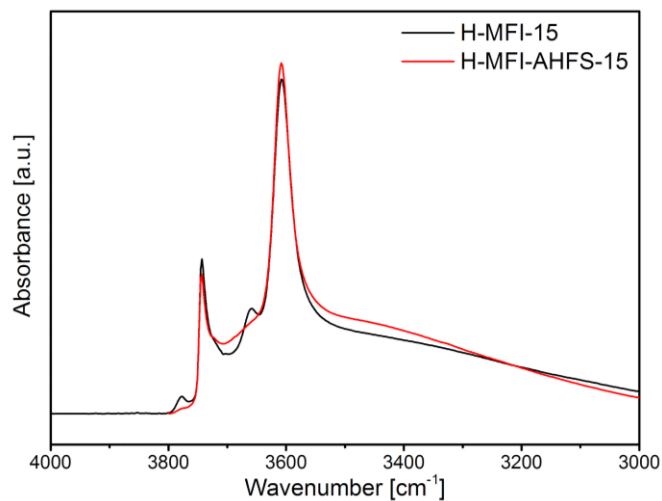
Figure A2.1. IR spectra of H-MFI-15 sample before (in black) and after (in red) AHFS treatment.
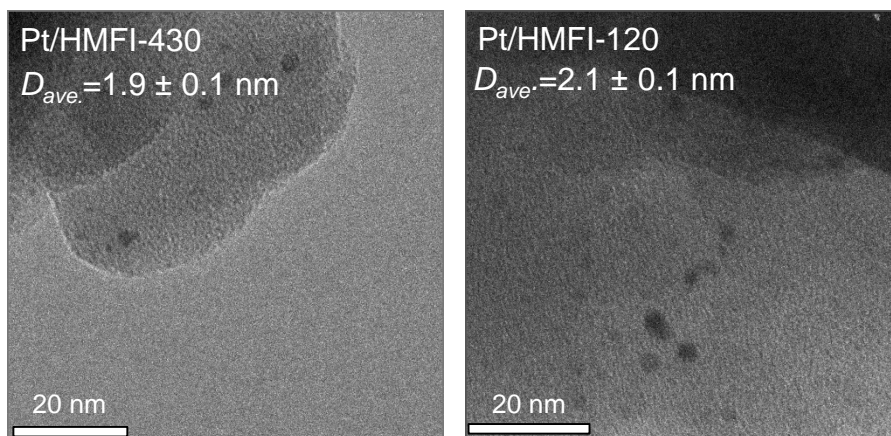
Figure A2.2. TEM images of Pt/HMFI-430 and Pt/HMFI-120.
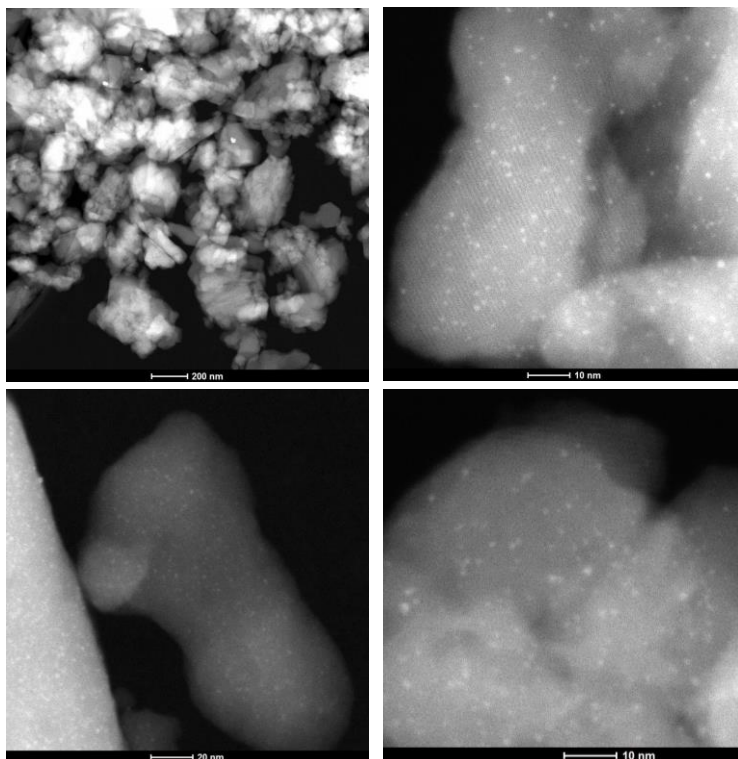
Figure A2.3. STEM images of Pt/HMFI-24.
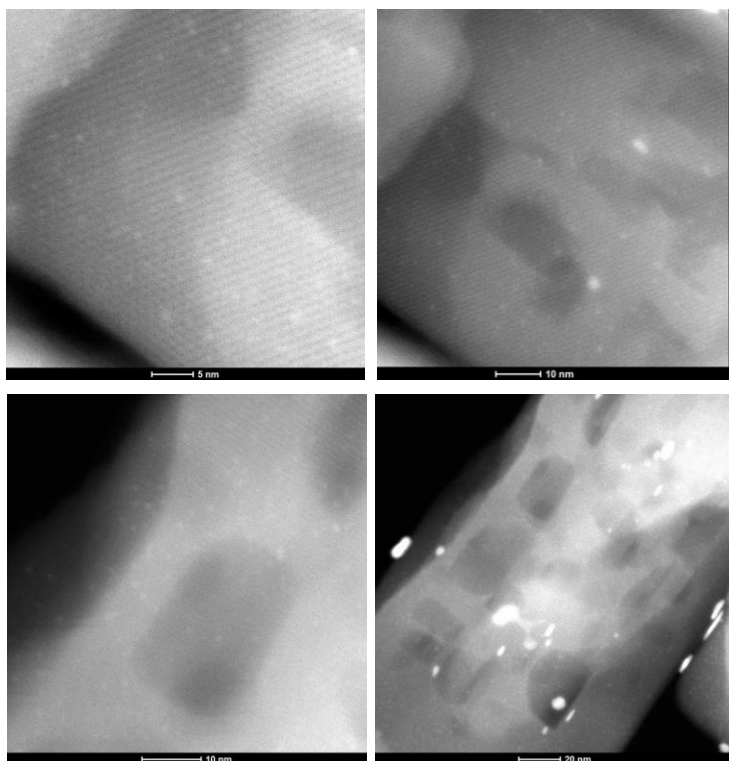
Figure A2.4. STEM images of Pt/HMFI-40.
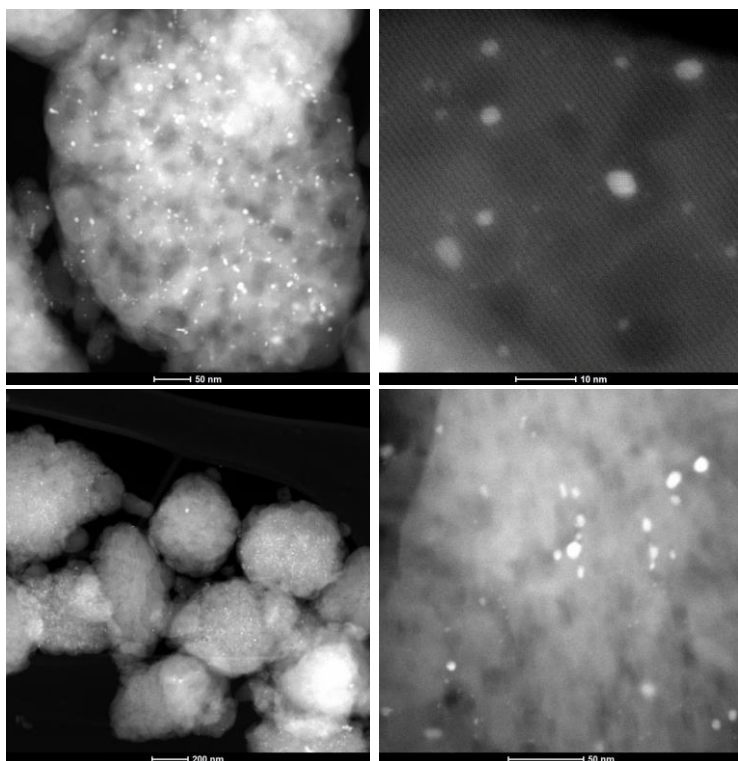
Figure A2.5. STEM images of Pt/HMFI-120.
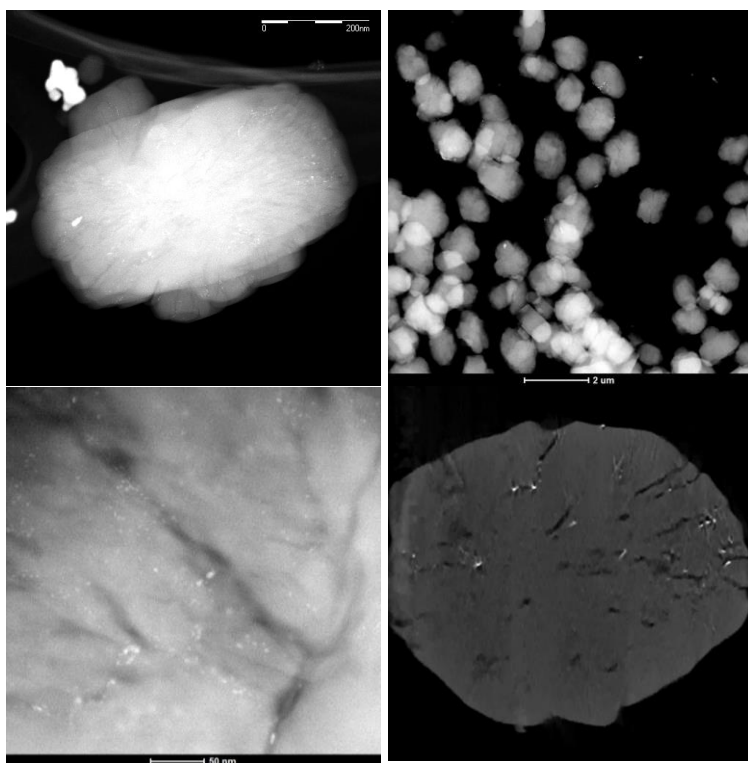
Figure A2.6. STEM images of Pt/HMFI-430.
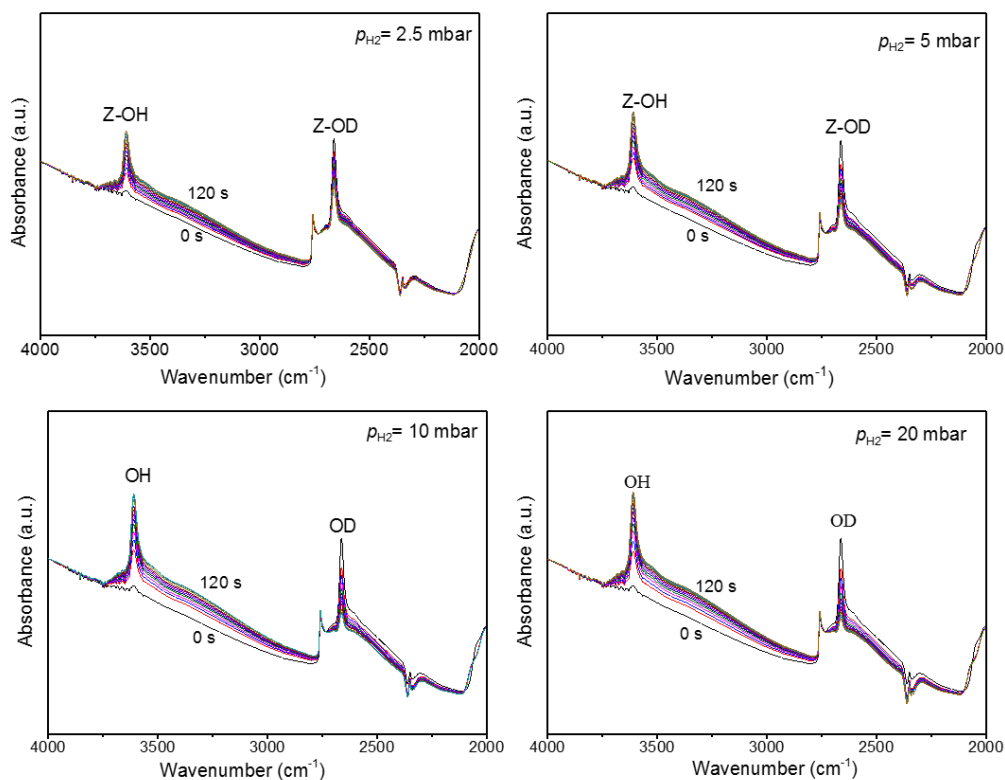
Figure A2.7. IR spectra of H/D exchange reactions under 2.5, 5, 10 and 20 mbar of H_2 pressure at 323 K.
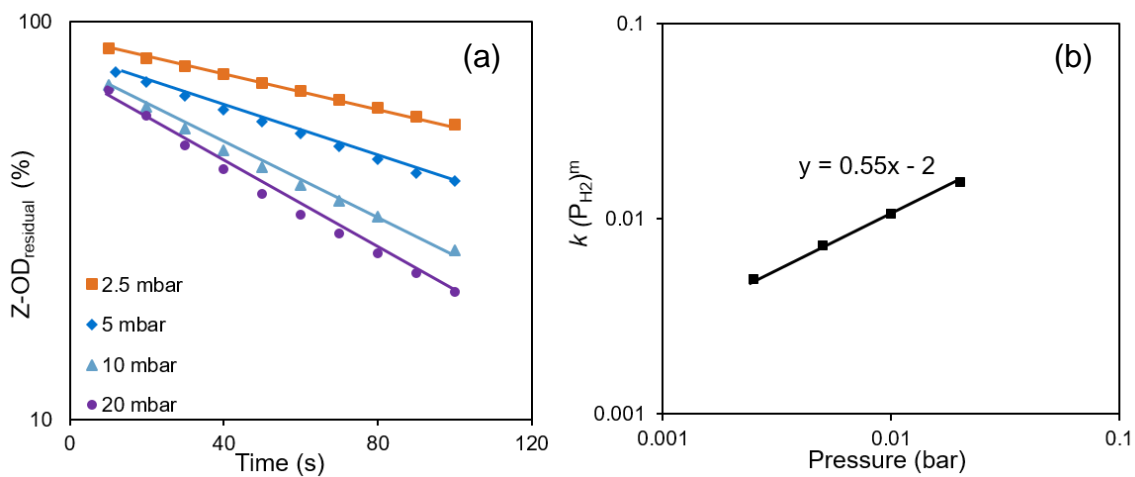
Figure A2.8. H/D exchange reaction under 2.5, 5, 10 and 20 mbar of H_2 pressure at 323 K; (a) Proportionality of Z-OD (D-form BAS) to reaction time; (b) The reaction order (0.5) with respect to the pressure of H_2. (Rate $= -d[Z\text{-}OD]/dt = k\cdot[Z\text{-}OD]^n \cdot p_{H_2}^m$)
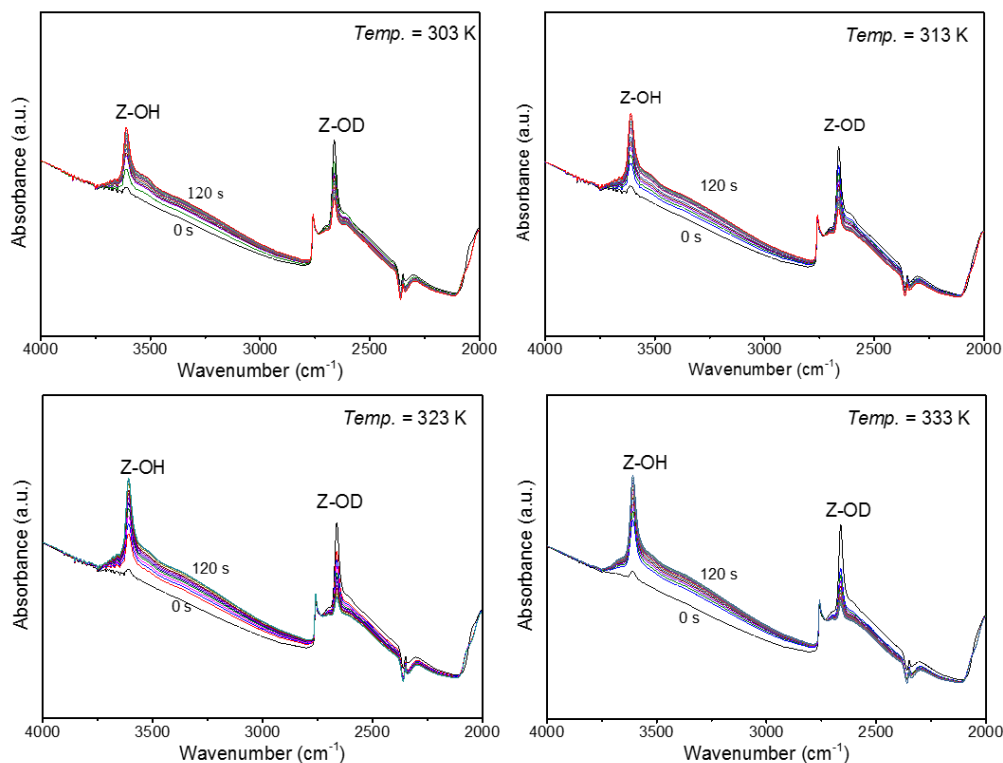
Figure A2.9. IR spectra of H/D exchange reactions at 303 — 333 K under 10 mbar of H_2 pressure.
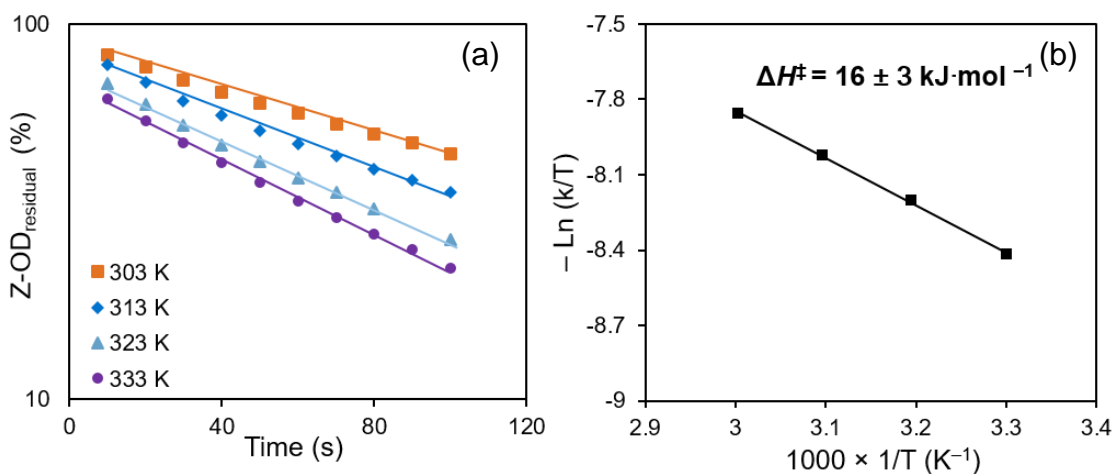
Figure A2.10. H/D exchange reactions at 303 — 333 K under 10 mbar H_2. (a) Proportionality of residual Z-OD (D-form BAS) percentage to reaction time.at 303 — 333 K. (b) Eyring plot (ln(k/T) – 1000×(1/T)) to determine the enthalpy required ($\Delta H^{\ddagger}$) to reach the transition state complex.

2.6. Associate content

Publication

This chapter in combination with Chapter 4 is to be submitted for publication.

Contributions

The work in this chapter was under the supervision of Dr. Yue Liu and Dr. Eszter Baráth. Guoju Yang contributed to the design of the experiments and operating setups and data analysis. Dr. Aleksei Vjunov contributed with the design of XAS experiments and related data analysis. Johannes A. Lercher was responsible for data discussion, supervising. Dr. Yue Liu and Prof. Dr. Johannes A. Lercher are the principal investigators of this work.

2.7. Reference

[1] S.i. Matsumoto, *Catal. Today,* 90 (**2004**) 183-190.

[2] D.E. Webster, *Top. Catal.,* 16 (**2001**) 33-38.

[3] R. Wang, Y. Li, R. Shi, *et al.*, *J. Mol. Catal. A: Chem.,* 344 (**2011**) 122-127.

[4] J. Lif, I. Odenbrand, M. Skoglundh, *Applied Catalysis A: General,* 317 (**2007**) 62-69.

[5] T. Visser, T.A. Nijhuis, A.M.J. van der Eerden, *et al.*, *J. Phys. Chem. B,* 109 (**2005**) 3822-3831.

[6] P. Salagre, J.L.G. Fierro, F. Medina, et al., *J. Mol. Catal. A: Chem.,* 106 (**1996**) 125-134.

[7] V.L. Barrio, P.L. Arias, J.F. Cambra, *et al.*, *Applied Catalysis A: General,* 248 (**2003**) 211-225.

[8] M. Rivallan, E. Seguin, S. Thomas, *et al.*, *Angew. Chem. Int. Ed.,* 49 (**2010**) 785-789.

[9] S. Altwasser, R. Gläser, J. Weitkamp, *Microporous Mesoporous Mater.,* 104 (**2007**) 281-288.

[10] S. Goel, S.I. Zones, E. Iglesia, *J. Am. Chem. Soc.,* 136 (**2014**) 15280-15290.

[11] H. Yang, H. Chen, J. Chen, *et al.*, *J. Catal.,* 243 (**2006**) 36-42.

[12] B.Z. Zhan, E. Iglesia, *Angew. Chem. Int. Ed.,* 46 (**2007**) 3697-3700.

[13] S. Goel, Z.J. Wu, S.I. Zones, *et al.*, *J. Am. Chem. Soc.,* 134 (**2012**) 17688-17695.

[14] A. Philippaerts, S. Paulussen, S. Turner, *et al.*, *J. Catal.,* 270 (**2010**) 172-184.

[15] W. Luo, U. Deka, A.M. Beale, *et al.*, *J. Catal.,* 301 (**2013**) 175-186.

[16] S. Schallmoser, T. Ikuno, M.F. Wagenhofer, *et al.*, *J. Catal.,* 316 (**2014**) 93-102.

[17] J.C. Di, H.Y. Chen, X.F. Wang, *et al.*, *Chem. Mater.,* 20 (**2008**) 3543-3545.

[18] W.D. Harkins, *Science,* 102 (**1945**) 263-268.

[19] M. Newville, *Journal of synchrotron radiation,* 8 (**2001**) 322-324.

[20] J.J. Rehr, J.J. Kas, F.D. Vila, *et al.*, *PCCP,* 12 (**2010**) 5503-5513.

[21] B. Ravel, M. Newville, *Journal of synchrotron radiation,* 12 (**2005**) 537-541.

[22] O. Muller, R. Roy, *Journal of the Less Common Metals,* 16 (**1968**) 129-146.

[23] R.W.G. Wyckoff, *American Mineralogist Crystal Structure Database,* (**1963**).

[24] Z.A. Chase, J.L. Fulton, D.M. Camaioni, *et al.*, *The Journal of Physical Chemistry C,* 117 (**2013**) 17603-17612.

[25] A.I. Frenkel, C.W. Hills, R.G. Nuzzo, *J. Phys. Chem. B.*, 105 (**2001**) 12689-12703.

[26] S. Mukerjee, S. Srinivasan, M.P. Soriaga, *et al.*, *J. Phys. Chem.,* 99 (**1995**) 4577-4589.

[27] A. Gorczyca, V. Moizan, C. Chizallet, *et al.*, *Angew. Chem. Int. Ed.,* 53 (**2014**) 12426-12429.

[28] R. Prins, *Chem. Rev.,* 112 (**2012**) 2714-2738.

Chapter 3

Determination of H_2 adsorption heat on Pt/MFI catalysts in the aqueous phase

A kinetic method was developed for determining the adsorption kinetics and thermodynamics of H_2 on transition metals in water. Using the reaction of gas H_2 with liquid D_2O into liquid HDO, gas HD and D_2 catalyzed by a transition metal, a correlation among the reaction rate, H_2 pressure and H_2 adsorption constant was established. By measuring the HD and D_2 formation rates as well as their variation with pressure and temperature, the H_2 adsorption constant and adsorption heat were determined. Applying this method to Pt/MFI catalysts, H_2 adsorption heats were obtained as (50 ± 3) $kJ \cdot mol^{-1}$ on Pt/Silicalite-1 and (41 ± 3) $kJ \cdot mol^{-1}$ on Pt/HMFI-24 (Si/Al = 24). It was found that H_2 adsorption on Pt in water is much weaker than that in the gas phase and an acidic environment provided by the support further weakens the adsorption.

3.1. Introduction

Activation of H_2 is the basic step required in catalytic hydrogenation and hydrogenolysis [1, 2], and in hydrogen fuel cell anode reactions. [3, 4] Transition metals are widely used a catalysts for H_2 activation.[5, 6] The H_2 activation on a transition metal surface involves physisorption of H_2, cleavage of H–H bond and formation of H-metal bond on the surface, which is known as dissociative adsorption.[7] The adsorbed surface H makes new bonds, e.g. C–H, O–H, with other adsorbed substrates in hydrogenation or hydrogenolysis, or donates electrons on a fuel cell anode to generate current.

The capability of material to adsorb and activate H_2 is normally evaluated by its adsorption heat. The adsorption heat of H_2 on transition metal has been experimentally and theoretically well studied and documented (summarized in **Table 3.1**).[8-22] Most of these studies were on gas phase adsorption, meaning that transition metals were directly exposed to the H_2 gas. Plenty of hydrogenation and hydrogenolysis reactions proceed in the aqueous phase or in the presence of a large amount of water, such as hydrotreating of biomass derivatives[1, 6, 23], electrohydrogenation in an electrolyte solution[4] and enzymatic hydrogenation by hydrogenases[24, 25]. Study of these processes requires understanding H_2 adsorption on the catalyst that is immersed in water.

Table 3.1. Reported adsorption heat of H_2 on the Pt surface.

ΔH_{ads} (kJ·mol^{-1})	Method	Refs.
63 –106	Field emission, Pt crystal	[8, 26]
44 –103	modified calorimeter, Pt wire，Pt/SiO₂，Pt powder	[9, 10]
80 – 92	He beam diffraction, Pt(111) surface	[11]
56 – 71	Differential scanning calorimeter, supported Pt or Pt powder	[12, 27, 28]
90 – 95	Heat-flow microcalorimetry, Pt/SiO₂, Pt powder	[13, 14]
60 – 120	Micromeritics ASAP 2010 apparatus, Pt/SiO₂ , Pt/Al₂O₃	[15]
61 – 125	differential scanning calorimeter, Pd/SiO₂ , Pd/Al₂O₃	[13, 29, 30]
88 – 102	LEED, thermal desorption spectroscopy and contact potential measurements, Pd crystal surface	[31]
85 – 122	TPD, Ni/SiO₂ , Ni/Al₂O₃	[32]
44 – 82	Theoretical calculation, on Pt crystal surface	[16-18, 33-36]
48 – 178	Theoretical calculation, on Pt clusters	[18-22]

Currently, only through electrochemical methods can the adsorption heat of H_2 on materials in water be determined. In cyclic voltammetry (CV) measurement of a metal electrode in electrolyte solutions, an adsorption peak in the CV curve was characteristic for under-potential adsorbed H (H_{upd}) in the cathodic H_2 evolution reaction. A hydrogen binding energy (HBE), which is virtually the H_2 adsorption heat on the cathode material per mole H atom,[37-39] can be calculated based on the potential of this peak (E_{peak}) via multiplying the Faraday constant (HBE $= F \cdot E_{peak}$).[37] This method requires i) the measuring materials to be electrically conductive; ii) either they themselves to be an electrode or immobilizable on another electrodes; iii) sufficient electrolyte concentrations in water. These requirements limit its application to only a small number of materials. Many hydrogenations and hydrogenolysis catalysts cannot be measured by this method, as those using oxide supports (e.g. Ni/Al_2O_3, Cu/SiO_2) which are non-conductive and using zeolite supports (e.g. Pt/HMFI) which exchange cations with electrolytes in the solution.

In this chapter, I established a novel kinetic method to determine the adsorption heat of H_2 onto Pt/MFI catalysts immersed in water, which can be applied for other transition metal catalysts as well. It is based on reactions of gas H_2 with liquid D_2O into gas D_2, HD and liquid HDO over a certain catalyst, as shown in Equation 3.1 and 3.2 below. By measuring the formation rates of D_2 and HD and particularly their variation with H_2 pressure and temperature, I obtain the activation energy of H_2 adsorption and desorption as well as the adsorption heat on the catalysts.

$$H_2 \text{ (g)} + 2D_2O \text{ (l)} \xrightarrow{\text{Catalyst}} D_2 \text{ (g)} + 2HDO \text{ (l)} \qquad (3.1)$$

$$H_2 \text{ (g)} + D_2O \text{ (l)} \xrightarrow{\text{Catalyst}} HD \text{ (g)} + HDO \text{ (l)} \qquad (3.2)$$
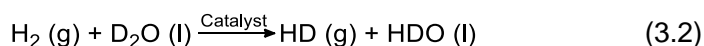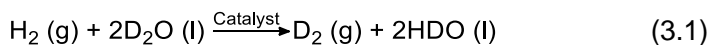
3.2. Experimental and theoretical methods

3.2.1. Preparation and characterization of catalytic materials

To investigate the influence of H_2 adsorption on phenol hydrogenation over Pt/MFI catalysts. The Pt/Silicalite-1 and Pt/HMFI-24 (Si/Al = 24) were chosen as representative samples in this chapter. The preparation method and characterization measurements of two samples have been described in Chapter 2 (Part 2.2. Experimental).

3.2.2. Reactions of gas H₂ with liquid D₂O

The reactions of gas H_2 with liquid D_2O over Pt/Silicalite-1 and Pt/HMFI-24 were carried out in an autoclave (Parr Instrument, 100 mL). Typically, 0.02 g Pt/Silicalite-1 or Pt/HMFI-24 and 30 ml D_2O was added into the autoclave reactor. Under 700 rpm agitation, the reactor was heated to the required temperature. When the temperature was reached, the reactor was quickly purged with H_2 for 3 times and pressurized under a certain pressure of H_2. After a certain reaction time, the gas was collected by a gas bag, and its component was analyzed by a mass-spectroscopy. The apparent reaction rate and rate normalized to surface Pt atoms are:

Apparent rate = Product yield / Reaction time

Rate per surface Pt = Apparent rate / Number of surface Pt loaded in reaction

3.3. Results and discussion

3.3.1. Physicochemical properties of catalysts.

Table 3.2. Physicochemical properties of Pt/HMFI-24 and Pt/Silicalite-1 catalysts.

Description	Catalysts	
	Pt/HMFI-24	Pt/Silicalite-1
Si/Al (atom/atom)[a]	24	∞
Pt loading (wt. %) [a]	0.99	1
Pt dispersion (%)[b]	97	100
Pt size (nm)[c]	1.1	1.0
BAS ($\mu mol.g^{-1}$)[d]	658	0
LAS ($\mu mol.g^{-1}$)[d]	54	0

[a] Element composition determined with AAS.

[b] Pt dispersion Determined by H₂ chemisorption.

[c] Particle size measured by TEM.

[d] The acidic properties probed by IR spectra of adsorbed pyridine (Py-IR).

The main physicochemical properties of Pt/HMFI-24 and Pt/Silicalite-1 have been shown in details in Chapter 2 (in 2.3.1). Here they are also compiled in **Table 3.2**. The H-MFI-24 (Si/Al = 24) is an acidic support with 658 $\mu mol·g^{-1}$ BAS concentration and 54 $\mu mol·g^{-1}$ LAS concentration, while Silicalite-1 is non-acidic. The particle sizes of Pt are comparable for both materials, 1.0 nm for Pt/Silicalite-1 and 1.1 nm for Pt/HMFI-24. Other physical and chemical properties are summarized in **Table 3.2**.

3.3.2. Calculation of kinetic isotope effect

It is known when an atom in a reactant molecule is replaced by one of its isotopes, rate constants for the reaction may change. The ratio between them is the kinetic isotope effect (KIE). This effect is normally weak for heavy atom isotopes, but is substantial for hydrogen isotopes (H, D and T). In the reaction of gas H_2 with liquid D_2O over Pt catalysts, the kinetic isotope effect in the formation rates of H_2, HD and D_2 involves the three elementary reactions in **Table 3.3**. The kinetic isotope effect $[KIE]_{HD}$ and $[KIE]_{D_2}$ are defined as their constant rate ratios,

$$[KIE]_{HD} = \frac{k_{HD}}{k_{H_2}}; \ [KIE]_{D_2} = \frac{k_{D_2}}{k_{H_2}}$$

In order to calculate the $[KIE]_{HD}$ and $[KIE]_{D_2}$ for HD and D_2, Bigeleisen's theoretical treatments were applied.[40] The the expression for calculating hydrogen/deuterium kinetic isotope effect was simplified as shown in the following Equation 3.3:

$$\frac{k_H}{k_D} = S \cdot M \cdot I \cdot EXC \cdot ZPE \quad (3.3)$$

Table 3.3. Derivation of kinetic isotope effect (KIE) for the desorption of HD and D_2 on Pt.

Description	Reaction steps	Rate constant	molecular mass	moment of inertia	Zero point energy
H₂ desorption	Pt-H + Pt-H $\xrightarrow{k_{H_2}}$ 2Pt + H₂	k_{H_2}[a]	M_{H_2}	I_{H_2}	ZPE_{PtH}; ZPE_{PtD}
HD desorption	Pt-H + Pt-D $\xrightarrow{k_{HD}}$ 2Pt + HD	k_{HD}	M_{HD}	I_{HD}	ZPE_{H_2}
D₂ desorption	Pt-D + Pt-D $\xrightarrow{k_{D_2}}$ 2Pt + D₂	k_{D_2}	M_{D_2}	I_{D_2}	ZPE_{HD}; ZPE_{D_2}
Derivation of Kinetic isotope effects	$[KIE]_{HD} = \dfrac{k_{HD}}{k_{H_2}} = \left(\dfrac{M^{\ddagger}_{HD}}{M^{\ddagger}_{H_2}}\right)^{\frac{3}{2}} \left(\dfrac{(I^{\ddagger}_{HD})^2}{(I^{\ddagger}_{H_2})^2}\right)^{\frac{1}{2}} \exp\left(\dfrac{(ZPE_{H_2} - ZPE_{HD}) - (ZPE_{PtH} - ZPE_{PtD})}{RT}\right)$ (Eq. 3.4)				
	$[KIE]_{D_2} = \dfrac{k_{D_2}}{k_{H_2}} = \left(\dfrac{M^{\ddagger}_{D_2}}{M^{\ddagger}_{H_2}}\right)^{\frac{3}{2}} \left(\dfrac{(I^{\ddagger}_{D_2})^2}{(I^{\ddagger}_{H_2})^2}\right)^{\frac{1}{2}} \exp\left(\dfrac{(ZPE_{H_2} - ZPE_{D_2}) - 2(ZPE_{PtH} - ZPE_{PtD})}{RT}\right)$ (Eq. 3.5)				

H or D in the subscript refers to hydrogen or deuterium containing species. Both S factor (symmetry number) and EXC factor (from the contributions of vibrationally excited molecules) were ignorable in this work. Hence only molecular mass (*M* factor), the moment of inertia (*I* factor) and zero point energy (*ZPE*) of the corresponding species were considered. Notably, the late transition state was proposed for desorptions of H_2, HD and

D$_2$ from Pt surface, as the reverse process- adsorption of H$_2$ on Pt surface, is almost energy barrierless.[16, 20, 36] In addition, translational and rotational degrees of freedom for surface H and D species (Pt-H and Pt-D) were neglected. Eventually, the kinetic isotope effects of HD and D$_2$ are expressed as Equation 3.4 and 3.5 in **Table 3.3**. The values of corresponding *M*, *I* and *ZPE* factors involved in the calculation of kinetic isotope effects are listed in **Table 3.4**.

Table 3.4. *M*, *I* and *ZPE* values of H and D-containing species involved in the calculation for the KIE.

Species	*M* (g·mol^{-1})	*I* (×10^{-14}g·cm^{-2})	*ZPE*[a] (kJ·mol^{-1})	Ref.
Pt-H	[d]	[d]	17.4 [b]	[34]
Pt-D	[d]	[d]	12.3 [c]	
H$_2$	2	4.67	26.1	[41]
HD	3	6.21	22.6	
D$_2$	4	9.31	18.5	

[a] ZPE = 0.5$h\upsilon$ (υ is the fundamental vibrational frequency).

[b] Calculated on the basis of vibrations both normal and parallel to the surface.

[c] The vibrational frequency of this mode was estimated from that of Pt−H bond, based on $\frac{v_{Pt-D}}{v_{Pt-H}} = \sqrt{\frac{\mu_{Pt-H}}{\mu_{Pt-D}}}$ (μ refers to the reduced mass).

[d] Translational and rotational degrees of freedom for surface H and D are ignored.

Therefore, [KIE]$_{HD}$ and [KIE]$_{D_2}$ can be calculated using the values in **Table 3.4** , according to Equation 3.4 and 3.5. The values of them vary depending on the temperature, as shown in **Table 3.5**.

Table 3.5. [KIE]$_{HD}$ and [KIE]$_{D_2}$ values at temperatures of 303 – 343 K.

Temp (K)	[KIE]$_{HD}$	[KIE]$_{D_2}$
303	1.29	2.01
313	1.32	2.08
323	1.35	2.14
333	1.37	2.20
343	1.39	2.27

3.3.3. Kinetic derivation and calculation of H₂ adsorption heat

The reaction of gas H_2 with liquid D_2O into liquid HDO, gas HD and D_2 (Eq. 3.1 and 3.2) generally involves three elementary steps: dissociative adsorption of H_2 (Eq. 3.6), surface D generation via the reaction of D_2O with surface H (Eq. 3.7) and desorption of products as D_2, HD and H_2 (Eqs. 3.8 – 3.10). The detailed elementary steps and corresponding kinetic parameters are summarized in **Table 3.6**.

Table 3.6. Elementary steps in the reaction of H_2 with D_2O.

Description	Elementary step		Rate constant	Rate equation	
H_2 adsorption	$H_2 + 2* \xrightarrow{k_a} 2H*$	(3.6)	k_a	$r_{ads} = k_a p_{H_2} \theta_*^2$	(3.11)
$D*$ generation	$H* + D_2O \xrightarrow{k_{exc}} D* + HDO$	(3.7)	k_{exc}	$r_{exc} = k_{exc} \theta_H [D_2O]$	(3.12)
H_2 desorption	$H* + H* \xrightarrow{k_{-a}} H_2 + 2*$	(3.8)	k_{-a}	$r_{H_2} = k_{-a} \theta_H^2$	(3.13)
HD desorption	$H* + D* \xrightarrow{k_{HD}} HD + 2*$	(3.9)	$k_{HD} = k_{-a}[KIE]_{HD}$	$r_{HD} = 2k_{HD} \theta_D \theta_H$	(3.14)
D_2 desorption	$D* + D* \xrightarrow{k_{D_2}} D_2 + 2*$	(3.10)	$k_{D_2} = k_{-a}[KIE]_{D_2}$	$r_{D_2} = k_{D_2} \theta_D^2$	(3.15)

* : Pt sites uncovered by H or D.

p_{H_2}: H_2 pressure.

θ_H and θ_D are the coverage of H and D accessible sites.

θ_* is the fraction (coverage) of Pt sites uncovered by H or D.

k_{-a} refers to the rate constant of H_2 desorption, which is the same with k_{H_2} used in **Table 3.3**.

$[KIE]_{HD}$ is k_{HD}/k_{-a}, the value varies in the range of 1.29 –1.39, depending on the temperatures of 303 – 343 K.

$[KIE]_{D_2}$ is k_{D_2}/k_{-a}, the values vary in the range of 2.01 – 2.27, depending on the temperatures of 303 – 343 K.

$[D_2O]$: the activity of the D_2O in the reaction solution, considered as 1 in pure D_2O.

The number of adsorption sites on Pt surface is a constant that the total coverage of H atom, D atom, and uncovered site equals to 1 (Eq. 3.16).

$$\theta_D + \theta_H + \theta_* = 1 \qquad (3.16)$$

Based on Equation 3.11, 3.13 and 3.15, the coverage of H atom, D atom and the empty site can be individually expressed as:

$$\theta_H = r_{H_2}^{0.5} \cdot k_{-a}^{-0.5} \qquad (3.17)$$

$$\theta_D = r_{D_2}^{0.5} \cdot k_{-a}^{-0.5} \cdot [KIE]_{D_2}^{-0.5} \qquad (3.18)$$

$$\theta_* = r_{\text{ads}}^{0.5} \cdot k_a^{-0.5} \cdot p_{\text{H}_2}^{-0.5} \qquad (3.19)$$

Therefore, Equation 3.16 is reformulated as Equation 3.20.

$$r_{\text{D}_2}^{0.5} \cdot k_{-a}^{-0.5} \cdot [\text{KIE}]_{\text{D}_2}^{-0.5} + r_{\text{H}_2}^{0.5} \cdot k_{-a}^{-0.5} + r_{\text{ads}}^{0.5} \cdot k_a^{-0.5} \cdot p_{\text{H}_2}^{-0.5} = 1 \qquad (3.20)$$

Considering a steady state reaction, in which the adsorption rate of H₂ from gas phase onto Pt equals to the desorption rate of H₂, HD and D₂ from Pt into the gas phase (Eq. 3.21),

$$r_{\text{ads}} = r_{\text{H}_2} + r_{\text{HD}} + r_{\text{D}_2} \qquad (3.21)$$

Equation 3.20 is further written as Equation 3.22 and reformulated as Equation 3.23.

$$r_{\text{D}_2}^{0.5} \cdot k_{-a}^{-0.5} \cdot [\text{KIE}]_{\text{D}_2}^{-0.5} + r_{\text{H}_2}^{0.5} \cdot k_{-a}^{-0.5} + (r_{\text{H}_2} + r_{\text{HD}} + r_{\text{D}_2})^{0.5} \cdot k_a^{-0.5} \cdot p_{\text{H}_2}^{-0.5} = 1 \qquad (3.22)$$

$$(r_{\text{H}_2} + r_{\text{HD}} + r_{\text{D}_2})^{0.5} \cdot p_{\text{H}_2}^{-0.5} = k_a^{0.5} - \left(r_{\text{H}_2}^{0.5} + r_{\text{D}_2}^{0.5} \cdot [\text{KIE}]_{\text{D}_2}^{-0.5} \right) \cdot (k_a / k_{-a})^{0.5} \qquad (3.23)$$

Note that the last term in Equation 3.23, k_a / k_{-a}, is actually the adsorption equilibrium constant of H₂ on Pt, i.e. K_a (Eq. 3.24).

$$K_a = k_a / k_{-a} \qquad (3.24)$$

Thus Equation 3.25 is finally obtained from Equation 3.23 and 3.24.

$$(r_{\text{H}_2} + r_{\text{HD}} + r_{\text{D}_2})^{0.5} \cdot p_{\text{H}_2}^{-0.5} = k_a^{0.5} - \left(r_{\text{H}_2}^{0.5} + r_{\text{D}_2}^{0.5} \cdot [\text{KIE}]_{\text{D}_2}^{-0.5} \right) \cdot K_a^{0.5} \qquad (3.25)$$

The form of Equation 3.25 shows that under certain values of k_a and K_a, which are typically constants under a fixed temperature, the term $(r_{\text{H}_2} + r_{\text{HD}} + r_{\text{D}_2})^{0.5} \cdot p_{\text{H}_2}^{-0.5}$ has a negative linear correlation with the term of $\left(r_{\text{H}_2}^{0.5} + r_{\text{D}_2}^{0.5} \cdot [\text{KIE}]_{\text{D}_2}^{-0.5} \right)$. The slope is the square root of K_a and the intercept is the square root of k_a. The desorption rates of HD (r_{HD}) and D₂ (r_{D_2}) are measurable as the formation rates of HD and D₂ in the reaction. The desorption rate of H₂ (r_{H_2}) is difficult to directly measure because of the large presence of gas H₂, however it can be calculated using the measured r_{HD} and r_{D_2} (Eq. 3.26). According to the rate Equations 3.13, 3.14 and 3.15, r_{H_2} can be expressed as a function of r_{HD} and r_{D_2},

$$r_{\text{H}_2} = \frac{[\text{KIE}]_{\text{D}_2} \cdot r_{\text{HD}}^2}{4[\text{KIE}]_{\text{HD}}^2 \cdot r_{\text{D}_2}} \qquad (3.26).$$

This gives a practical method to determine K_a and k_a from linear fitting Equation 3.25, using the data of r_{HD} and r_{D_2} measured under a series of different pressure of H₂ (p_{H_2})

(**Table 3.7**). Further, all the relevant kinetic and thermodynamic parameters, e.g. adsorption heat and energy barrier, can be obtained via Arrhenius equation and Van't Hoff equation.

Table 3.7. An experimental method to determine the k_a, k_{-a} and K_a via the reaction of H$_2$ with liquid D$_2$O.

Reaction	H_2 (g) + 2D$_2$O (l) $\xrightarrow{\text{Pt}}$ D$_2$ (g) + 2HDO (l)	(Eq. 3.1)
	H_2 (g) + D$_2$O (l) $\xrightarrow{\text{Pt}}$ HD (g) + HDO (l)	(Eq. 3.2)
Equation	$(r_{H_2} + r_{DH} + r_{D_2})^{0.5} \cdot p_{H_2}^{-0.5} = k_a^{0.5} - (r_{H_2}^{0.5} + r_{D_2}^{0.5} \cdot [\text{KIE}]_{D_2}^{-0.5}) \cdot K_a^{0.5}$ (Eq. 3.25)	
Data acquisition	r_{HD} and r_{D_2} measured by HD and D$_2$ formation rate, r_{H_2} calculated by $r_{H_2} = \frac{[\text{KIE}]_{D_2} \cdot r_{HD}^2}{4[\text{KIE}]_{HD}^2 \cdot r_{D_2}}$ (Eq.3.26)	
Plot	Plotting $(r_{H_2} + r_{HD} + r_{D_2})^{0.5} \cdot p_{H_2}^{-0.5}$ against $(r_{H_2}^{0.5} + r_{D_2}^{0.5} \cdot [\text{KIE}]_{D_2}^{-0.5})$ gives a linear curve: K_a = (Slope)^2 ; k_a = (Intercept)^2 ; k_{-a}= (Slope/Intercept)^2	

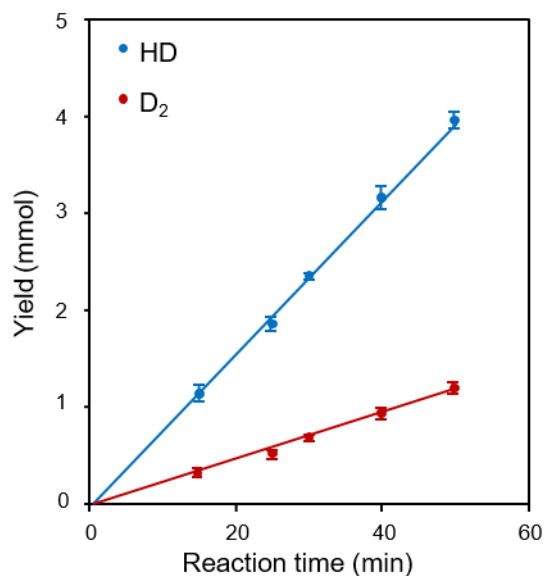**Figure 3.1.** Yields of HD and D$_2$ as a function of reaction time. The error bar is obtained from four times repetitions. Reaction conditions: 5 mg Pt/Silicalite-1, 30 mL D$_2$O, 323 K, 30 bar H$_2$, stirring at 700 rpm.

A typical reaction result of 30 bar H$_2$ with 30 mL D$_2$O over Pt/Silicalite-1 at 323 K is shown in **Figure 3.1**, as the yields of HD and D$_2$ with reaction time. Both HD and D$_2$

increase linearly from the beginning of the reaction till at least 50 min. This indicated that the period required to reach a steady state reaction was very short thus negligible in our reaction time scale. Re-adsorption of HD and D$_2$ was also negligible within the reaction time because of the largely excess of H$_2$ that the fraction of D atom in the gas phase mixture was below 2% after 50 min. Nevertheless, the re-adsorption became substantial when the D-fraction in gas phase reached above 8%, making the plot deviation from linearity after 300 min (**Figure 3.2**). All our experiment data were collected before the gas phase D-fraction exceeded 5 % to exclude HD and D$_2$ re-adsorption. The desorption rates of HD and D$_2$ were obtained from the slopes in **Figure 3.1**, as (82 ± 4) µmol·min^{-1} and (25 ± 2) µmol·min^{-1}, respectively. Using these two values, the desorption rate of H$_2$ was calculated to be (79 ± 10) µmol·min^{-1} according to Equation 3.26.
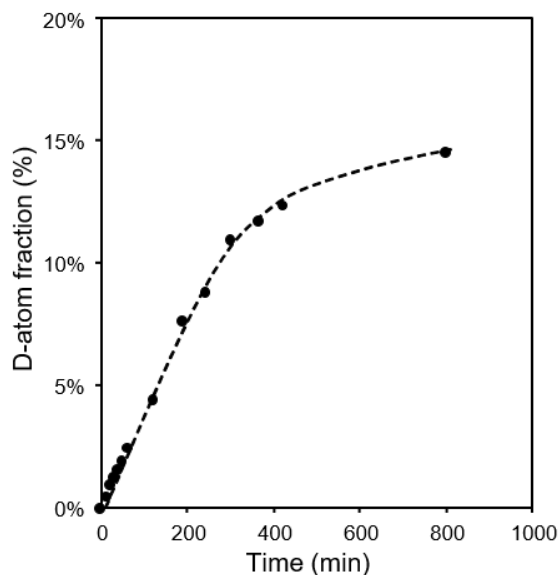
Figure 3.2. The fraction of D atoms in the gas mixture with reaction time over Pt/Silicalite-1. Reaction conditions: 5 mg Pt/Silicalite-1, 30 mL D$_2$O, 323 K, 30 bar H$_2$, stirring at 700 rpm.

In the same way, a series of H$_2$, HD and D$_2$ desorption rates over Pt/Silicalite-1 and Pt/HMFI-24 at different H$_2$ pressures and different temperatures were measured (**Table A3.1** in **Appendix**). They were plotted in the manner of Equation 3.25 in **Figure 3.3**. Each plot under a fixed temperature showed a linearly decreasing trend, in good agreement with the prediction by Equation 3.25. The values of K_a and k_a were obtained by linear fitting of the plots. For example, linear fitting of the red plot in **Figure 3.3a**, which was the reaction result of Pt/Silicalite-1 at 303 K, gave a slope of 0.529 and an intercept of 1.52,

corresponding to K_a of 0.28 bar^{-1} and k_a of 2.3 s^{-1}·bar^{-1}; further k_{-a} was calculated to be 8.2s^{-1} as the division of k_a by K_a. All the adsorption rate and equilibrium constants were summarized in **Table 3.8**.
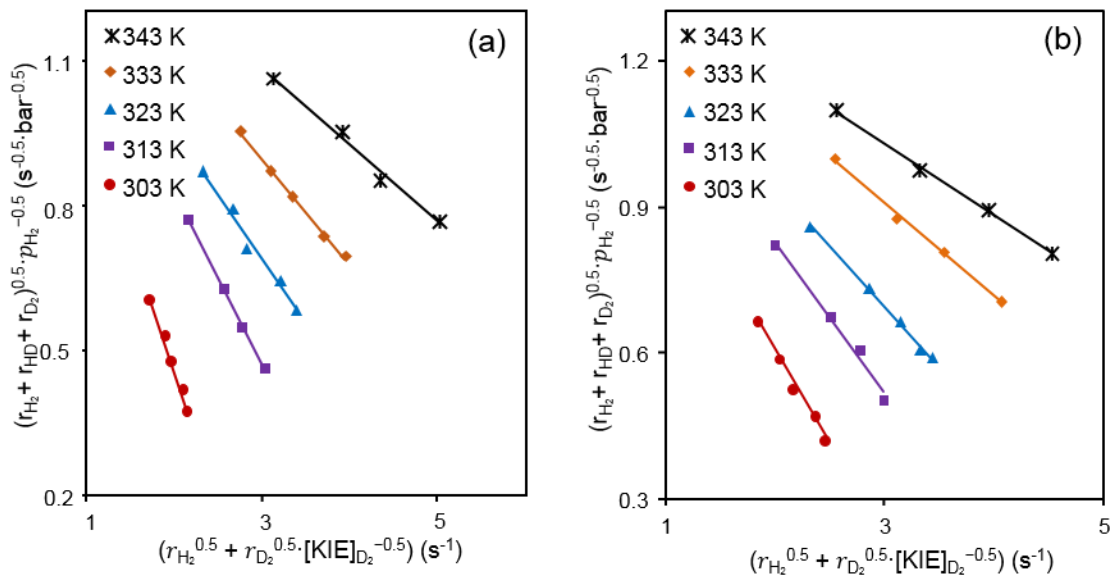
Figure 3.3. Reaction kinetic results over Pt/Silicalite-1 (a) and Pt/HMFI-24 (b) under different pressures and temperatures plotted using Equation 3.25.

Table 3.8. Adsorption and desorption rate constants and adsorption equilibrium constants over Pt/Silicalite-1 and Pt/HMFI-24 at temperatures from 303 K to 343 K. (Rate constant and equilibrium constant values have relative deviations of ~ 10%).

Temp.(K)	Pt/Silicalite-1			Pt/HMFI-24		
	k_{-a} (s^{-1})	k_a (s^{-1}bar^{-1})	K_a (bar^{-1})	k_{-a} (s^{-1})	k_a (s^{-1}bar^{-1})	K_a (bar^{-1})
303	8.2	2.3	0.28	13	1.8	0.14
313	19	2.3	0.12	22	2.0	0.091
323	31	2.2	0.072	34	2.0	0.059
333	50	2.4	0.048	61	2.2	0.036
343	96	2.4	0.025	100	2.2	0.021
Energy (kJ·mol^{-1})	Desorption barrier	Adsorption barrier	Adsorption heat	Desorption barrier	Adsorption barrier	Adsorption heat
	51 ± 3	1 ± 2	50 ± 3	44 ± 3	3 ± 2	41 ± 3

The adsorption isotherm of H₂ on Pt/Silicalite-1 in water was compared with that in the gas phase in **Figure 3.4a**. In the gas phase, H₂ adsorption was very strong so that the saturated adsorption was readily reached at a H₂ pressure below 0.1 bar. In contrast, at 0.1 bar the

Pt/Silicatalie-1 in water had a coverage of only 0.18 and the saturated adsorption required an H_2 pressure as high as above 1000 bar. The same trend was also observed on Pt/HMFI-24 (**Figure 3.4b**). The weak adsorption in water than in the gas phase was reflected by the lower adsorption heat in water. The H_2 adsorption heat on Pt in the gas phase was reported experimentally[8-15] and theoretically[16-22] to be in the range of $60 - 100$ kJ·mol^{-1}, depending on the coverage and exposed lattice surfaces. The value is substantially higher than the measured adsorption heat on Pt in water, (50 ± 3) kJ·mol^{-1} for Pt/Silicalite-1 and (41 ± 3) kJ·mol^{-1} for Pt/HMFI-24. Considering that the Pt surface in water is covered by multilayers of water, the lower H_2 adsorption heat in water compares to that in the gas phase, is attributed to the presence of oriented and structured water species adsorbed on the Pt surface.[42-44] The adsorption of H_2 on Pt surface competes with that of water, substituting water and disrupting the well-structured water chains or oligomers on a Pt surface. Therefore, part of the H_2 adsorption heat is compensated by the energy required to desorb water from Pt surface to bulk phase water. Furthermore, the H_2 adsorption strength will be affected by the adsorption state/strength of water on Pt.

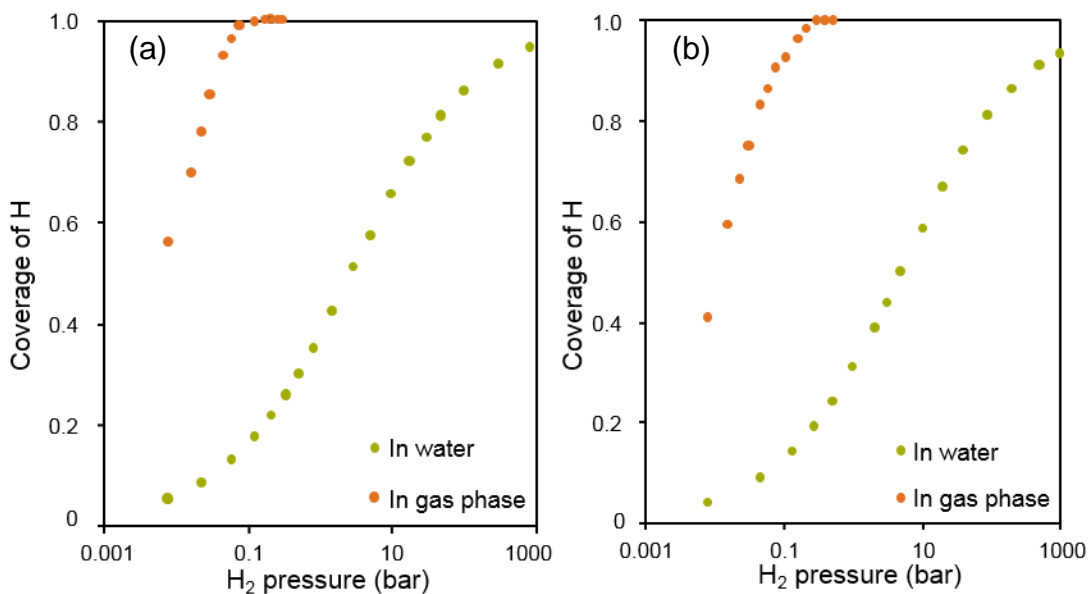**Figure 3.4.** Adsorption isotherm of H_2 on (a) Pt/Silicalite-1 and (b) Pt/HMFI-24 in the gas phase and water phase at 298 K. (Gas phase isotherm was measured by H_2-chemisorption.) Isotherm in water was plotted by using dissociative adsorption model and the adsorption equilibrium constant at 298 K. The adsorption equilibrium constant at 298 K was obtained based on the constants at 303 – 343 K and Van't Hoff equation.

The activation energy of H_2 adsorption and desorption and the adsorption heat were obtained by using the Arrhenius equation and Van't Hoff equation (**Figure 3.5**). For both Pt/Silicalite-1 and Pt/HMFI-24, the H_2 adsorption rate constants k_a were hardly changed with temperature. Almost no activation energy was required for the adsorption of H_2 on Pt, i.e. (1 ± 2) kJ·mol^{-1} on Pt/Silicalite-1 and (3 ± 2) kJ·mol^{-1} on Pt/HMFI-24. This agreed with the previous study which reported that the dissociative chemisorption process was nearly barrierless on the Pt.[16, 20, 36] The desorption rate constants k_{-a} increased with an increase of temperature, with desorption activation energies of (51 ± 3) kJ·mol^{-1} on Pt/Silicalite-1 and (44 ± 3) kJ·mol^{-1} on Pt/HMFI-24. The adsorption equilibrium constants K_a decreased with temperature, showing an exothermic process. The adsorption heats were (50 ± 3) kJ·mol^{-1} on Pt/Silicalite-1 and (41 ± 3) kJ·mol^{-1} on Pt/HMFI-24. The higher adsorption heat of ~9 kJ·mol^{-1} on Pt/Silicalite-1 over Pt/HMFI-24 was caused by the acidity of the H-MFI-24 support. It was reported that H binding energy (HBE) of Pt was sensitive to the acid-base properties of the surrounding environments.[38, 39, 45] For example, the HBE of both Pt (110) and (100) surface decreased about 15 kJ·mol^{-1} with the pH changed from 13 to 0.[38] Therefore, the acid sites in HMFI provided an acidic environment for Pt which lowered the HBE and decreased the adsorption heat of H_2 on Pt. Whereas Silicalite-1 contained no acid sites thus Pt was in a neutral environment, resulting in a higher HBE and a higher H_2 adsorption heat. It was speculated that the presence of adjacent hydronium ions had an impact on the dipole orientation or dipole moment of adsorbed water on the Pt surface,[39, 45, 46] strengthening the adsorption of water, and consequently weakening the competitive adsorption of H_2.
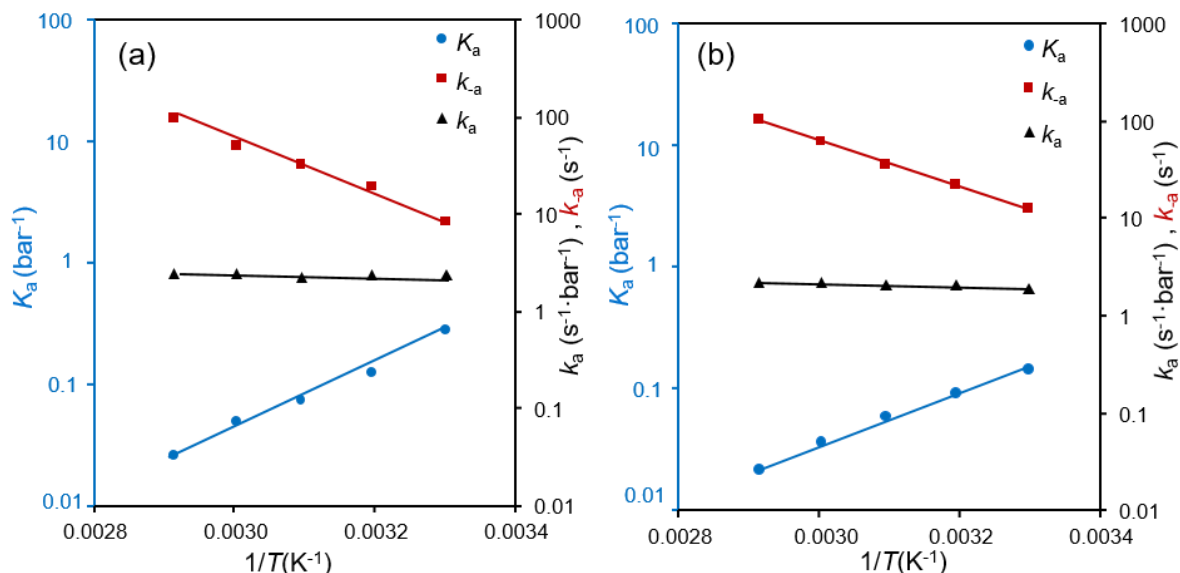
Figure 3.5. Arrhenius plots of adsorption and desorption rate constants and Van't Hoff plot of adsorption equilibrium constants, in H_2 adsorption on Pt/Silicalite-1 (a) and Pt/HMFI-24 (b) in water.

3.4. Conclusions

In conclusion, a practical method was established to determine the adsorption kinetics and thermodynamics of H_2 on transition metal immersed in water, based on the reaction of gas phase H_2 with liquid D_2O, as shown **in Figure 3.6**. The desorption rates of H_2, HD and D_2, the H_2 pressure and the adsorption rate constant and equilibrium constant have a correlation described in Equation 3.25.

$$(r_{H_2} + r_{HD} + r_{D_2})^{0.5} p_{H_2}^{-0.5} = k_a^{0.5} - \left(r_{H_2}^{0.5} + r_{D_2}^{0.5}[KIE]_{D_2}^{-0.5}\right) K_a^{0.5} \qquad (3.25)$$

By measuring the formation rates of HD and D_2 in the reaction, particularly their variation with H_2 pressure, the adsorption rate constant and equilibrium constant were obtained by fitting the data using Equation 3.25. Applying this method to Pt/MFI samples, the H_2 adsorption heat on Pt/Silicalite-1 and Pt/HMFI-24 were determined to be (50 ± 3) kJ·mol⁻¹ and (41 ± 3) kJ·mol⁻¹, respectively. In addition, this approach allows the determination of adsorption equilibrium constants and the rate constants under operando conditions of catalysts, which could shed light on the understanding of H_2 activation on working catalysts and their catalytic performance in hydrogenation/hydrogenolysis in the water phase.
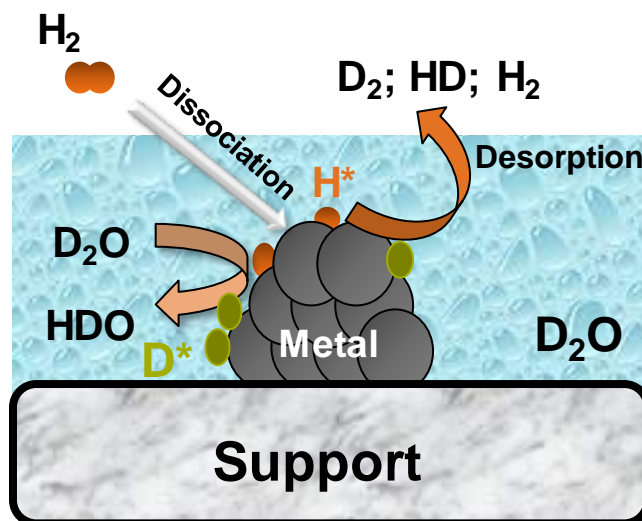
Figure 3.6. Reactions of gas H_2 with liquid D_2O into gas D_2, HD and liquid HDO over supported transition metal.

3.5. Appendix

Table A3.1. The desorption rates of H_2, HD and D_2 normalized to the number of surface Pt over Pt/Silicalite-1 (A3.1$_{a1-a5}$) and Pt/HMFI-24 (A3.1$_{b1-b5}$) at 303 – 343 K. (Values for HD and D_2 have relative deviations of 5%; values for H_2 have a relative deviation of 10%).

Table A3.1$_{a1}$ (303 K)

Pressure (bar)	Desorption rate (mol·mol$_{Pt\ surf.}^{-1}$·s^{-1})		
	HD	D_2	H_2
10	1.70	0.66	1.31
15	1.84	0.55	1.84
20	1.97	0.57	2.07
30	2.41	0.84	2.07
40	2.56	0.89	2.20

Table A3.1$_{a2}$ (313 K)

Pressure (bar)	Desorption rate (mol·mol$_{Pt\ surf.}^{-1}$·s^{-1})		
	HD	D_2	H_2
10	2.77	1.15	1.99
20	3.28	0.85	3.75
30	3.56	0.83	4.59
50	4.10	0.88	5.70

Table A3.1$_{a3}$ (323 K)

Pressure (bar)	Desorption rate (mol·mol$_{Pt surf.}^{-1}$·s^{-1})		
	HD	D$_2$	H$_2$
10	3.59	2.55	1.49
15	4.54	2.40	2.53
20	4.69	1.80	3.62
30	5.54	1.71	5.30
40	5.76	1.53	6.39

Table A3.1$_{a4}$ (333 K)

Pressure (bar)	Desorption rate (mol·mol$_{Pt surf.}^{-1}$·s^{-1})		
	HD	D$_2$	H$_2$
10	3.83	1.01	4.29
15	4.72	1.18	5.55
20	5.43	1.31	6.61
30	6.45	1.47	8.32
40	8.38	2.42	8.51

Table A3.1$_{a5}$ (343 K)

Pressure (bar)	Desorption rate (mol·mol$_{Pt surf.}^{-1}$·s^{-1})		
	HD	D$_2$	H$_2$
10	4.48	1.39	5.41
20	7.37	2.48	8.25
30	8.51	2.55	10.7
50	11.9	3.86	13.7

Table A3.1$_{b1}$ (303 K)

Pressure (bar)	Desorption rate (mol·mol$_{Pt surf.}^{-1}$·s^{-1})		
	HD	D$_2$	H$_2$
10	2.08	0.99	1.31
15	2.40	0.94	1.83
20	2.38	0.67	2.51
30	2.67	0.66	3.26
40	2.76	0.63	3.60

Table A3.1$_{b2}$ (313 K)

Pressure (bar)	Desorption rate (mol·mol$_{Pt\ surf.}^{-1}$·s^{-1})		
	HD	D$_2$	H$_2$
10	2.31	3.88	0.41
20	4.16	3.37	1.53
30	5.14	3.73	2.11
50	5.92	4.35	2.39

Table A3.1$_{b3}$ (323 K)

Pressure (bar)	Desorption rate (mol·mol$_{Pt\ surf.}^{-1}$·s^{-1})		
	HD	D$_2$	H$_2$
10	3.53	2.03	1.82
20	5.10	2.37	3.24
30	6.32	3.11	3.78
40	7.11	3.59	4.16
50	7.92	6.90	2.68

Table A3.1$_{b4}$ (333 K)

Pressure (bar)	Desorption rate (mol·mol$_{Pt\ surf.}^{-1}$·s^{-1})		
	HD	D$_2$	H$_2$
10	4.75	4.33	1.13
20	6.43	7.24	1.24
30	7.85	8.60	1.55
50	10.6	9.88	2.47

Table A3.1$_{b5}$ (343 K)

Pressure (bar)	Desorption rate (mol·mol$_{Pt\ surf.}^{-1}$·s^{-1})		
	HD	D$_2$	H$_2$
10	3.58	7.99	0.47
20	6.90	7.99	1.29
30	10.9	9.27	3.73
50	14.2	13.9	4.24

3.6. Associated content

Publication

This chapter is to be submitted in Angewandte Chemie. The content and structure of Chapter 3 are different from the manuscript.

Contributions

In this work, Dr. Yue Liu supervised the topic of determination of H_2 adsorption heat on transition metals in the water phase. Guoju Yang contributed to the design of the experiments and operating setups, and data analysis and manuscript writing. Xi Chen participated in part of experiments operation. Johannes A. Lercher was responsible for data discussion, supervising and manuscript preparation. Dr. Yue Liu and Prof. Dr. Johannes A. Lercher are the principal investigators of this work.

3.7. References

[1] A.M. Ruppert, K. Weinberg, R. Palkovits, *Angew. Chem. Int. Ed.,* 51 (**2012**) 2564-2601.

[2] B. Delmon, *Catal. Lett.,* 22 (**1993**) 1-32.

[3] J.K. Nørskov, T. Bligaard, A. Logadottir, *et al.*, *J. Electrochem. Soc.,* 152 (**2005**) J23-J26.

[4] H.A. Gasteiger, N.M. Marković, *Science,* 324 (**2009**) 48-49.

[5] Y.X. Liu, G.F. Zhao, D.S. Wang, *et al.*, *Natl Sci Rev,* 2 (**2015**) 150-166.

[6] P. Barbaro, F. Liguori, N. Linares, *et al.*, *Eur. J. Inorg. Chem.,* (**2012**) 3807-3823.

[7] K. Christmann, *Surf. Sci. Rep.,* 9 (**1988**) 1-163.

[8] R. Lewis, R. Gomer, *Surf. Sci.,* 17 (**1969**) 333-345.

[9] P.R. Norton, P.J. Richards, *Surf. Sci.,* 44 (**1974**) 129-140.

[10] J.B. Lantz, R.D. Gonzalez, *J. Catal.,* 41 (**1976**) 293-302.

[11] B. Poelsema, G. Mechtersheimer, G. Comsa, *Surf. Sci.,* 111 (**1981**) 519-544.

[12] M.A. Vannice, L.C. Hasselbring, B. Sen, *J. Catal.,* 95 (**1985**) 57-70.

[13] M.A. Natal-Santiago, S.G. Podkolzin, R.D. Cortright, *et al.*, *Catal. Lett.,* 45 (**1997**) 155-163.

[14] B.E. Spiewak, R.D. Cortright, J.A. Dumesic, *J. Catal.,* 176 (**1998**) 405-414.

[15] E. Bus, J.A. van Bokhoven, *PCCP,* 9 (**2007**) 2894-2902.

[16] R.A. Olsen, G.J. Kroes, E.J. Baerends, *J. Chem. Phys.,* 111 (**1999**) 11155-11163.

[17] G.W. Watson, R.P.K. Wells, D.J. Willock, *et al.*, *J. Phys. Chem. B,* 105 (**2001**) 4889-4894.

[18] X. Liu, H. Dilger, R.A. Eichel, et al., *J. Phys. Chem. B,* 110 (**2006**) 2013-2023.

[19] Y. Okamoto, *Chem. Phys. Lett.,* 429 (**2006**) 209-213.

[20] C.G. Zhou, J.P. Wu, A.H. Nie, *et al.*, *J Phys Chem C,* 111 (**2007**) 12773-12778.

[21] S.M. Kozlov, H.A. Aleksandrov, K.M. Neyman, *J Phys Chem C,* 119 (**2015**) 5180-5186.

[22] S.K. Ignatov, A.I. Okhapkin, O.B. Gadzhiev, *et al.*, *J Phys Chem C,* 120 (**2016**) 18570-18587.

[23] M.J. Climent, A. Corma, S. Iborra, *Green Chemistry,* 16 (**2014**) 516-547.

[24] J.S. Van Dyk, B.I. Pletschke, *Biotechnol. Adv.,* 30 (**2012**) 1458-1480.

[25] H. Zhang, X. Gao, J. Ren, *et al.*, *J. Mol. Catal. B: Enzym.,* 105 (**2014**) 118-125.

[26] W.J.M. Rootsaert, L.L. Vanreijen, W.M.H. Sachtler, *J. Catal.,* 1 (**1962**) 416-431.

[27] B. Sen, P. Chou, M.A. Vannice, *J. Catal.,* 101 (**1986**) 517-521.

[28] B. Sen, M.A. Vannice, *J. Catal.,* 130 (**1991**) 9-20.

[29] P. Chou, M.A. Vannice, *J. Catal.,* 104 (**1987**) 1-16.

[30] A. Guerrero, M. Reading, Y. Grillet, *et al.*, *Zeitschrift für Physik D Atoms, Molecules and Clusters,* 12 (**1989**) 583-586.

[31] H. Conrad, G. Ertl, E.E. Latta, *Surf. Sci.,* 41 (**1974**) 435-446.

[32] G.D. Weatherbee, C.H. Bartholomew, *J. Catal.,* 87 (**1984**) 55-65.

[33] S. Gudmundsdottir, E. Skulason, K.J. Weststrate, *et al.*, *PCCP,* 15 (**2013**) 6323-6332.

[34] J. Greeley, M. Mavrikakis, *J. Phys. Chem. B,* 109 (**2005**) 3460-3471.

[35] J. Fearon, G.W. Watson, *J. Mater. Chem.,* 16 (**2006**) 1989-1996.

[36] A.S. Zyubin, T.S. Zyubina, Y.A. Dobrovol'skii, *et al.*, *Russ J Inorg Chem,* 57 (**2012**) 1460-1469.

[37] G.S. Karlberg, T.F. Jaramillo, E. Skulason, *et al.*, *Phys. Rev. Lett.,* 99 (**2007**) 126101.

[38] W. Sheng, Z. Zhuang, M. Gao, *et al.*, *Nat Commun,* 6 (**2015**).

[39] J. Zheng, W. Sheng, Z. Zhuang, *et al.*, *Science Advances,* 2 (**2016**).

[40] E. Buncel, C.C. Lee, Isotopes in Organic Chemistry, Elsevier: Amsterdam., **1977**.

[41] K.K. Irikura, *J. Phys. Chem. Ref. Data,* 38 (**2009**) 749-749.

[42] L. Árnadóttir, E.M. Stuve, H. Jónsson, *Surf. Sci.,* 604 (**2010**) 1978-1986.

[43] H. Ogasawara, B. Brena, D. Nordlund, *et al.*, *Phys. Rev. Lett.,* 89 (**2002**) 276102.

[44] H. Ibach, S. Lehwald, *Surf. Sci.,* 91 (**1980**) 187-197.

[45] J. Durst, A. Siebel, C. Simon, *et al.*, *Energy & Environmental Science,* 7 (**2014**) 2255-2260.

[46] S. Trasatti, *Journal of Electroanalytical Chemistry and Interfacial Electrochemistry,* 39 (**1972**) 163-184.

Chapter 4

Influence of support acidity on the Pt-catalyzed hydrogenation of phenol in the aqueous phase

The hydrogenation activity of five Pt/MFI samples with varying BAS concentrations in the aqueous phase was tested by hydrogenation reaction of phenol. The hydrogenation rate of phenol showed a positive correlation with the hydronium ion concentrations in MFI micropores. Furthermore, catalysts with higher hydronium ion concentrations showed weaker adsorption of phenol. The hydronium ions in adjacent to Pt clusters in MFI micropores changed the H-addition pathways. In the presence of hydronium ions, protonation of the aromatic ring coupled with electron transfer led to a higher rate than the conventional addition of hydrogen atom. This changed the reaction order of H_2 from 0.5 to 1, and decreased the corresponding activation enthalpy from 94 to 63 $kJ \cdot mol^{-1}$.

4.1. Introduction

The conversion of biomass into fuels and chemical feedstocks is an alternative to reduce the dependence of the world on crude oil. However, its corrosive nature, low vapor pressure, and high viscosity limits its extensive application. Hydrodeoxygenation over bifunctional catalysts of metal supported on zeolite provides an efficient method to remove the high oxygen content within the biomass to produce hydrocarbon.

It has been established that catalytic activity of supported metal catalysts can be enhanced by the support properties. Sachtler et.al accounted for the higher turnover frequency of neopentane conversion over the acid Pd/NaY catalysts by the formation of $[Pd_n-H_x]^{x+}$.[1] Some reports attributed the acid promotion to the alteration of the metal band structure induced by proximal protons.[2-5] There were also some explanations for acid-promoted phenomenon pointing out the presence of acid can either stabilize reduced form of metal[6, 7] or prevent the metal from leaching, positioning and coke deposition[8, 9].

In a recent study by Song and her co-workers, the higher hydrogenation activity of phenol over Ni/HMFI with more BAS concentration was partially attributed to the enrichment of phenol and the reaction intermediates in the pores of the more acidic zeolite. Furthermore, they also proposed concentration of active H for phenol hydrogenation would be not only contributed by the dissociative adsorption of H_2 on the Ni particle, but also by the concentration of available protons adjacent to Ni particles, i.e. the Brønsted acid site of zeolite delivered an additional proton for phenol hydrogenation process. [10] However, there was no direct evidence that BAS in zeolite micropores facilitated adsorption of phenol in the aqueous phase. Moreover, the catalytic role of BAS in the hydrogenation process was not clarified in details by them.

Although several models have been proposed, the catalytic role and intrinsic impact of support acidity on metal-catalyzed reaction still remains unclear. Therefore, the aim of this chapter is to investigate the intrinsic impact of support acidity on the process of platinum-catalyzed phenol hydrogenation in the aqueous phase. In this chapter, the Pt/HMFI sample with higher BAS concentration showed a higher hydrogenation activity. Detailed kinetic

studies provided insights into the effect of acid promotion, in which different H-addition pathways of phenol in the presence or absence of hydronium ions were reported.

4.2. Experimental

4.2.1. Chemicals and Materials

The following chemicals were used as received in this work: NaCl (99.5 %, Sigma-Aldrich), Na_2SO_4 (99.0 %, Sigma-Aldrich); Phenol (99.0 %, Sigma-Aldrich), Cyclohexanol (99.0 %, Sigma–Aldrich), Cyclohexanone (99.0 %,Sigma-Aldrich), 1,4-Dimethoxybenzene (99.0 %, Sigma-Aldrich), D_2O (99.9 atom % D, Sigma-Aldrich), Chloroform-d (99.8 atom % D, Sigma-Aldrich), Ethyl acetate (99.9 %, Sigma-Aldrich), Nitrogen (99.999 %, Westfalen), Hydrogen (99.999 %, Westfalen) and Oxygen (99.9999 %, Westfalen).

4.2.2. Preparation and characterizations of Pt/MFI catalysts.

Five Pt/MFI samples with varying BAS concentrations, i.e. Pt/HMFI-24, Pt/HMFI-40, Pt/HMFI-120, Pt/HMFI-430, Pt/Silicalite-1, were used in this chapter. The preparation procedures of these catalysts have been reported in Chapter 2 (Part 2.2. Experimental), thereby no future descriptions herein.

Most of the characterization measurements of these catalysts, such as AAS, STEM, H_2 chemisorption, IR, *etc.*, were also introduced in Chapter 2. While the measurement of phenol adsorption on the catalysts in the aqueous phase was described below:

The adsorption isotherms of phenol from aqueous solutions on Pt/HMFI-24 and Pt/Silicalite-1 were determined at room temperature and fitted with Langmuir-type isotherm to obtain phenol adsorption constants for both samples. Specifically, 20 mg of catalyst (m) was immersed in 2 mL (V) of a phenol solution at a given concentration (c_0). The equilibrium concentration (c_e) was measured after 24 h using UV-VIS (Hitachi Spectrophotometer U-3000 series, $\lambda_{max} = 264$ nm, externally calibrated). The phenol uptake (q) was determined by the change in the bulk concentration, the volume of the solution and mass of the solid sample, as shown in Equation 4.1:

$$q = V \cdot (c_0 - c_e) \cdot m^{-1} \qquad (4.1)$$

4.2.3. Catalytic measurements

The aqueous phase hydrogenation of phenol was performed in an autoclave (Parr Instrument, 300 mL). Typically, 1.0 – 3.0 g phenol, 0.01 g Pt-based catalyst, and 100 mL distilled H_2O were charged into the autoclave followed by pressurizing H_2. Subsequently, it was heated to the desired reaction temperature. After a certain time, the autoclave was quenched by fast cooling to 278 K in an ice bath. The organic products were extracted from the aqueous phase with 20 mL ethyl acetate for three times. To enhance the extraction efficiency, sodium chloride was added to the reaction mixture. The organic phase was dried over sodium sulfate. 1,4-dimethoxybenzene was added in the extracted solution as internal standard. Products were qualitatively and quantitatively analyzed by a GC-MS (Agilent 7890 B-Agilent 5975C MS) equipped with an HP–5 capillary column (30 m × 250 µm × 0.25 µm).

H/D substitution reaction of phenol with catalysts in D_2O was carried out in a 100 mL of autoclave (Parr Instrument). Typically, 5 mg catalyst and 0.3 g phenol were mixed with the 30 mL D_2O. Hydrogen or nitrogen was charged in the autoclave (ambient temperature). Then, after the required temperature was reached, the stirring was initiated and the reaction time was recorded from that point. After the reaction, the organic products were extracted with ethyl acetate and analyzed by MS (Agilent 5975C) or with chloroform-d for ^{1}H MAS NMR analysis (using an Avance III 500 System from Bruker Biospin with an Ultra Shield 500 MHz magnet and a SEI 500 S2 probe head).

4.3. Results and Discussion

4.3.1. Catalysts characterization

The main physicochemical properties of five Pt/MFI samples were shown in details in Chapter 2. Here they are also compiled in **Table 4.1**. The Pt contents of five samples are at around 1wt. %. The textural properties and Pt particle size of these catalysts are all comparable. Notably, the concentration of BAS expectedly decrease from 658 to 0 µmol·g^{-1} with the growing framework Si/Al ratio of the support from 24 to infinite. LAS concentrations are less than 54 µmol·g^{-1} for all five samples.

Table 4.1. Physical and chemical properties of Pt/MFI samples.

Catalyst	Si/Al ratio[a]	BET (m$^2 \cdot$ g^{-1})	Pt[a] wt %	Pt size[b] nm	Dispersion[c] (%)	Acid site[d] (μmol$\cdot$ g^{-1}) BAS	LAS
Pt/HMFI-24	24	450	0.99	1.1	99.8	658	54
Pt/HMFI-40	40	453	0.93	1.2	98.3	414	40
Pt/HMFI-120	120	444	0.95	2.0	50.2	112	34
Pt/HMFI-430	430	422	1.01	1.9	37.1	48	2.6
Pt/Silicalite-1	∞	362	1.00	1.0	100	0	0

[a] Element composition determined with AAS.

[b] Particle size measured by TEM.

[c] Pt dispersion Determined by H$_2$ chemisorption.

[d] the acidic properties probed by IR spectra of adsorbed pyridine (Py-IR).

4.3.2. Catalytic hydrogenation of phenol over Pt/MFI catalysts

In order to explore the roles of acid and metal sites in the bifunctional Pt/HMFI catalysts, the hydrodeoxygenation reactions of phenol were performed in the aqueous phase. Based on the mechanism proposed by Zhao *et al.*, [10, 11] the phenol hydrodeoxygenation reaction in aqueous phase proceeded in the following pathway (**Scheme 4.1**): phenol was firstly hydrogenated on Pt into cyclohexanone as the primary product, which was subsequently hydrogenated to cyclohexanol. In the presence of hydronium ion, cyclohexanol was dehydrated to cyclohexene, which was finally hydrogenated to cyclohexane. The overall reaction pathway required two functions of Pt/HMFI samples, with Pt catalyzing the hydrogenation of aromatic ring and alkene, and acid sites mediating the dehydration of cyclohexanol intermediate.
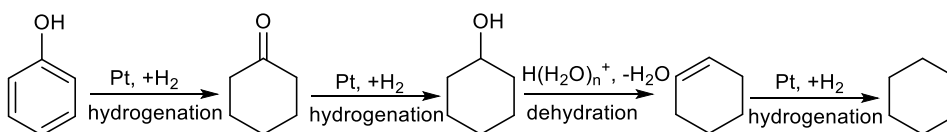
Scheme 4.1. Reaction pathway for phenol hydrodeoxygenation over Pt/HMFI in the aqueous phase.[11]

The apparent rate for phenol hydrogenation on Pt was expressed as

$$r = k \cdot C_{Phenol}{}^{m} \cdot p_{H2}{}^{n}, \qquad (4.2)$$

where k is rate constant, m and n denote the reaction orders of phenol and H_2. The conversion in phenol hydrogenation described the decline in phenol concentration in the aqueous phase.

As shown in **Figure 4.1**, the turnover frequencies of phenol hydrogenation (TOFs, normalized to surface Pt atoms) measured at the temperature of $433 - 493$ K, followed the sequence of Pt/HMFI-24 > Pt/HMFI-40 > Pt/HMFI-120 > Pt/HMFI-430 > Pt/Silicalite-1, which was in agreement with the increasing Brønsted acid site concentrations of the respective supports (TOF values are listed in **Table A4.1** in **Appendix**). For example, at 453 K, the TOF on Pt/HMFI-24 was 4.3 h^{-1}, which was more 10 times higher than that on Pt/Silicalite-1 (0.4 h^{-1}). In addition, the apparent activation enthalpies of each catalyst decreased from 94 to 63 kJ·mol^{-1} with the increasing of support BAS concentration from 0 to 658 $\mu mol·g^{-1}$ (**Table A4.1**). Both apparent TOFs and apparent activation enthalpies suggested that the presence of support acidity not only catalyze dehydration of cyclohexanol but also promote the rate of the phenol hydrogenation over Pt.
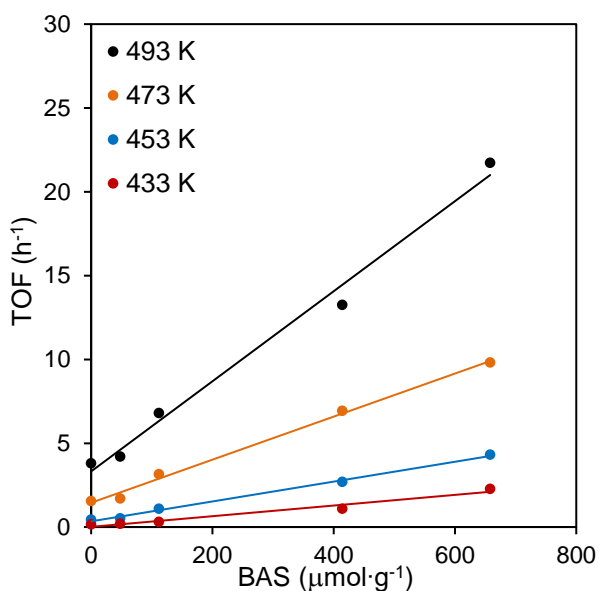

Figure 4.1. Turnover frequencies as a function of support acidity. Reaction conditions: 1.0 g phenol, 0.01 g catalyst, 40 bar H_2, $433 - 493$ K, stirring at 700 rpm.

In the previous study, the higher hydrogenation activity of phenol over Ni/HMFI with more BAS concentration was attributed to the enhanced adsorption of phenol, based on IR

measurement in the gas phase.[10] In this study, the adsorption isotherm of phenol in the aqueous phase under reaction conditions was obtained, in which the phenol uptake on Pt/HMFI-24 was actually lower than that on Pt/Silicalite-1 (**Figure. 4.2**). The different result of phenol adsorption in the gas phase and in the water phase could be attributed to the polar selectivity of zeolite micropores. In the micropores of H-MFI-24, the Brønsted acid sites inside led to a high polarity of the pore system, which preferred to adsorbing more water than phenol molecules. In contrast, the micropores of Silicalite-1 favored adsorbing phenol over water, due to the hydrophobicity and organophilicity of this pure siliceous zeolite. The phenol adsorption result under reaction conditions indicate that the rate enhancement of phenol hydrogenation by the hydronium ions is not from the changes in the phenol adsorption. In addition, the adsorption heat of hydrogen on Pt/HMFI-24 (41 $\pm$ 3 kJ·mol^{-1}) was lower than on Pt/Silicalite-1 (50 $\pm$ 3 kJ·mol^{-1}), which indicates the H$_2$ adsorption on Pt surface becomes weak in the presence of hydronium ions as well.
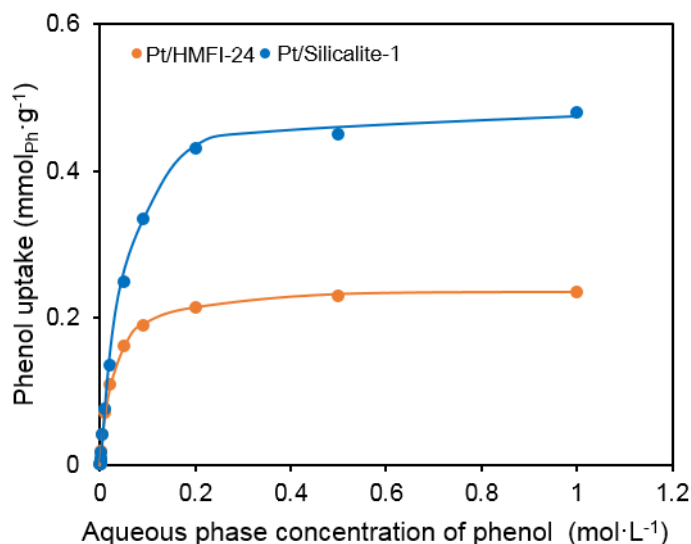

Figure 4.2. Adsorption isotherm of phenol from aqueous phase onto Pt/HMFI-24 and Pt/Silicalite-1 at 473 K.

To figure out the positive influence and essential role of hydronium ions on Pt-catalyzed phenol hydrogenation, kinetic studies on the most acidic Pt/HMFI-24 and the non-acidic Pt/Silicalite-1 were performed. Firstly, aqueous phenol solutions of 0.11–0.44 M was used to determine the reaction order of phenol over Pt/Silicalite-1 and Pt/HMFI-24. As seen in

Figure 4.3a, zero order with respect to phenol concentration on both Pt/HMFI-24 and Pt/Silicalite-1 was observed. The 0th order on phenol indicates a saturated adsorption of phenol on the Pt surface, regardless of the presence of hydronium ions. The isotherms of phenol adsorption in the aqueous phase over Pt/HMFI-24 and Pt/Silicalite-1 were in agreement with the 0th reaction order of phenol. As shown in **Figure 4.2**, the uptake of phenol is saturated under chosen reaction conditions (≥ 0.11M).
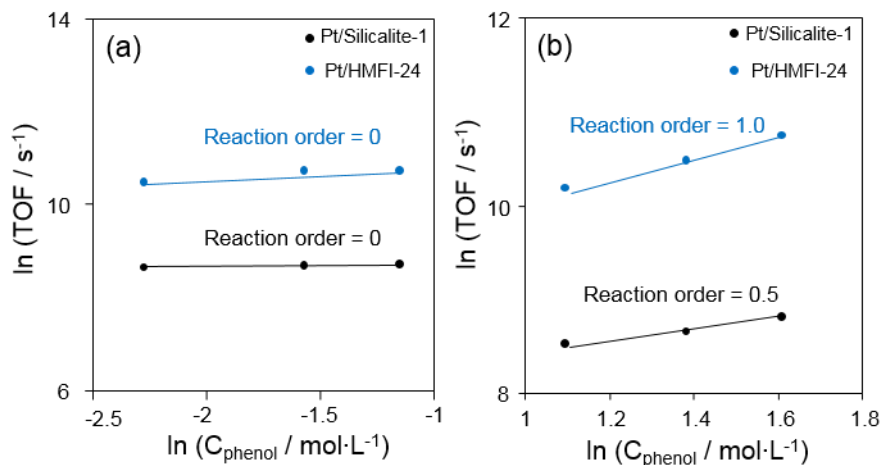

Figure 4.3. Hydrogenation of phenol over Pt/HMFI-24 and Pt/Silicalite-1 with (a) varying phenol concentration (0.11 – 0.44 M phenol; 4MPa H_2) and (b) varying hydrogen pressures (3 – 5 MPa; 1 g phenol). Reaction conditions: H_2O (100 mL), Pt/HMFI-24 and Pt-Silicalite-1 (0.01 g), at 473 K, stirring at 700 rpm.
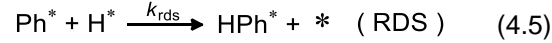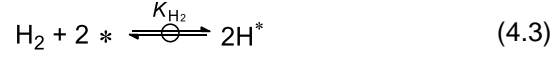
Table 4.2. Kinetic parameters in phenol hydrogenation on Pt/HMFI-24 and Pt/Silicalite-1.

Catalyst	Reaction Order		$\Delta H^{\ddagger}$ (kJ·mol^{-1})	$\Delta S^{\ddagger}$ (J·mol^{-1}·K^{-1})
	H_2	Phenol		
Pt/HMFI-24	1	0	63 ± 4	-94 ± 9
Pt/Silicalite-1	0.5	0	94 ± 3	-47 ± 7

For the reaction order in H_2 pressure, it was determined to be 0.5^{th} order for Pt/Silicalite-1, but 1st order for Pt/HMFI-24 (**Figure 4.3b**). The different H_2 reaction order implied different reaction pathways in the presence or absence of hydronium ion adjacent to Pt.

In general, H_2 dissociative adsorbs on Pt surface,[12] while phenol favors molecularly adsorption on Pt surface through a mixed σ−π interaction. [13] Therefore, the H_2 and phenol (Ph) competitive adsorption on active Pt site (*) can be described as Equations 4.3 and 4.4,

where the * represents active Pt site and Ph refers to phenol. In addition, K_{Ph} and K_{H_2} represent the equilibrium constants for H_2 and phenol adsorption, while k_{rds} refers to the rate constant of the rate-determining step.

$$H_2 + 2\ * \xrightleftharpoons{K_{H_2}} 2H^* \qquad (4.3)$$

$$Ph + \ * \xrightleftharpoons{K_{Ph}} Ph^* \qquad (4.4)$$

$$Ph^* + H^* \xrightarrow{k_{rds}} HPh^* + \ * \quad (RDS) \qquad (4.5)$$

Since it was 0.5^{th} order in H_2 for phenol hydrogenation over Pt/Silicalite-1, the rate-determining step (RDS) of first H-addition was assumed (Equation 4.5) to fit the kinetic model. Therefore, the rate equation for phenol hydrogenation over Pt/Silicalite-1 is expressed as Equation 4.6.

$$\text{Rate (Pt/Silicalite-1)} = k_{rds}\theta_{Ph^*}\theta_{H^*} \qquad (4.6)$$

H_2 and phenol adsorption is proposed to be sufficiently fast and quasi-equilibrated. The site balance equation for accessible Pt sites is straightforward, only involving H* and phenol molecule. Therefore, the surface coverage of adsorbed H atom (θ_{H^*}) and phenol (θ_{Ph^*}) is expressed in Equation 4.7 and 4.8,

$$\theta_{H^*} = \frac{K_{H_2}^{0.5} \cdot p_{H_2}^{0.5}}{1 + K_{H_2}^{0.5} \cdot p_{H_2}^{0.5} + K_{Ph} \cdot C_{Ph}} \qquad (4.7)$$

$$\theta_{Ph^*} = \frac{K_{Ph} \cdot C_{Ph}}{1 + K_{H_2}^{0.5} \cdot p_{H_2}^{0.5} + K_{Ph} \cdot C_{Ph}} \qquad (4.8)$$

in which the concentration of phenol and pressure of H_2 in aqueous solution is simplified as C_{Ph} and p_{H_2}, respectively. Eventually, the rate equation can be derived by substituting Equation 4.7 and 4.8 into rate expression (Equation 4.6), which gives:

$$\text{Rate (Pt/Silicalite-1)} = \frac{k_{rds} \cdot K_{H_2}^{0.5} \cdot p_{H_2}^{0.5} \cdot K_{Ph} \cdot C_{Ph}}{\left(1 + K_{Ph} \cdot C_{Ph} + K_{H_2}^{0.5} \cdot p_{H_2}^{0.5}\right)^2} \qquad (4.9)$$

The Equation 4.9 shows that the reaction order with respect to phenol varies from -1 to 1 and the reaction order on H_2 is 0.5^{th} when the coverages for phenol and empty sites are larger than other species.

Table 4.3. Elementary steps of phenol hydrogenation over Pt/Silicalite-1 and Pt/HMFI-24.

Description	Elementary steps		
	Pt/Silicalite-1	Pt/HMFI-24	
H_2 adsorption	$H_2 + 2* \underset{K_{H_2}}{\rightleftharpoons} 2H^*$ (4.3)	$H_2 + 2* \underset{K_{H_2}}{\rightleftharpoons} 2H^*$	(4.3)
Phenol adsorption	$Ph + * \underset{K_{Ph}}{\rightleftharpoons} Ph^*$ (4.4)	$Ph + * \underset{K_{Ph}}{\rightleftharpoons} Ph^*$	(4.4)
1st H addition	$Ph^* + H^* \xrightarrow{k_{rds}} HPh^* + *$ (4.5)	$Ph^* + H^* \underset{k_{HPh}}{\rightleftharpoons} HPh^* + *$	(4.10)
2nd H addition	fast	$HPh^* + H^* \xrightarrow{k_{rds}} H_2Ph^* +$	(4.11)

* represents accessible Pt sites.

p_{H_2} refers to H_2 pressure.

*C* refers to the concentration of corresponding species.

θ_* is the coverage of accessible Pt sites.

θ_H, θ_{Ph}, θ_{HPh^+} and *θ_{HPh^*}* are the coverage of H, phenol, protonated phenol and hydrogenated phenol.

k_{rds} refers rate constant of RDS.

K represents the equilibrium constant of the corresponding compound.

In the case of phenol hydrogenation over Pt/HMFI-24, one kinetic model with the 2nd H-addition step as the rate determining step was proposed to fit the phenol hydrogenation data, since the reaction order on H_2 measured in this work was 1. The sequence of elementary steps describing this model is listed in **Table 4.3**. Firstly, the H_2 and phenol competitively adsorbed on the accessible Pt sites as occurred on Pt/Silicalite-1 (Equation 4.3 and Eq.4.4). However, different from phenol hydrogenation on Pt/Silicalite-1, first H-addition step of phenol on Pt/HMFI-24 is fast and quasi-equilibrated in the presence of hydronium ion (Equation 4.10). The rate-determining step is second H addition to phenol in the presence of hydronium ion (Equation 4.11).

$$Ph^* + H^* \underset{k_{HPh}}{\rightleftharpoons} HPh^* + * \qquad (4.10)$$

$$HPh^* + H^* \xrightarrow{k_{rds}} H_2Ph^* + * \qquad (4.11)$$
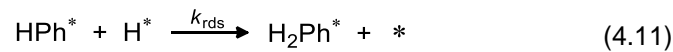
The coverage of 1st H added phenol resulting from Equation 4.10 is written as:

$$\theta_{HPh^*} = K_{Ph}K_{H_2}^{0.5}p_{H_2}^{0.5}C_{Ph}\theta_* \quad (4.12)$$

As the 2nd H-addition step is RDS (, the rate of phenol hydrogenation over Pt/HMFI-24 is expressed:

$$\text{Rate(Pt/HMFI-24)} = \ k_{rds}\theta_{\text{HPh}^*}\theta_{\text{H}^*} \quad (4.13)$$

The site balance for Pt sites on Pt/HMFI-24 involves adsorbed H, phenol and hydrogenated phenol species resulting from Eqs. (4.3, 4.4 and 4.10), thus can be written as Equation 4.14

$$1 = \theta_* + \theta_\text{H} + \theta_\text{Ph} + \theta_\text{HPh} \quad (4.14)$$

If the surface coverages of hydrogenated phenol species are assumed to be low, given the high activity of them, the site balance equation can be simplified as following:

$$1 = \theta_* + \theta_\text{H} + \theta_\text{Ph} \quad (4.15)$$

Based on the series of Eqs. (4.3 and 4.4) , the θ_H and θ_Ph are derived and substituted into Equation 4.15, then it gives:

$$1 = \theta_* + K_{\text{H}_2}^{0.5} \cdot p_{\text{H}_2}^{0.5}\theta_* + K_\text{Ph}C_\text{Ph}\theta_*,$$

where θ_* is derived to be Equation 4.16:

$$\theta_* = 1 \ / \ (1 + \ K_{\text{H}_2}^{0.5} \cdot p_{\text{H}_2}^{0.5} + \ K_\text{Ph}C_\text{Ph}) \quad (4.16)$$

Thus, the corresponding rate (Equation 4.17) can be written by combining the Equation 4.16 with Equations (4.12 and 4.13), as shown below:

$$\text{Rate (Pt/HMFI-24)} = \frac{k_{rds}K_{\text{H}_2}K_\text{Ph}K_\text{HPh}C_\text{Ph}p_{\text{H}_2}}{(1 + K_{\text{H}_2}^{0.5} \cdot p_{\text{H}_2}^{0.5} + K_\text{Ph}C_\text{Ph})^2} \quad (4.17)$$

When the coverage of phenol is much larger than the coverage of H on the surface, the reaction order of phenol varies from –1 to 1 and the reaction order of H_2 is 1, which is in consistence with the measured results in this work.

4.3.2. Different pathways for the first H-addition to phenol Pt/Silicalite-1 and Pt/HMFI-24 catalysts.

To figure out how the first H was added to phenol over Pt/Silicalite-1 and Pt/HMFI-24, hydrogenation reaction of phenol was performed in D_2O over the two catalysts, where deuterium products, i.e. D-cyclohexanol, D-cyclohexanone, as well as D-phenol were obtained. The position of D in D-phenol provided information of the first D/H addition pathways onto phenol. For the reaction over Pt/Silicalite-1, the hydrogenation selectively occurred at the ortho carbon of phenol ring, as depicted in **Scheme 4.2a.** Whereas both

ortho-C and para-C in phenol ring were favorable to be hydrogenated in the presence of hydronium ions (actually is $D(D_2O)_n^+$) over Pt/HMFI-24, as shown in **Scheme 4.2b.** The different hydrogenation position selectivity on the phenol aromatic ring indicates a different H addition route in the presence or absence of hydronium ion. The protonation of phenol aromatic ring is speculated to participate in the H-addition step in the presence of hydronium ions.
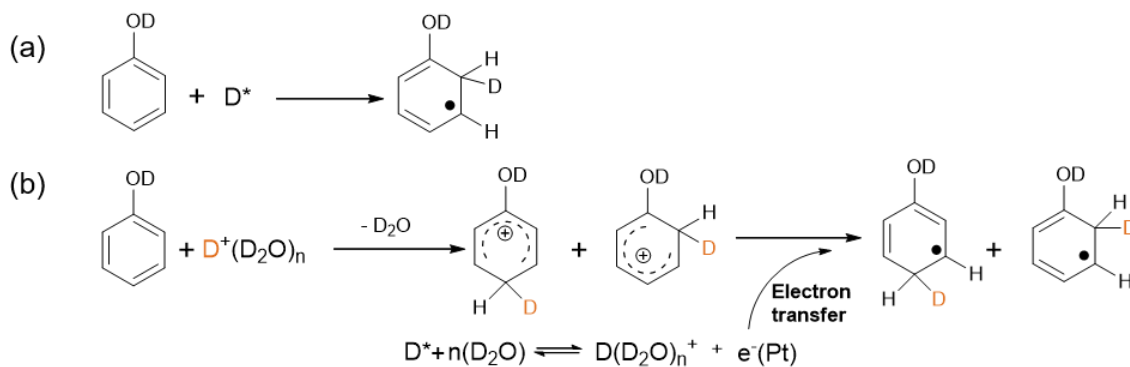
Scheme 4.2. Pathways of (a) substitution over Pt/Silicalite-1 and (b) protonation and substitution over Pt/HMFI-24.

The MS spectra of phenol after D_2O-phase hydrogenation reaction are shown in the **Figure 4.4a**. The MS spectrum gave m/z of 95.1 as the molecular ion peak reference of C_6H_5OD. The second D substituting the H on the aromatic ring yielded the ion with m/z of 96.1. The m/z of 97.1 and 98.1 ions in the MS spectrum came from further D-substituted phenol at the aromatic ring. The concentration of D-substituted phenol (m/z 95.1→96.1 and m/z 96.1→97.1) after reaction over Pt/HMFI-24 was higher under H_2 than that under N_2. This indicates H/D substitution of phenol could be promoted by the presence of Pt and H_2. The MS results were in agreement with ^1H MAS NMR results, in which the concentration of H atoms at both ortho and para position decreased after the H/D substitution reaction, as shown in the **Figure 4.4b**. Therefore, both of them pointed to the possibility of phenol ring protonation by the presence of hydronium ions under the reaction conditions.
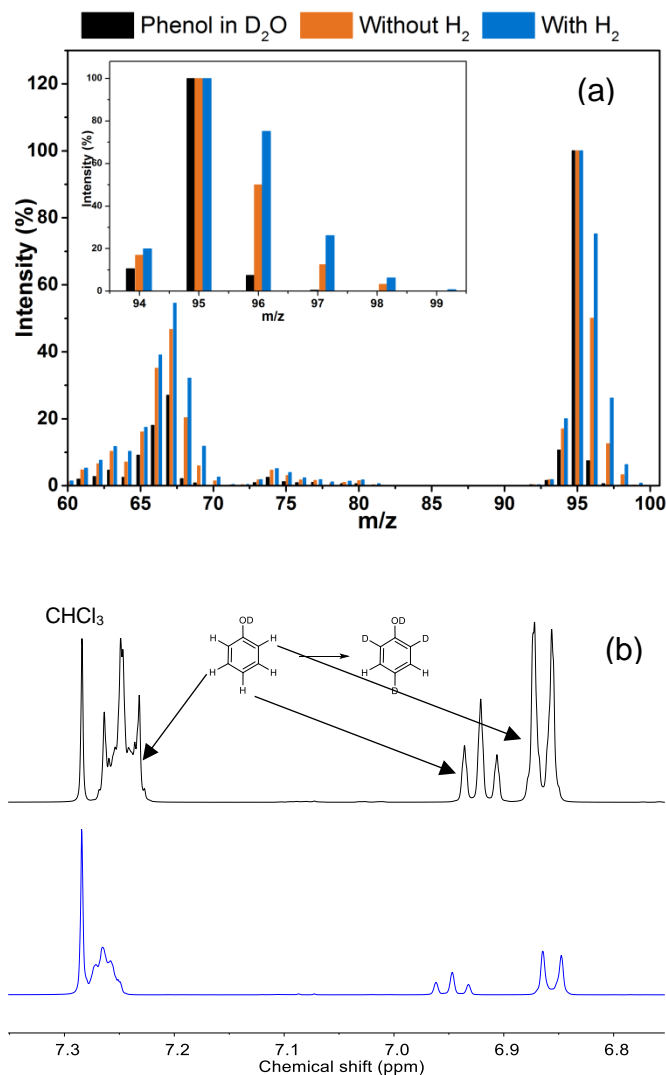
Figure 4.4. (a) Mass spectra of phenol H/D exchange reaction in D_2O over Pt/HMFI-24 in the presence (orange) and absence (blue) of H_2. Mass spectra of neat phenol in D_2O (black) is given as a reference. (b) ^{1}H MAS NMR spectra of phenol after H/D substitution reaction under H_2 (blue) and N_2 (black). Reaction conditions: 1.0 g phenol, 0.01 g Pt/HMFI-24, 100ml D_2O; at 473 K, 40 bar H_2 or N_2 (ambient temperature), stirring at 700 rpm.

Notably, the H/D substitution reaction of phenol showed the position selectivity. The H atoms at both para and ortho position were selectively replaced by D atoms, while the meta-H atoms remained almost constant, in consistency with a reported computational study.[14] However, the position selectivity was different in the reactions over Pt/Silicalite-1 or Pt/HMF-24. Specifically, the ortho-H atoms were more preferred to being substituted by D atom over Pt/Silicalite-1 (**Figure. 4.5a**), whereas the H atoms at both ortho and para position were selectively substituted by D atoms over Pt/HMFI-24, as shown in **Figure 4.5**

b. The different H-substitution preference affected by the presence of hydronium ions from MFI zeolite was depicted in **Scheme 4.3**. In terms of reaction over Pt/Silicalite-1 (**Scheme 4.3a**), H_2 firstly adsorbed and reacted with D_2O into adsorbed D atom (D*) on Pt sites. Then D* substitute the ortho-H at the aromatic ring of phenol. For Pt/HMFI-24, the reaction in the presence of hydronium ions on acid support underwent electrophilic substitution of H atom at both ortho and para position by the $D(D_2O)_n^+$, as shown in **Scheme 4.3b**. As the transition state of phenol substitution and hydrogenation was same, the difference of H/D substitution pathways on Pt/Silicalite-1 and Pt/HMFI-24 indicated a different H addition route of phenol hydrogenation in the absence or presence of hydronium ion. Therefore, it was proposed that the protonation of phenol via electrophilic attack by hydronium ions participated in the first H-addition step of phenol over Pt/HMFI-24.
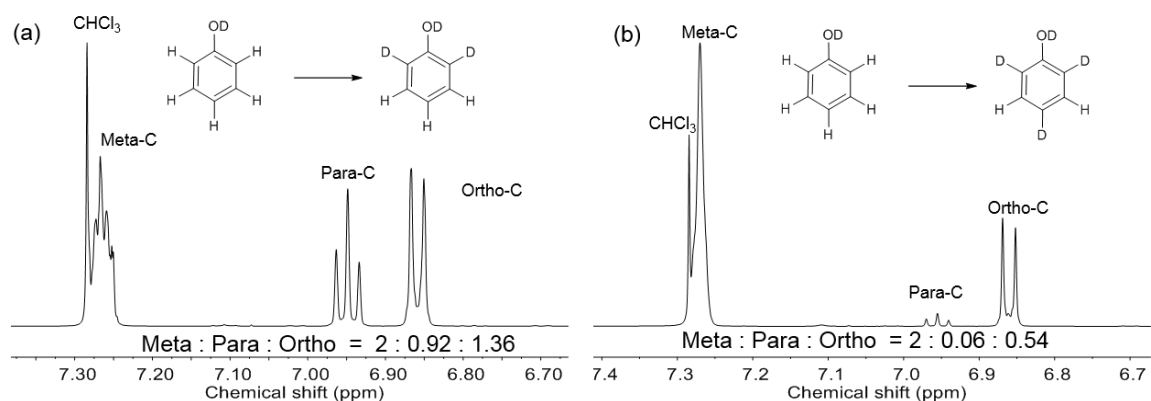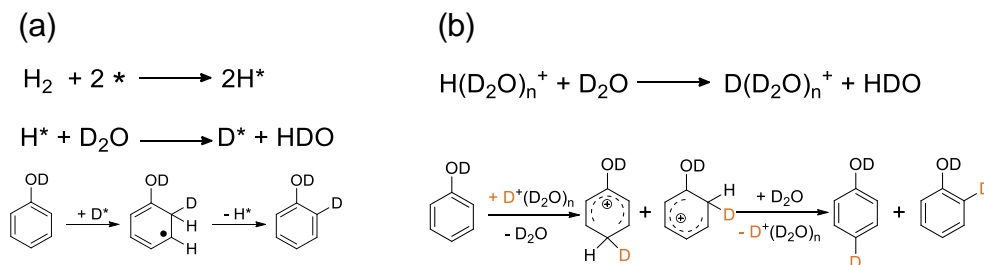

Figure 4.5. ^{1}H NMR spectra of D-substituted phenol after reaction over Pt/Silicalite-1(a) and Pt/HMFI-24 (b). Reaction conditions: 0.3 g phenol, 0.005 g Pt-based catalyst, 30ml of D_2O, 40bar H_2, at 473 K for 0.5 h, stirring speed of 700 rpm.

Scheme 4.3. H/D substitution pathways of phenol on Pt in the absence (a) and in the presence (b) of hydronium ion.

4.3.3. Phenol hydrogenation pathways over Pt/HMFI-24 catalyst.

The hydrogenation pathways of phenol in the presence or absence of hydronium ion are proposed in **Scheme 4.4**. In terms of phenol hydrogenation in the absence of hydronium ion, i.e. over Pt/Silicalite-1 (**Scheme 4.4a**), the first H was added at the ortho-position of the aromatic ring to form HPh*, which was the rate-determining step. The second H-addition step occurred to generated H_2Ph^*. The energy diagram of this process is depicted in **Figure 4.6**. The starting state of phenol hydrogenation involved adsorbed phenol and gas-phase H_2, because the reaction orders on phenol and H_2 were 0 and 0.5. The dissociative chemisorption of H_2 into two adsorbed H atoms occurred on Pt surface and gave an adsorption heat of $\sim$50 kJ·mol^{-1} (**Chapter 3**). Afterward, the first H-addition as rate-determining step took place by adding adsorbed H atom into adsorbed phenol to generate HPh*. The measured apparent activation enthalpy (94 kJ·mol^{-1}) reflected the difference in the energy level between transition state of first H-addition and adsorbed state of phenol and one H atom. Therefore, the intrinsic activation enthalpy of phenol hydrogenation over Pt/Silicalite-1 should combine the adsorption heat of H atom (25 kJ·mol^{-1}) and apparent activation enthalpy of 94 kJ·mol^{-1}, hence giving 119 kJ·mol^{-1}.
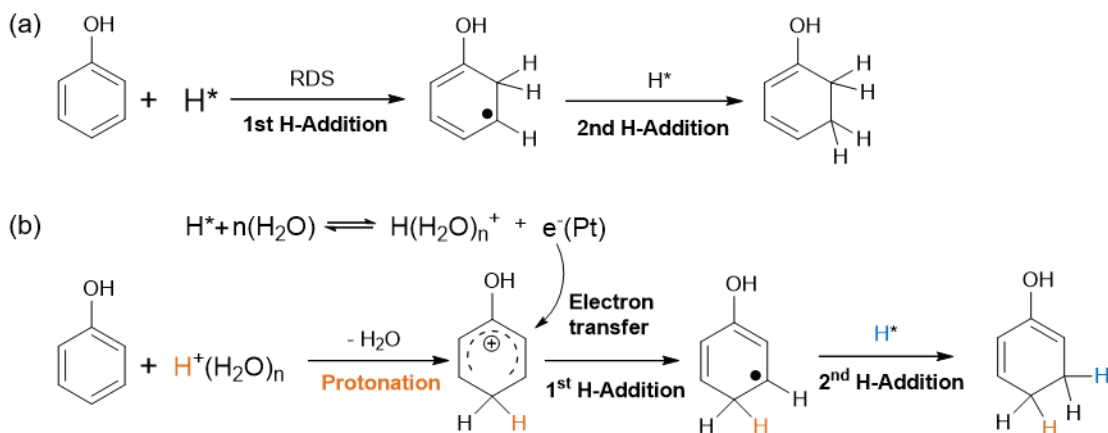
Scheme 4.4. Phenol hydrogenation pathways on Pt site in the absence (a) or in the presence (b) of hydronium ions.
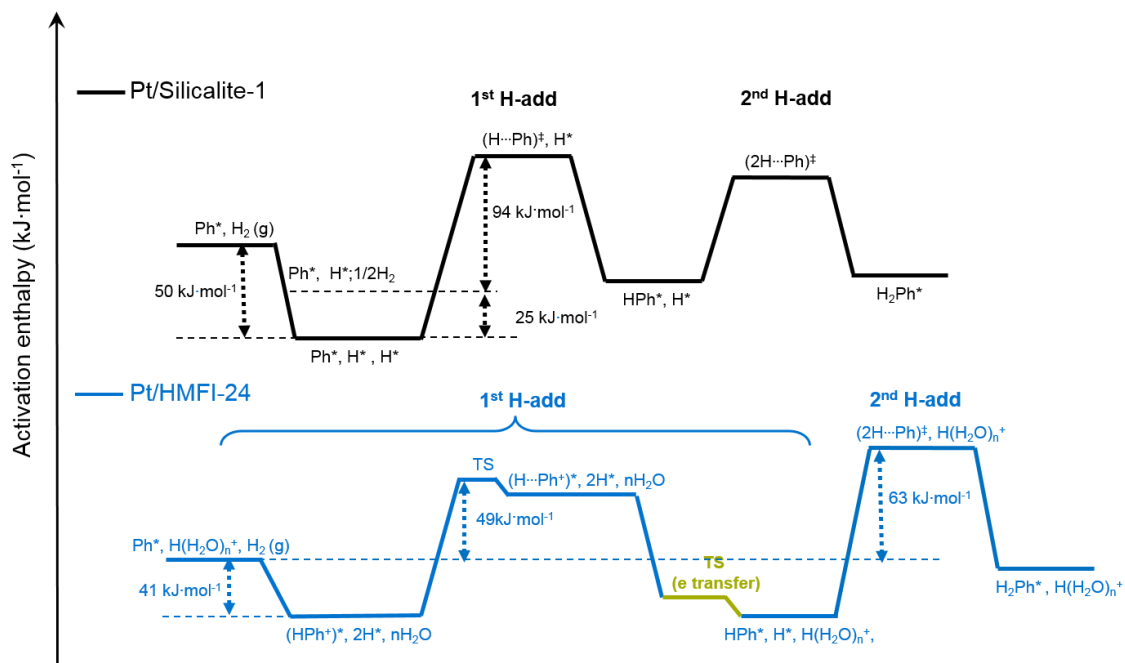
Figure 4.6. Energy diagrams of phenol hydrogenation in the aqueous phase on Pt/Silicalite-1 (black), and on Pt/HMFI-24 (blue).

The hydrogenation of phenol in the presence of hydronium ions underwent a complex H addition route, in which protonation of phenol aromatic ring and electron transfer from adsorbed H to protonated phenol were involved (**Scheme 4.4b**). Firstly, the phenol molecule saturatedly adsorbed on the Pt surface. Then the aromatic ring of the adsorbed phenol got protonated by the hydronium ions from the zeolite support, followed by accepting an electron via Pt surface from adsorbed H to generated 1st H-added phenol (HPh*). While the adsorbed H-atom transformed into a hydronium ion upon interaction with water after donating the electron to the aromatic ring of protonated phenol. The processes of protonation and electron transfer decreased the activation enthalpy of first H-addition step to a level lower than the second H-addition step. It was proved by the determination of activation enthalpy of phenol ring protonation which gave 49 kJ·mol^{-1} (**Figure A4.7** in **Appendix**), lower than apparent activation enthalpy of phenol hydrogenation (63 kJ·mol^{-1}). The schematic energy diagram of this process was shown in **Scheme 4.4b**. The adsorption heat of H_2 over Pt/HMFI-24 was estimated to be 41 kJ·mol^{-1} in the Chapter 3. Given the 1st reaction order of H_2, the intrinsic activation enthalpy of phenol hydrogenation over Pt/HMFI-24 was the sum of H_2 adsorption heat (41 kJ·mol^{-1})

and the measured apparent activation enthalpy (63 kJ·mol^{-1}), giving 104 kJ·mol^{-1}, which was lower than that on Pt/Silicalit-1. Therefore, hydrogenation rate of phenol increased with the growing concentration of hydronium ions from the MFI support.

4.4. Conclusions

Pt clusters encapsulated in MFI with varying Brønsted acid site concentrations were tested in phenol hydrogenation in the aqueous phase. Catalysts with higher hydronium ion concentrations in MFI micropores showed weaker adsorption of phenol, but higher hydrogenation activity. Different hydrogen addition pathways over acidic or non-acidic Pt/MFI catalysts were proposed, based on the different reaction orders of H$_2$. In the absence of hydronium ions, molecular adsorption of phenol and dissociative adsorption of H$_2$ firstly occurred on the Pt surface, then the phenol hydrogenation proceeded through the first addition of active H atom to the adsorbed phenol, the step of which was the rate-determining step and gave an intrinsic activation enthalpy of 119 kJ·mol^{-1}. In the presence of hydronium ions from MFI support, as depicted in **Figure 4.7**, the adsorbed phenol molecule firstly got protonated by the hydronium ion, instead of conventional addition of H atom. Afterward, the protonated phenol accepted one electron from the adsorbed H via the Pt surface to form first H-added phenol. In this step, the adsorbed H atom transformed into hydronium ions by interaction with water after providing one electron. Then the second H-addition step by the adsorbed H atom took place. The process of phenol protonation coupled with electron transfer decreased the energy barrier to a level that even lower than 2nd H-addition step. Therefore, the rate-determining step was 2nd H-addition step, giving a lower intrinsic activation enthalpy of 104 kJ·mol^{-1} than 119 kJ·mol^{-1} in the absence of hydronium ions. Consequentially, the protonation of phenol aromatic ring coupled with electron transfer in the presence of hydronium ions, led to a higher rate than the conventional addition of hydrogen atom.
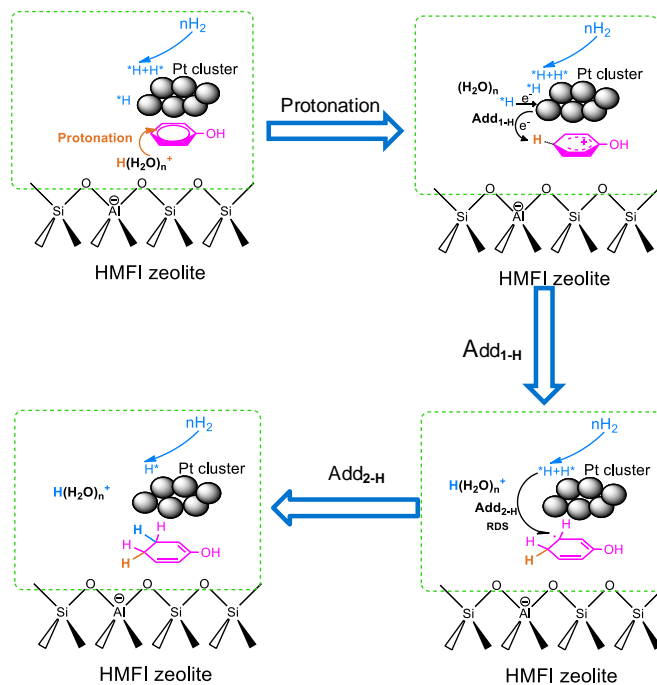
Figure 4.7. Proposed hydrogenation pathway of phenol in the presence of hydronium ions.

4.5. Appendix

Calculations

Conversion, reaction rate, turnover frequency (TOF) and carbon balance were calculated according to the following equations:

Conversion = (weight of converted reactant/weight of the starting reactant) × 100%.

TOF = mole of converted reactant / (mole of active metal site × reaction time).

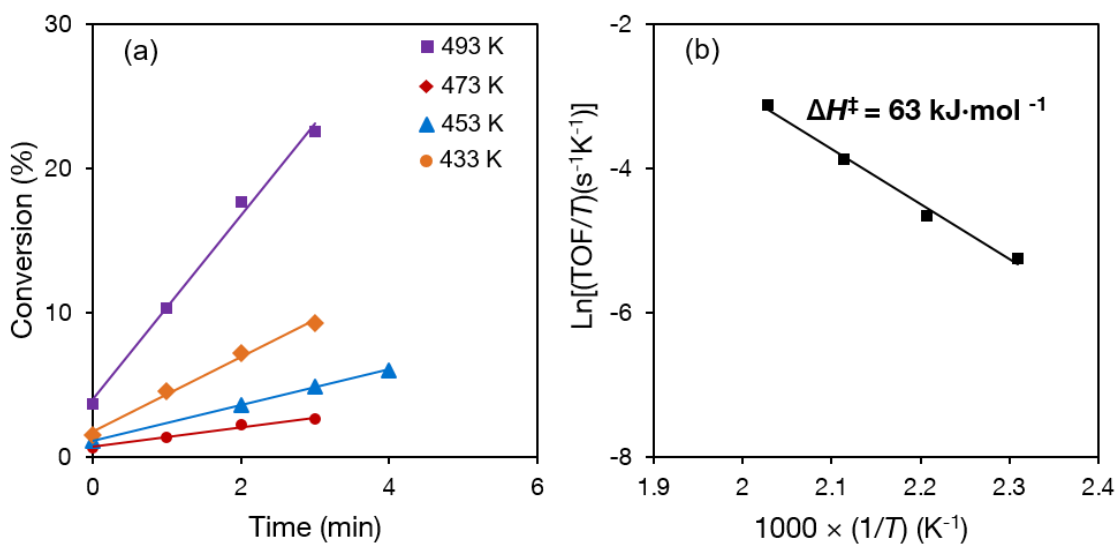The carbon balance = mole of carbon in starting reactant/mole of carbon in the product.

Figure A4.1. Phenol hydrogenation reaction over Pt/HMFI-24 at 433 − 493 K under 40 mbar H_2. (a) Conversion of phenol as a function of reaction time at 433 − 493 K; (b) Eyring plot to determine the activation enthalpy and entropy.

Figure A4.2. Phenol hydrogenation reaction over Pt/HMFI-40 at $433 - 493$ K under 40 mbar H_2. (a) Conversion of phenol as a function of reaction time at $433 - 493$ K; (b) Eyring plot to determine the activation enthalpy and entropy.
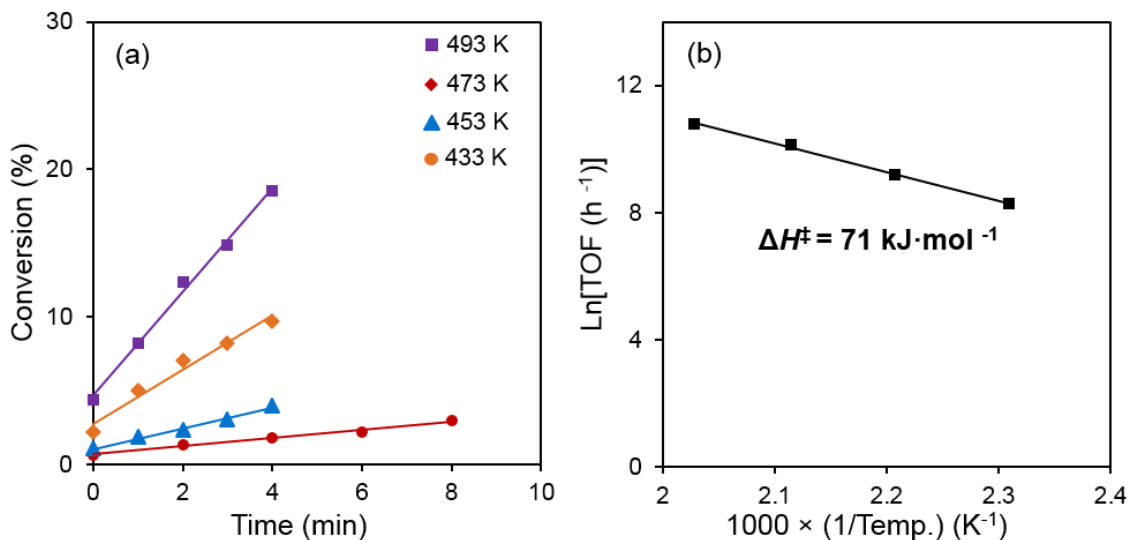

Figure A4.3. Phenol hydrogenation reaction over Pt/HMFI-120 at $433 - 493$ K under 40 mbar H_2. (a) Conversion of phenol as a function of reaction time at $433 - 493$ K; (b) Eyring plot to determine the activation enthalpy and entropy.

Figure A4.4. Phenol hydrogenation reaction over Pt/HMFI-430 at 433 – 493 K under 40 mbar H$_2$. (a) Conversion of phenol as a function of reaction time at 433 – 493 K; (b) Eyring plot to determine the activation enthalpy and entropy.
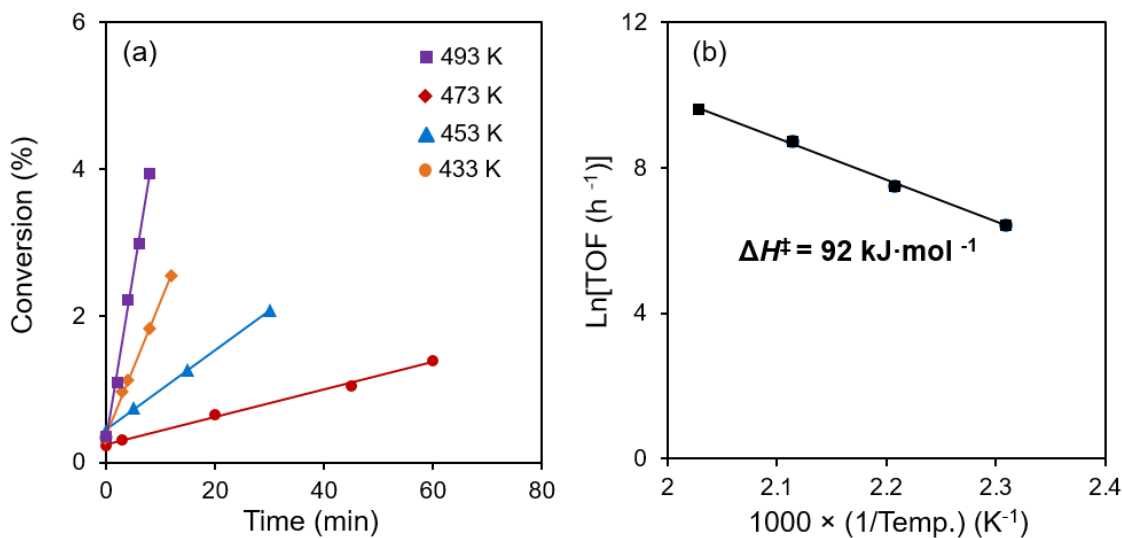

Figure A4.5. Phenol hydrogenation reaction over Pt/Silicalite-1 at 433 – 493 K under 40 mbar H$_2$. (a) Conversion of phenol as a function of reaction time at 433 – 493 K; (b) Eyring plot to determine the activation enthalpy and entropy.
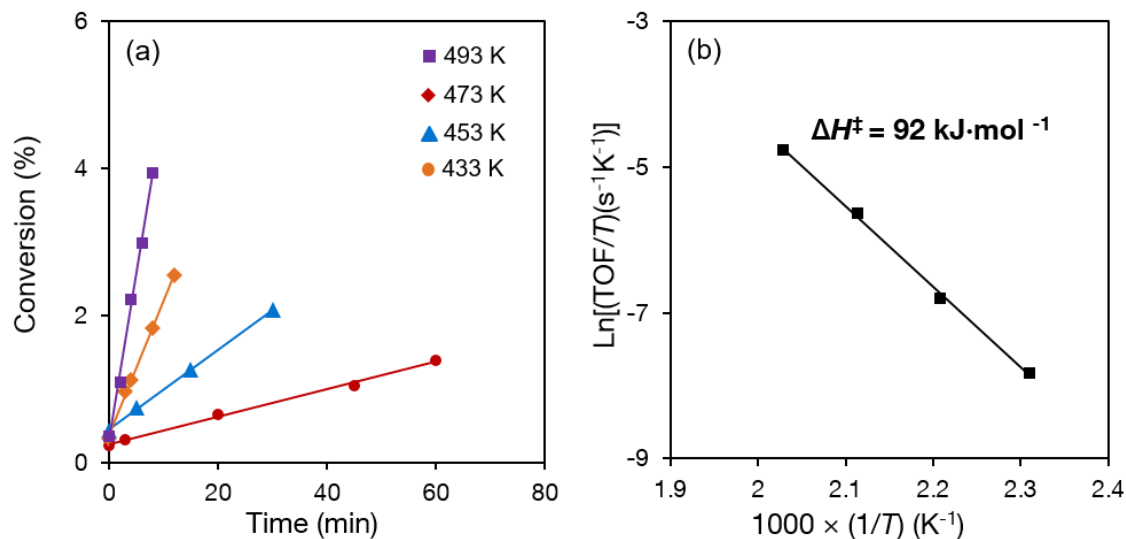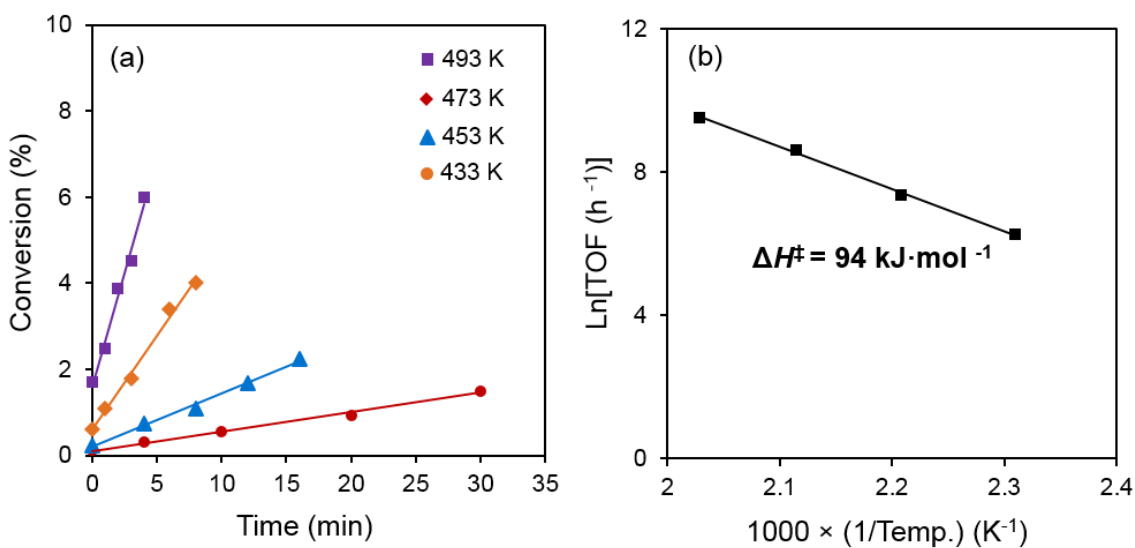
Table A4.1. TOFs, activation enthalpies and entropies of phenol hydrogenation over the Pt/MFI samples with different BAS concentrations.

Catalyst	BAS	TOF (h^{-1})				$\Delta H^{\ddagger}$	$\Delta S^{\ddagger}$
	μmol.g^{-1}	433 K	453 K	473 K	493 K	kJ·mol^{-1}	J·mol^{-1}·K^{-1}
Pt/HMFI-24	658	2.3	4.3	9.8	21.7	63	-94
Pt/HMFI-40	414	1.1	2.7	6.9	13.2	71	-83
Pt/HMFI-120	112	0.3	1.1	3.1	6.8	89	-52
Pt/HMFI-430	48	0.2	0.5	1.7	4.2	92	-51
Pt/Silicalite-1	0	0.1	0.4	1.5	3.8	94	-47
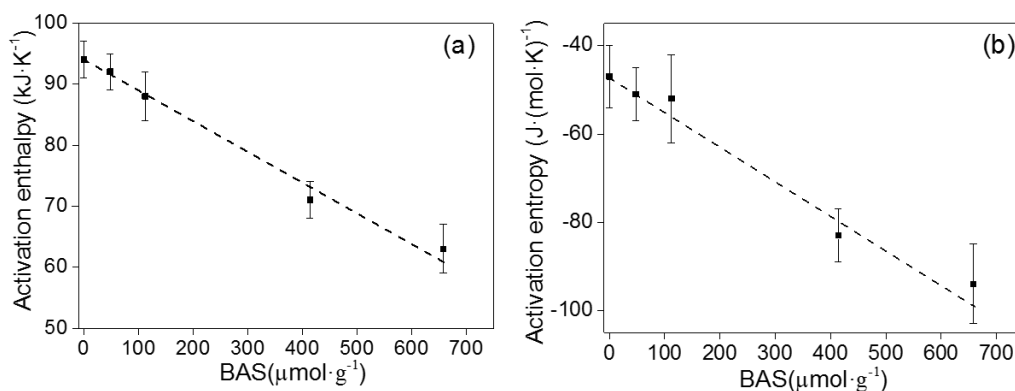
Figure A4.6. Activation enthalpies (a) and entropies (b) of phenol hydrogenation as a function of support BAS concentrations.
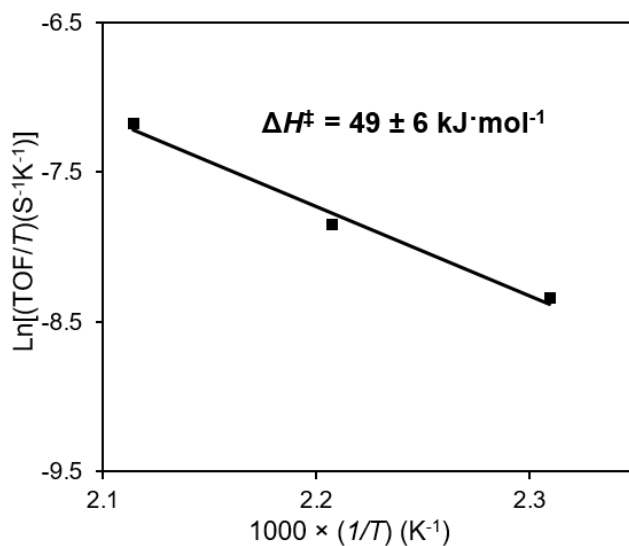

Figure A4.7. Eyring plot to determine the activation enthalpy ($\Delta H^{\ddagger}$) of H/D substitution reaction of phenol on Pt/HMFI-24 in the presence of H$_2$. Reaction conditions: 0.3 g phenol, 0.05 g Pt/HMFI-24, 30ml D$_2$O; at 433; 453 and 473 K, under 40 bar H$_2$ (ambient temperature), stirring at 700 rpm.

4.6. Associated content

Publication

This chapter in combination with Chapter 2 is to be submitted for publishment. The content and structure of Chapter 4 are different from the manuscript.

Contributions

In this work, Dr. Yue Liu supervised the topic of Influence of support acidity on the Pt-catalyzed hydrogenation of phenol in the aqueous phase. Guoju Yang contributed to the design of the experiments and operation of setups, and data analysis. Mr. Sebastian Eckstein contributed with the determination of adsorption isotherms of phenol in the aqueous phase. Prof. Dr. Johannes A. Lercher was responsible for data discussion, supervising and manuscript preparation. Dr. Yue Liu and Prof. Dr. Johannes A. Lercher are the principal investigators of this work.

Acknowledgments

The author would like to thank Xaver Hecht and Martin Neukamm for technical support. Financial support in China Scholarship Council is highly appreciated. The author is grateful to the fruitful discussions with Dr. Donald M. Camaioni and Dr. Hui Shi at Pacific Northwest National Laboratory.

4.7.   References

[1] Z. Karpinski, S.N. Gandhi, W.M.H. Sachtler, *J. Catal.,* 141 (**1993**) 337-346.

[2] B.L. Mojet, J.T. Miller, D.E. Ramaker, *et al.*, *J. Catal.,* 186 (**1999**) 373-386.

[3] A.Y. Stakheev, L.M. Kustov, *Appl Catal a-Gen,* 188 (**1999**) 3-35.

[4] G. Larsen, G.L. Haller, *Catal. Lett.,* 3 (**1989**) 103-110.

[5] F. Hoxha, B. Schimmoeller, Z. Cakl, *et al.*, *J. Catal.,* 271 (**2010**) 115-124.

[6] P. Salagre, J.L.G. Fierro, F. Medina, *et al.*, *J. Mol. Catal. A: Chem.,* 106 (**1996**) 125-134.

[7] V.L. Barrio, P.L. Arias, J.F. Cambra, *et al.*, *Applied Catalysis A: General,* 248 (**2003**) 211-225.

[8] J. Lif, I. Odenbrand, M. Skoglundh, *Applied Catalysis A: General,* 317 (**2007**) 62-69.

[9] R. Wang, Y. Li, R. Shi, *et al.*, *J. Mol. Catal. A: Chem.,* 344 (**2011**) 122-127.

[10] W.J. Song, Y.S. Liu, E. Barath, *et al.*, *Green Chemistry,* 17 (**2015**) 1204-1218.

[11] C. Zhao, S. Kasakov, J.Y. He, *et al.*, *J. Catal.,* 296 (**2012**) 12-23.

[12] K. Christmann, *Surf. Sci. Rep.,* 9 (**1988**) 1-163.

[13] G.F. Li, J.Y. Han, H. Wang, *et al.*, *ACS Catal,* 5 (**2015**) 2009-2016.

[14] G. Bouchoux, D. Defaye, T. McMahon, *et al.*, *Chem-Eur J,* 8 (**2002**) 2900-2909.

Chapter 5

Summary and conclusions

The aim of this thesis is to synthesize small and uniform Pt nanoparticles encapsulated in the micropores of MFI-type zeolite as bifunctional catalysts for the hydrogenation of phenol. A novel kinetic method was developed for obtaining the detailed kinetics and thermodynamics of H_2 adsorption on transition metal catalysts. The impact of support acidity on Pt-catalyzed phenol hydrogenation was investigated, as it represented an efficient H-addition pathway for improving hydrogenation reactions. The focuses are (1) relating the superior performances of the sub-nanosized Pt clusters encapsulated in HMFI support to the intrinsic properties of acid-promoted metal nanoparticles, (2) understanding the individual and cooperative roles of metal and acid sites in the bifunctional catalyst, (3) clarifying individual reaction steps in the integrated reaction network occurred during phenol hydrogenation.

A series of Pt/MFI catalysts composed of the sub-nanosized Pt cluster encapsulated in MFI zeolite were prepared and characterized. All the physical and chemical properties of these samples were comparable, except different BAS concentrations of the MFI supports. STEM images showed that Pt clusters (≤ 2 nm) were well-distributed and encapsulated in the micropores of MFI zeolites for all the catalysts. Both of XANES and the IR spectra of CO adsorption revealed an electron-deficient state of Pt clusters in adjacent to BAS. The H/D exchange reaction between H_2 and D-form zeolite was performed to figure out the interaction between the Pt and BAS, which suggested the dissociative adsorption of H_2 on Pt surface and the interaction of Pt clusters with proximal BAS in the micropores of MFI zeolite.

Furthermore, a kinetic method was developed for determining the adsorption kinetics and thermodynamics of H_2 on Pt/MFI catalysts in the aqueous phase. Using the reaction of gas H_2 with liquid D_2O into liquid HDO, gas HD and D_2 catalyzed by Pt, a correlation among the reaction rate, H_2 pressure and H_2 adsorption constant was established. By measuring the HD and D_2 formation rates as well as their variations with pressure and temperature, the H_2 adsorption constant and adsorption heat were determined.

The impact of zeolite support acidity on the Pt-catalyzed hydrogenation of phenol was investigated in details. The hydrogenation rate of phenol exhibited a positive trend with the

increasing of support acidity. The hydronium ions from MFI support promoted the H-addition rate of phenol under reaction conditions. Catalysts with higher hydronium ion concentrations in MFI micropores showed weaker adsorption phenol, but higher hydrogenation activity. In the presence of hydronium ions, protonation of the aromatic ring coupled with electron transfer led to a higher rate than the conventional addition of hydrogen atom.

In conclusion, the comprehensive knowledge of various preparation methods and in-depth understanding of individual reaction kinetics allow us to design bifunctional catalysts with carefully adjusted active metal and acid sites which can improve catalytic reactions. This would open new possibilities to design efficient and stable catalysts for highly selective conversion of biomass feedstocks into green (free of sulfur, oxygen, and polyaromatics), sustainable, and high-grade transportation fuels.

Chapter 6

Zusammenfassung und Folgerungen

Das Ziel dieser Thesis ist, kleine und gleichgroße Pt Nanopartikel, welche sich in Mikroporen von MFI artigen Zeoliten befinden, als bifunktionale Katalysatoren für die Phenolhydrierung zu synthetisieren. Eine neuartige kinetische Methode wurde entwickelt, um die detaillierte Kinetik und Thermodynamik der H_2 Adsorption auf Übergangsmetallkatalysatoren zu erhalten. Der Einfluss des aziden Trägers auf Pt katalysierter Phenolhydrierung wurde untersucht, da sie einen effizienten H-Additionsmechanismus für die Verbesserung der Hydrierungsreaktionen zeigt. Die Schwerpunkte liegen auf (1) der Beziehung zwischen den überragenden Leistungen der sub-nanoskalierten Pt Clustern, welche sich in HMFI Mikroporen befinden, und der intrinsischen Eigenschaften der säurefördenden Metallnanopartikeln, (2) dem Verständnis der individuellen und kooperativen Rolle des Metalls und den aziden Stellen im bifunktionalen Katalysator, (3) der Erläuterung der einzelnen Reaktionsschritte im integrierten Reaktionsnetzwerk während der Phenolhydrierung.

Es wurden eine Reihe von Pt/MFI Katalysatoren, die aus den sub-nanoskalierten Pt Clustern bestehen und sich in MFI Zeolithen befinden, präpariert. Die physikalischen und chemischen Eigenschaften dieser Proben sind mit Ausnahme der unterschiedlichen BAS Konzentrationen des MFI Trägers vergleichbar. STEM Analysen zeigten, dass Pt Cluster ($\leq$ 2nm) gut verteilt sind und in den Mikroporen des MFI Zeoliths für alle Katalysatoren eingekapselt sind. Sowohl XANES als auch die IR Spektren der CO Adsorption ergaben einen Elektronenmangelzustand der Pt Cluster in Angrenzung zu BAS. Die H/D Austauschreaktion zwischen der H_2 und der D-Art des Zeoliths wurde durchgeführt, um die Interaktion zwischen dem Pt und BAS, welche die dissoziative Adsorption von H_2 auf der Pt Oberfläche beweist und die Existenz von Interaktionen des Pt Clusters mit Proximal BAS in den Mikroporen des Zeoliths zeigt, herauszufinden.

Zusätzlich wurde eine kinetische Methode entwickelt, die die Adsorptionskinetik und Adsorptionsthermodynamik von H_2 auf Übergangsmetallen in Wasser bestimmt. Ein Zusammenhang zwischen der Reaktionsrate, des H_2 Drucks und der H_2 Adsorptionskonstante wurde, unter Verwendung der durch Übergangsmetall-katalysierten Reaktion von gasförmigen H_2 mit flüssigem D_2O in flüssigen HDO, gasförmigen HD und D_2 , hergestellt. Die H_2 Adsorptionskonstante und Adsorptionswärme wurde sowohl durch

Messung der HD und D_2 Bildungsraten als auch durch Variation des Drucks und der Temperatur bestimmt.

Der Einfluss von aziden Zeolithträgern auf die Kinetik der Pt katalysierte Hydrierung von Phenol wird im Detail untersucht. Mit Erhöhung der Trägerazidität zeigen die Hydrierungsraten von Phenol einen positiven Trend. Unter Reaktionsbedingungen fördern die Hydroniumionen des MFI Trägers die H-Additionsrate von Phenol. Katalysatoren mit hoher Hydroniumionen Konzentrantion in MFI Mikroporen zeigten eine schwächere Adsorption von Phenol, aber eine höhere Hydrierungsaktivität. In Gegenwart von Hydroniumionen führte die Protonierung des aromatischen Rings, gepaart mit Elektronentransfer, zu einer höheren Rate als die herkömmliche Addition des Wasserstoffatoms.

Abschließend kann gesagt werden, dass das umfassende Wissen über verschiedene Vorbereitungsmethoden und das tiefgehende Verständnis der individuellen Reaktionskinetik es uns ermöglichen, bifunktionelle Katalysatoren mit sorgfältig eingestellten aktiven Metall- und Säurestellen zu entwickeln, die die katalytischen Reaktionen verbessern können. Dies würde neue Möglichkeiten eröffnen, um effiziente und stabile Katalysatoren für eine hoch selektive Umwandlung von Biomasse-Rohstoffen in „grüne" (frei von Schwefel, Sauerstoff und Polyaromaten), nachhaltige und hochwertige Transportbrennstoffe zu entwerfen.

Curriculum vitae

Guoju was born in September 13th 1987 in Heilong Jiang, China In 2006, he entered department of chemistry in Jilin University, located in Changchun, Jilin Province in China, and majored chemistry. Till July 2010, he obtained his Bachelor title in Chemistry. In the same year, he was admitted into State Key Laboratory of Inorganic Synthesis and Preparative for his master study, majoring inorganic chemistry. The research focused on preparation and application of nanosized SAPO-34 zeolite. He leadered and cooperated in several projects including the methanol to olefin conversion over sheet-like and sphere-like nanosized SAPO-34 zeolites. During 2010 – 2012, he studied at Dalian Institute of Chemical Physics, Chinese Academy of Sciences, as a visiting postgraduate student, majoring chemical engineering. During his master study, he published 1 journal and obtained several rewards including 3-year full covered scholarships. He obtained his master degree in inorganic chemistry in 2016 in Jilin University. The same year, he was granted the doctor position by Prof. Dr. Johannes A. Lercher from Technical Chemistry II, Technische Universität München and the scholarship from Chinese Scholarship Council. Since then, he did his Ph.D. study under Prof. Lercher's guidance on "biomass conversion over Pt/MFI bifunctional catalysts." His research focused on developing sub-nanosized Pt clusters encapsulated in the micropores of MFI zeolite and investigating the influence of support acidity on hydrogenation reactions, from the view of designing efficient catalysts and studying reaction kinetics.

.

List of publications

Journals

Guoju Yang, Xi Chen, Yue Liu[*], Johannes A. Lercher[*] "Determination of H_2 adsorption heat on transition metals in water", to be submitted.

Guoju Yang, Sebastian Eckstein, Hui Shi, Donald M. Camaioni, Eszter Baráth[*], Yue Liu[*], and J. A. Lercher[*] "Influence of acid sites on the Pt-catalyzed hydrogenation of phenol in the aqueous phase", to be submitted.

Guoju Yang, Thomas J. Bauer, Gary L. Haller, Johannes A. Lercher and Eszter Baráth[*] "H-Transfer reactions of alkenes with tertiary alkyl amines in the presence of carbon supported noble metals", to be submitted.

Poster presentation

Influence of acid sites on the Pt-catalyzed hydrogenation of phenol in the aqueous phase.

Guoju Yang, Yue Liu, Eszter Baráth, Johannes A. Lercher in the 16th International Congress on Catalysis